Generative Thermal Design Through Boundary Representation and Deep Reinforcement Learning

by

Hadi Keramati

A thesis
presented to the University of Waterloo
in fulfillment of the
thesis requirement for the degree of
Doctor of Philosophy
in
Mechanical and Mechatronics Engineering

Waterloo, Ontario, Canada, 2022

Examining Committee Membership

The following served on the Examining Committee for this thesis. The decision of the Examining Committee is by majority vote.

External Examinor:	Sajjad Bigham Assistant Professor Dept. of Mechanical Engineering-Engineering Mechanics Michigan Technological University
Supervisor:	Feridun Hamdullahpur Professor Dept. of Mechanical and Mechatronics Engineering University of Waterloo
Internal-External Member:	Nima Maftoon Assistant Professor Dept. of Systems Design Engineering University of Waterloo
Internal Member:	Xianguo Li Professor Dept. of Mechanical and Mechatronics Engineering University of Waterloo
Internal Member:	Arash Arami Assistant Professor Dept. of Mechanical and Mechatronics Engineering University of Waterloo

Author's Declaration

This thesis consists of material all of which I authored or co-authored: see Statement of Contributions included in the thesis. This is a true copy of the thesis, including any required final revisions, as accepted by my examiners. I understand that my thesis may be made electronically available to the public.

Statement of Contributions

The content of this thesis are based on the manuscripts that are published in several journal and conference papers. As a results, a number of co-authors have contributed to some parts the current work. Individual contributions are as follows:

Prof. Feridun Hamdullahpur: Supervision, mentoring, funding acquisition, review and editing all the research work

Prof. Michael Ohadi: Supervision and review in early stage of the work for chapter 2 and chapter 3

Mojtaba Barzegari: Helped in primary software installation for chapter 4

Dr. Fabio Battaglia: Addressed comments from reviewers for chapter 3

Dr. Xiang Zhang: Main researcher in some of the parts provided in chapter 2

Abstract

Advancement in Additive Manufacturing (AM) allows fabrication of complex geometries. This provides the opportunity to think beyond hand-designed topologies. The main goal of this dissertation is to build a Generative Design (GD) framework which generates several optimal topologies. In this framework, Machine Learning (ML) accelerated predictive models in conjunction with a precise geometry representation for thermal design automation are used to reach an effective design space exploration.

A size optimization algorithm is presented to optimize the geometry of Manifold-microchannel heat exchanger with straight fins using genetic algorithm and a hybrid Computational Fluid Dynamics (CFD) model. Challenges for process development pertinent to this design configuration using AM are also introduced particularly in microchannel part which can be addressed by efficient design methods.

Reinforcement Learning is a branch of machine learning with strong capabilities in sequential decision making to maximize a reward. This decision making tool along with a parametric approach for geometry representation are utilized for fin shape optimization in heat exchanger design.

Machine learning models and neural networks provide predictive tools for a wide range of applications. In this thesis, Convolutional Neural Networks (CNNs) are deployed to successfully predict heat transfer and pressure drop of the geometries that can efficiently explore the design space. A high level accuracy is seen in predicting direct CFD results from shapes saved as images.

Online computing for optimization is complex and computationally expensive. The pre-trained CNN models are used as an alternative for computational engine in GD. This method drastically reduces the time required for one episode of reinforcement learning from several minutes to few seconds.

The design space is expanded to multiple fin shape optimization using Multi-Agent Proximal Policy Optimization (MAPPO) in which each shape is controlled in a decentralized way while value learning is performed in a centralized way. We validate our method using Multi-agent Particle-world Environment (MPE) for high dimensional action space. It is shown that cooperative interaction of agents with a shared reward results in optimal thermal design solutions with reduced pressure drop and enhanced heat transfer.

A robust generative thermal design framework is developed with which there is no need for discretized design domain or derivation with respect to the domain settings. Proposed method provides the tools and knowledge for efficient use of time, physical space and computational resources particularly for microchannel heat exchanger design.

Acknowledgements

I would like to express my sincere gratitude to my supervisor, Prof. Feridun Hamdullahpur, for granting me the opportunity to work on this fascinating project and for his support and guidance.

I would like to thank Prof. Michael Ohadi for building the backbone of my research at the early stage of my PhD journey and his continuous support and guidance.

I would also like to thank the members of the examining committee, Prof. Xianguo Li, Prof. Nima Maftoon, Prof. Arash Arami, and Prof. Sajjad Bigham for their helpful insights and valuable time.

I also express my gratitude to Khosrow Modarresi, the technology transfer manager at Waterloo commercialization office, for his valuable collaboration and communication to secure intellectual property through patent application, and to walk us through funding acquisition for commercialization of the developed framework.

I would like to thank Dr. Nigel Morris at Autodesk Inc for providing opportunities for my industry talks and Dr. Adrian Bejan for his constructive feedback and novel ideas.

Dedication

To my family.

Table of Contents

List of Figures

List of Tables

Chapter 1

Introduction

Heat eXchangers (HXs) have wide applications such as car radiators, computer cooling, Heating, Ventilation, and Air Conditioning (HVAC), recuperators for gas turbine engines, aerospace, waste heat recovery, and fuel cell systems [1–3]. With the demand for more effective use of energy, increased awareness about environmental issues and high cost of energy carriers, effective heat exchanger design solutions have gained more attention.

Additive Manufacturing (AM) allows conversion of complex digital geometries to functional real world objects beyond the capabilities of conventional manufacturing methods [4, 5]. Existing methods in engineering design, however, are not effective to fully utilize the potential opportunities provided by AM. In many engineering practices, limited number of pre-defined design candidates are analyzed showing a gap between design solutions and the flexibility and effectiveness provided by AM.

Generative Design (GD) is a design exploration process performed iteratively over various geometries followed by a performance evaluation [6]. There are several GD techniques introduced recently including the ones that rely on traditional Topology Optimization (TO), Generative Adversarial Networks (GANs), Variational Autoencoders (VAEs), and deep Reinforcement Learning (RL) [7, 8].

In many engineering problems such as thermal design, sufficient data are not available to be used for methods that require an existing dataset (e.g. GANs and VAEs). Therefore, most of the GD problems in engineering rely on TO. Several TO methods are used in mechanical and structural design among which density-based method known as SIMP (Solid Isotropic Material with Penalization) and level set method are widely used for different material minimization application.

TO and design automation generally require solving Partial Differential Equations (PDEs). High fidelity simulation which is commonly used to solve PDEs is CPU-intensive, particularly in presence of complex physics [9]. Since high fidelity simulation is not important during the concept design process, a high performance estimator can accelerate the design process to a great extent [8, 10]. Deep Learning (DL) and neural networks provide predictive models for a wide range of applications. Physics-Informed Neural Network (PINN) and feedforward neural networks, for example, showed promising results as surrogate models to predict results of computer simulation [11, 12]. DL can be used to estimate the results of simulation from different geometries which provides accelerated iterative process in GD.

Traditional TO methods are not practical for thermo-fluid applications since porous medium approaches are used for solid distribution. In fluid flow and particularly heat exchanger design, boundary conditions are significant parts of the simulation and it is important to have distinguishable and precise boundaries [13–15]. Moreover, for several applications such as those in biomedical engineering, working fluids (e.g. nanofluids) and particular boundary conditions require clear boundaries for implementation [16–21]. A convenient way of optimizing the design while keeping the boundaries distinguishable is to use pixel or voxel-based optimization which requires high CPU time due to the curse of dimensionality [22]. In thermofluid design, the direction to greater performance is aligned with greater design freedom [23, 24]. Providing freedom in design is, however, computationally demanding and impose manufacturing challenges.

Reinforcement Learning (RL) is one of the basic components of Machine Learning (ML). Many types of algorithms are introduced for classification, regression, clustering, etc. RL, however, is a real time sequential decision making algorithm that can be applied to numerous real-world applications. This powerful decision making tool has potential applications in decision making for engineering design and heat transfer if proper setting is provided.

There are several design representation including Signed Distance Functions (SDFs), pixels and voxels, point clouds, graphs, mesh, grammars, and Boundary Representation (BREP). Most of other geometry representations should be converted to BREP as the native Computer-Aided Design (CAD) representation for fabrication. Working directly on BREP is an advantage in simulation and manufacturing. BREP also facilitates boundary condition implementation which is crucial for thermo-fluid structures where nonlinear PDEs should be solved numerically. BREP also gained attention among researchers in structural topology optimization [25, 26].

1.1 Research Objectives

Given the current state of generative design methods for thermal devices, and motivated by the above rationale, the goal of the current dissertation is to develop a framework to facilitate the design generation for heat transfer devices with fins.

As articulated above, there is a gap between what can be designed and what can be manufactured. In this dissertation, an attempt is made to reduce the time and enhance the performance of the design automation to close the aforementioned gap.

The speed of performance evaluation in engineering design is crucial for the search algorithms. Accelerated physics prediction is achieved utilizing different supervised machine learning algorithms to reduce the time required for one iteration in the design optimization.

The other objective of the current research is to use boundary representation which is a native geometry representation for downstream tasks susch as manufacturing and simulation software. Topological representation using parametric curve reduces the dimension of the optimization problem without sacrificing the resolution of the shape or freedom to change the design [27]. This representation provides exact geometrical definition regardless of the size of discretization in numerical approach [28].

1.2 Thesis Overview

This thesis is structured in a way that each chapter provides input to the subsequent one, and as such is organized as follows: Chapter 2 begins with the heat exchanger types and design considerations including operating conditions and manufacturing techniques. This chapter concludes with a review of recent study in TO and GD. Application of RL and surrogate models are also discussed. Chapter 3 presents size optimization of a pre-defined design configuration and process development using AM techniques. Chapter 4 introduces a method for generative design using continuous solid-liquid interface for a single fin shape. Chapter 5 looks at the possibility of predicting the outcome of the Computational Fluid Dynamics (CFD) for heat transfer devices (e.g. heat transfer and pressure drop). A supervised machine learning approach is used for the estimation of finite element simulation. Chapter 6 extends the proposed framework for GD to the larger problem of multiple fin shape design automation which uses chapter 5 as a computational engine and chapter 4 as a search engine. In chapter 7, a general conclusion of the current work and recommendations for future work are presented.

Chapter 2

Recent Development in Heat Exchanger Design

2.1 Introduction

This chapter provides a review of heat exchangers in terms of general design, manufacturing techniques, and operating parameters for selected applications. This chapter provides insights into challenges being encountered in the development of HXs, including material selection, recent developments in conventional and generative design, and application areas of HXs. A review on models that predict the outcome of CFD which can accelerate the GD is also provided. Part of this chapter is based on a peer-reviewed article published in "Frontiers in Heat and Mass Transfer" entitled " Recent developments in high temperature heat exchangers: A review " [5].

Heat exchangers are subjected to unique material challenges such as creep, reduced strength at high temperatures, oxidation of material, corrosion, and thermal shock. As a result, expensive alloys that retain their strength at elevated temperatures are often the material of choice. However, these alloys typically have low thermal conductivity, and difficult manufacturability [29], and thus present their own challenges in heat exchanger design and fabrication. Low strength at higher operating pressures means that the walls must be thicker, requiring more material. Thick wall geometry makes the HXs made of expensive alloys costly in most applications. One way to offset these costs is to develop compact heat exchangers that have higher surface area to volume ratio and thus reduce the amount of material needed. As a result, in the past couple of decades, there has been increased interest in the development of compact and cost effective HXs [30]. Advanced

manufacturing techniques, mainly Additive Manufacturing (AM) of metals, have recently shown promising results in fabricating compact HXs with innovative heat transfer surface designs [31].

2.2 Material Selection

Materials are key to the economic design of HXs. Materials are selected for an HX for a particular application based on a combination of mechanical properties (e.g., strength, creep resistance, fatigue), thermal properties (e.g., thermal expansion, thermal conductivity), chemical properties (e.g., oxidation, corrosion), manufacturability (e.g., machining, joining), and overall cost. Material selection may also depend upon the heat exchanger design itself. For example, applications such as those of the aerospace sector are more sensitive to the overall weight and shape of HX than the cost of heat exchanger itself. Most materials used at lower temperatures, such as steel, copper, and aluminum, lose their thermo-mechanical properties at elevated temperatures. The maximum allowable stresses of some high temperature material are shown in Fig. 2.1 and Fig. 2.2. As shown, most of these materials lose strength at temperatures exceeding 550°C and particularly above 600°C.

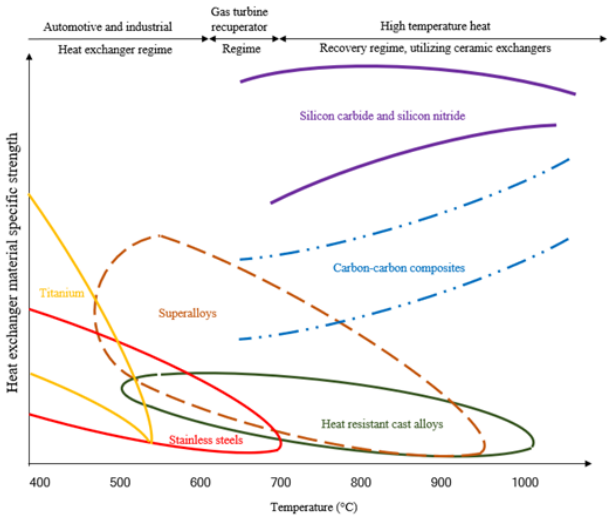

Figure 2.1: Temperature ranges for heat exchanger materials (adapted from reference [32])

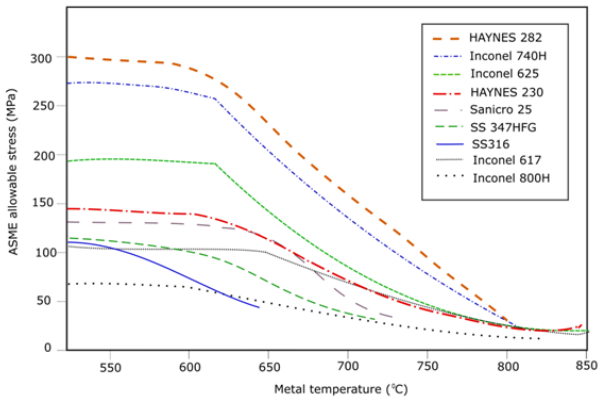

Figure 2.2: Strengths of various iron- and nickel-based alloys showing that most of the materials lose strength at higher temperatures (adapted from references [33] and [34])

2.2.1 Metals

Metals are the first choice materials for heat exchanger applications due to their excellent thermomechanical properties as well as manufacturability. When the operating temperatures rise beyond 600°C, the cost of materials increases exponentially due to steep decrease in material strength. Metallic heat exchanger materials can be divided into iron-based alloys and nickel-based superalloys. Iron-based alloys such as SS316 and SS347 have good mechanical properties up to 550°C and 600°C, respectively, but are limited in corrosion resistance at high temperatures. Nickel-based alloys with chromium are both strong and corrosion resistant at high temperatures. It should be noted, however, that the cost of Ni-based alloys is about 3 to 10 times higher than iron-based alloys [34]. Hence, iron-based alloys are preferred in applications up to 600°C in many recuperator designs, provided that corrosion and creep do not present any issues.

Iron-based Alloys

Given their mechanical properties and resistance to corrosion, iron-based alloys such as the AISI 600 series of superalloys should be considered as the first choice for moderately high temperature applications [35]. For example, type 347 austenitic stainless steel is widely used as material for recuperators that operate at temperatures up to 600°C [36, 37]. However, severe corrosion may develop for type 347 austenitic stainless steel recuperators that operate above 650°C [38]. At temperatures above 700°C, film instabilities cause oxidation,

cracking with spallation, and Cr depletion. Furthermore, cracking can accelerate oxidation by breaching the protective layer [36]. On the other hand, high temperature ferritic steels can be used for environments with fusion and fission neutron irradiation up to temperatures reaching 750°C. Ferritic steels also can be used for lead/bismuth, while silica bearing steels can be used for sulfuric acid thermal decomposition [38]. Fig. 2.3 shows the tensile strength of different steels for the range of temperatures shown. The tensile strength of austenitic, martensitic and ferritic stainless steel is higher than that of low-carbon steels. Although semi-austenitic steels show significantly high hot-strengths at low temperature, they are not suitable for temperatures higher than 650°C [39].

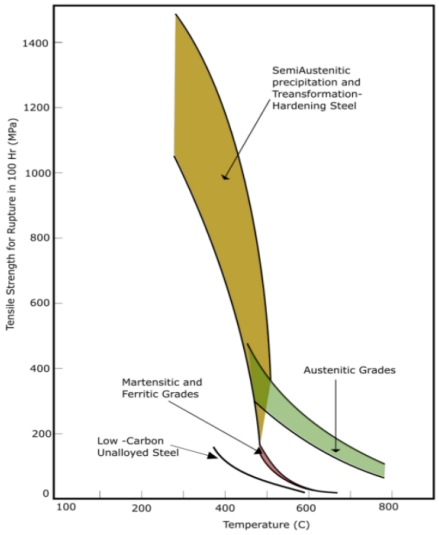

Figure 2.3: Comparison of the hot-strength of stainless steels with low carbon alloyed steels at high temperatures [40]

Nickel-based Superalloys

Nickel-based alloys exhibit better mechanical and corrosion resistance properties at higher temperatures than iron-based materials. These materials can operate at temperatures as high as 816℃. For example, selected Inconel alloys, which are a family of austenitic nickel-chromium-based superalloys, are suitable for environments subjected to high pressure, high temperature, and corrosion [41]. Heat treatment, such as annealing, of Inconel and its chromium content make it more suitable for corrosive environments than iron-based alloys [42]. In addition, while the molybdenum content of Inconel improves strength, its aluminum content improves oxidation resistance, and similarly, the nickel content improves

its corrosion resistance [43]. Other nickel-based alloys commonly used in the high temperature applications are from the Haynes family.

2.2.2 Ceramics

Although metals have advantages such as manufacturability, strength, ductility and weldability, their use in HXs is limited at very high temperatures. Ceramic materials, however, have excellent temperature resistance as well as corrosion resistance, making them the material of choice for HXs. Heat exchangers made out of ceramic materials have higher temperature capability, good corrosion and creep resistance, and low material cost, but low pressure containment capability compared to metal heat exchangers [44]. Ceramics have crystalline or partly crystalline structures and are produced from essentially inorganic, non-metallic substances. These materials are solidified from molten mass by cooling and are typically post-processed by heating. They can be divided into two types: 1) monolithic and 2) ceramic matrix composites (CMCs). Monolithic ceramic materials have a single constituent such as silicon carbide, silicon nitride, zirconia, or alumina, and are brittle and have low tension strength. Except silicon carbide and silicon nitride, other ceramics are prone to thermal shock due to large thermal gradients. This causes HXs made of these materials to suffer from lack of reliability [45]. Although ceramics have good thermo-mechanical properties, manufacturability, fabrication and mechanical joining remains a concern for their use in heat exchanger applications. Manufacturing of the primary component involves processes such as powder sintering and dry pressing. Unlike the metallic components, though, the ceramic components are limited in the type of primary shapes that can be formed economically. Further, joining of these primary components is a challenge, as mechanically joining these components is not reliable due to the brittle nature of the material. Many ceramic heat exchanger designs thus use the block structure of primary components, which are further machined and are bonded together inside an oven [46, 47]. However, in recent years, some newer bonding techniques, such as laser welding, have shown promise for joining ceramic components [48]. Given their advantage of working at high temperatures and the general push to achieve higher thermal efficiencies, further developmental efforts are expected in the near future. Monolithic ceramic materials are brittle and cannot withstand pressure. Except for silicon carbide and silicon nitride, ceramics cannot resist large thermal gradients. Monolithic ceramics thus suffer from lack of reliability [45]. To address this problem, ceramic matrix composites (CMCs) were developed to improve the thermal shock resistance, hardness, and high temperature stability [49].

2.3 Types of Conventional Heat Exchangers

As discussed previously, the cost of HX increases exponentially as the operating temperature increases, particularly above 600°C, mainly due to the material cost as well as manufacturing cost of the superalloy and ceramic heat exchangers. Higher pressure applications such as those encountered in the power cycles complicates the issue even further. The majority of conventional heat exchanger designs used in low temperature applications prove to be uneconomical at high operating temperatures. The high cost of exchangers in power plant applications such as supercritical CO2 Brayton cycles is a major stumbling block to making the cycle economical [34]. As a result, newer designs of heat exchangers that utilize the materials more efficiently, namely higher surface area to volume ratio designs, are being developed [34, 42]. These designs typically use microchannels as well as fin geometries to accomplish the higher area. An added advantage of smaller channel sizes is that the heat transfer in such miniature geometries is much higher [50, 51]. Advances in manufacturing processes, such as 3D printing, have helped engineers to fabricate designs which are difficult to fabricate otherwise [52, 53]. The present section reviews various heat exchanger types and designs including the conventional designs utilized in high temperature applications.

2.3.1 Plate-fin Heat Exchangers (PFHXs)

Plate-fin heat exchangers (PFHXs) are one of the most commonly utilized HXs for diverse industrial sectors. They are used mainly for gas-to-gas heat transfer applications. The main components of a PFHX, including side bars, fins, and parting sheets, are shown in Fig. 2.4. The fins are usually fabricated using a stamping process and are brazed together with the base plates. A brazed PFHX can withstand a maximum pressure of 90 bar, while diffusion bonded PFHXs can be used under pressures up to 200 bar [34]. The fins in PFHXs can be easily rearranged, which allows the PFHXs to operate in any of the cross-flow, counter-flow, or cross-counter-flow configurations. The main applications for PFHXs at high temperatures are gas turbine and power plants for hot gas heat recovery. Generally, PFHXs have a good heat transfer area to volume ratio and hence can be compact and economical for high-temperature applications [34].

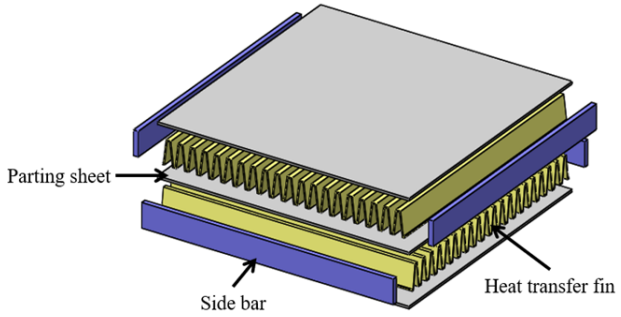

Figure 2.4: Illustration of main components of PFHX

2.3.2 Plate-and-frame Heat Exchangers

Plate-and-frame heat exchangers are often used to transfer heat between two liquids or two gases. The fluid-separating plates of these heat exchangers are typically manufactured by compression processing of a thin metal sheet, and come in several patterns such as wavy, chevron, washboard, herringbone, cross-corrugated, cross-undulated, or cross-wavy [54,55]. Two such heat transfer plates are then stacked to produce a single cell. This process is repeated to manufacture the required number of cells. The structural strength of the core is achieved through the connection of the end plates once all the cells are stacked, as shown in Fig. 2.5 [56]. For high pressure applications, the plates can be welded or brazed together to ensure operation up to 200 bar pressure and 815°C temperature [57]. Two layouts are typically used for plate-and-frame heat exchangers in recuperators in microturbine systems: 1) rectangular designs, which are installed behind the rotating machinery, and 2) annular designs, which are wrapped around the turbine [58].

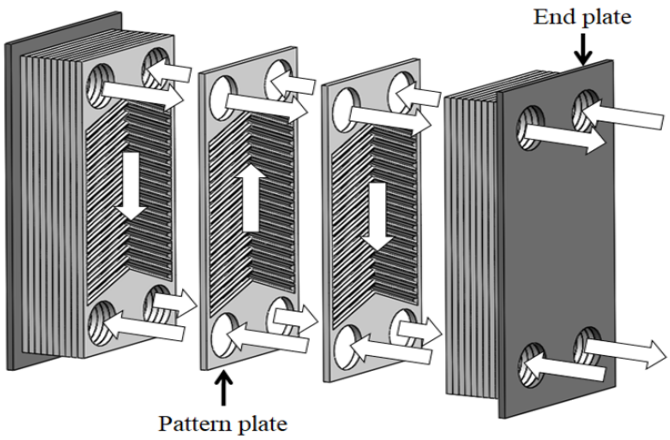

Figure 2.5: Plate-and-frame heat exchanger structure concept

2.3.3 Shell-and-tube Heat Exchangers

Shell-and-tube heat exchangers (Fig. 2.6) are the most common type used in industry. The tube diameters vary from 0.625" to 1.5" (16 mm to 38 mm) in conventional heat exchangers. These heat exchangers have very low surface area to volume ratio and hence are generally not economical for high-temperature and high-pressure applications. Chordia et al. [34], however, developed a shell-and-tube heat exchanger with a large number of tubes of diameter close to 1 mm to achieve small wall thickness and very high surface area to volume ratio. Since the channels are on the order of millimeters or less, the heat exchanger benefits from the high heat transfer. Since this type of heat exchanger can handle more severe conditions and higher pressures and temperatures, it can be used in gas turbine systems if there is no space limitation.

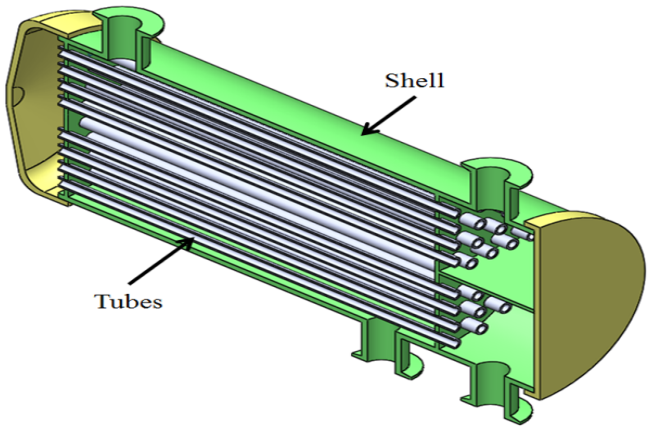

Figure 2.6: Shell-and-tube heat exchanger structure concept

2.4 HX Fabrication Using Advanced Manufacturing Techniques

Processing, machining, welding and brazing of superalloys is difficult due to their higher toughness, low thermal conductivity, tendency to crack during welding, or the unavailability of suitable brazing materials [59]. Specialized equipment and highly trained operators are often needed for processing such materials. However, new developments in advanced manufacturing techniques such as 3D printing can address the challenges faced by conventional manufacturing. This section discusses HXs fabricated using various advanced manufacturing techniques such as additive manufacturing and photo-chemical etching processes.

2.4.1 Additive Manufacturing

Additive manufacturing (AM), also known as 3D printing, emerged nearly three decades ago and was initially used mainly for quick prototyping and production of specialized parts. However, due to its high degree of freedom, especially for fabrication of complex parts, there has been significant development of industrial-scale 3D printers since then. 3D printers now can print various metals, ceramics, and other tough-to-machine materials. As a result, AM has evolved from prototyping purposes to production of complex parts used in industries such as aerospace, biomedical, oil and gas. There are three major metal-based

AM techniques: selective laser melting (SLM), direct metal laser sintering (DMLS), and electron beam melting (EBM). SLM and DMLS printers usually consist of two platforms. The first platform is a powder dispenser platform that houses the metal powder. The second platform is the build platform on which the 3D structure is built. After a layer of the 3D structure is built, the powder dispenser platform rises while the build platform lowers, so a new layer of powder can be distributed on top of the existing layer. A re-coater arm is used to uniformly distribute the metal powder, as shown in Fig. 2.7. In the case of DMLS, the metal powder is sintered using a laser just below its melting temperature. For the case of SLM, the powder is completely melted. Lenses focus the laser beam while a scanning mirror controls the beam or spot location based on a slicing of the 3D structure CAD file. The process is repeated until the entire 3D structure is built. The EBM process is similar to that of SLM. The major difference is that an electron beam is used instead of a laser to melt the powder. Due to the use of the high-power electron beam, parts fabricated using EBM will have better mechanical strength than parts fabricated using the SLM or DMLS process.

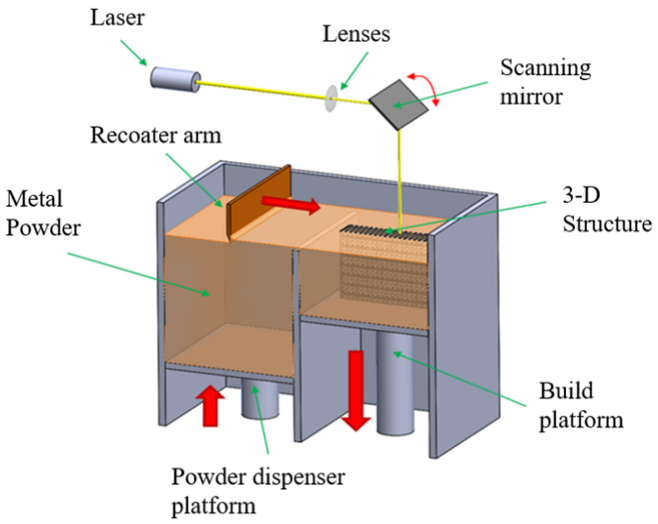

Figure 2.7: DMLS/SLM concept [60]

Laminated object manufacturing (LOM) is another AM technique capable of fabricating metal heat exchangers. In the LOM process, a 3D structure is built layer by layer by cutting a sheet of material using a laser, as shown in Fig. 2.8. A heated roller bonds the build part in the current layer onto the previous layer. The process is repeated until the entire 3D structure is built. Compared to DMLS and SLM, the LOM process is simpler and cheaper.

In addition, LOM can be used to fabricate ceramic heat exchangers. However, the finish quality and accuracy of LOM are not as good as DMLS or SLM.

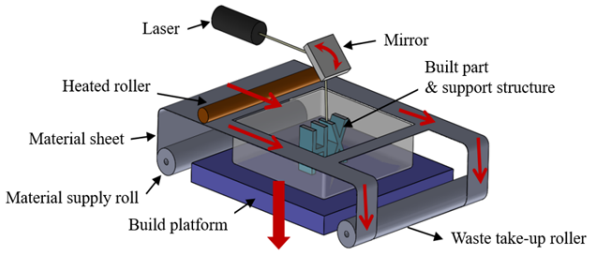

Figure 2.8: LOM process [61]

Additive manufacturing can help fabricate the complex and compact geometries of HXs which are otherwise almost impossible to fabricate. Several superalloys such as Inconel 718 and Inconel 625 are compatible with AM. It also allows fabrication of the heat exchanger as a single component, which eliminates the need to weld or braze different parts. There have been several successful attempts to fabricate HXs using AM, as summarized below.

Manifold-microchannel Heat Exchangers

The manifold-microchannel heat exchanger (M2HX) is a novel design that takes advantage of the high heat transfer rates of microchannels without the associated high pressure drops by reducing the flow length through the microchannel. However, a consequence of the short flow lengths is that the assumption of negligible spreading in the fluid-separating wall (base plate) may no longer be valid, and conventional heat exchanger correlations cannot be used to compute heat exchanger effectiveness. In the limiting case of extremely short flow lengths, spreading dominates, and a constant base plate temperature can be assumed. This is the approach taken by previous authors to determine heat exchanger effectiveness for a cross-flow M2HX currently under development for enhanced gas-to-gas heat transfer applications. In a manifold-microchannel heat exchanger, a manifold is placed on top of microchannels, as shown in Fig. 2.9. The inlet gas is then distributed into the microchannels through the manifold and travels a short length in each microchannel before it is guided out. The main advantages of the manifold-microchannel are, first, that the pressure drop in the manifold-microchannel heat exchanger can be reduced by a factor of the square of the number of divisions, due to the simultaneous reduction in both flow length and flow rate [62]. Thus, for a given pressure drop, the manifold-microchannels allow smaller hydraulic diameters than would be possible with straight microchannels, resulting

in higher heat transfer coefficients and reduced mass/volume ratio. Second, heat transfer coefficient is improved due to the short microchannel flow length, which causes thermally developing flow, which has higher heat transfer performance than fully developed flow. Third, the small fin size (< 0.3 mm in width) allows for very high heat transfer surface area per volume ratio (1000 to 2000 m^2/m^3), which renders the manifold-microchannel heat exchangers more compact than most state-of-the-art heat exchangers. Finally, using the multi-pass manifold configuration as shown in Fig. 2.9, the effectiveness of M2HX can be increased by minimizing heat spreading in the wall separating the fluid streams.

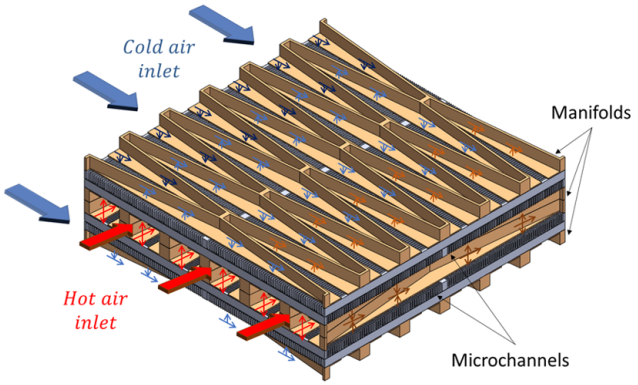

(a)

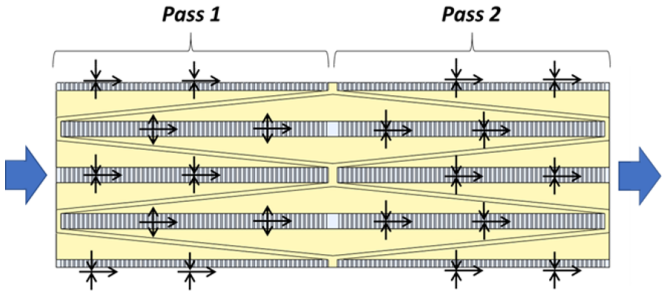

(b)

Figure 2.9: Manifold-microchannel concept: (a) isometric view; (b) top view

It is challenging to fabricate manifold-microchannel heat exchanger structures using conventional fabrication techniques, as they consist of multiple manifold and microchannel layers stacked together. Due to the small size of the microchannels, improper brazing or

welding between the manifold and microchannels can cause clogging in the microchannels resulting from a wicking effect. Metal additive manufacturing processes such as DMLS or SLM can be used to avoid this problem, as they fabricate parts layer by layer, allowing the manifold-microchannel to be fabricated as a single component and significantly simplifying the fabrication process. Many studies have been reported in the literature that discuss the superior performance of this technology compared to conventional technologies in various applications [63,64]. In those works, 50 percent or higher heat transfer was reported for the same pressure drop when compared to state-of-the-art fins such as wavy fins, louver fins, and plain plate fins. A recent work at the Advanced Heat Exchangers and Process Intensification laboratory at the University of Maryland [31] shows that a manifold-microchannel heat exchanger fabricated using Inconel 718 can achieve 30 percent less weight for the same heat transfer and pressure drop performance compared to several commercially available PFHXs for pre-cooling applications at 600°C for aircraft applications, as shown in Fig. 2.10.

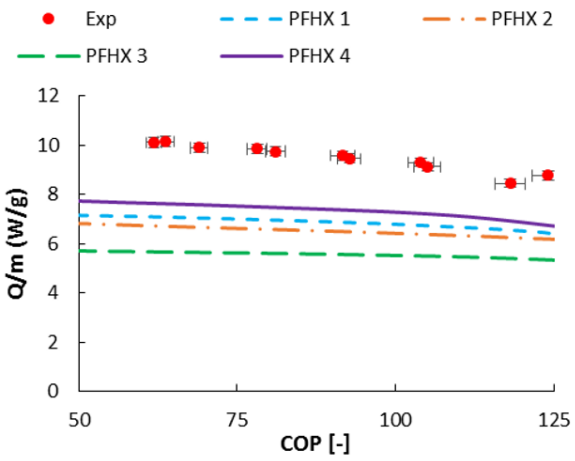

Figure 2.10: Performance comparison between M2HX with plate-fin heat exchanger (PFHX) [65]

Multi-furcating Heat Exchangers

Another type of 3D printed HX was developed by Gerstler and Erno [53] from General Electric Global Research. They successfully fabricated multi-furcating heat exchangers using SLM for fuel-cooled oil cooler applications as shown in Fig. 2.11. The heat exchanger surfaces were fabricated using four different materials: aluminum, titanium alloy (Ti64), cobalt chrome, and Inconel 718. The test results showed that the heat exchangers met the

pressure drop and heat transfer design requirement with 66% lower weight and 50% lower volume than the conventional heat exchangers.

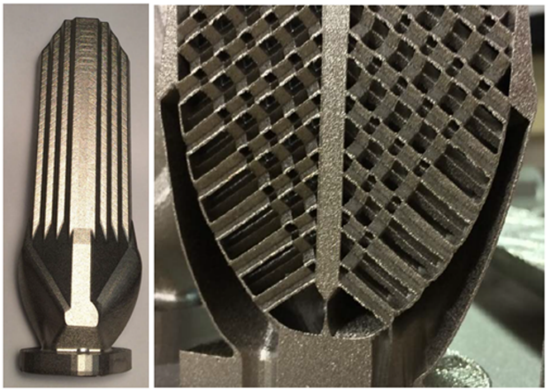

Figure 2.11: Multi-furcating heat exchanger [53]

2.4.2 Printed Circuit Heat Exchangers using Photo-chemical Etching

Photo-chemical etching is a fabrication process that utilizes a photoresist and etchants to machine away a certain area of a metal plate. The process was initially developed for fabrication of printed circuit boards. However, due to its ability to etch various metals, including titanium, nickel superalloy, and copper superalloy, and its high accuracy, the process has been used to fabricate printed circuit heat exchangers. The etching process is shown in Fig. 2.12.

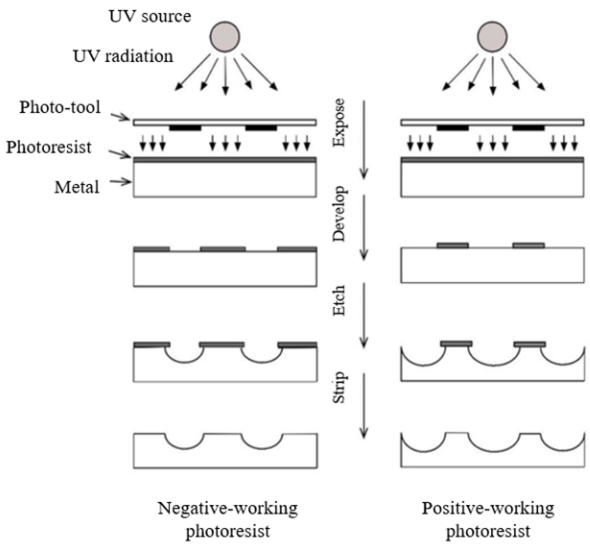

Figure 2.12: Photo-chemical etching process (adopted from reference [66])

First, a photoresist layer is deposited on the metal surface. Then, the photoresist is exposed to UV light via a photo-tool. Afterward, the exposed metal is dissolved via an etching process to form semi-circular channels with typical channel width of 0.5-2 mm [66]. Lastly, the photoresist is removed using a solution like alkaline. If the photo-tool specifies the area that needs to be dissolved by the UV light, the process is called positive-working photoresist. If the photo-tool specifies the area that is left, the process is called negative-working photoresist.

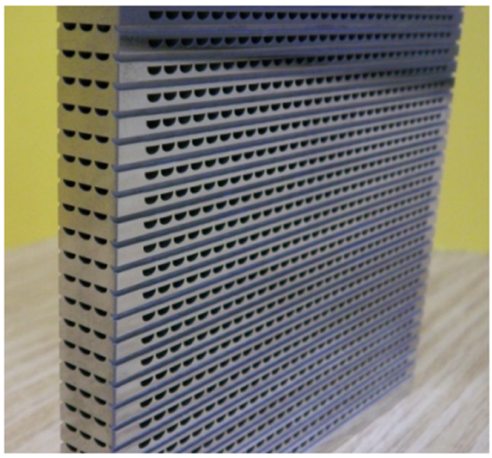

Figure 2.13: Printed circuit heat exchanger [67]

2.4.3 Ceramic Heat Exchangers

As discussed in the materials section, ceramic materials can be used for much higher temperatures than their metallic counterparts. Several different types of ceramic heat exchangers have been fabricated and tested, including ceramic PFHXs, plate and frame heat exchangers, and ceramic shell-and-tube heat exchangers [1,68–70]. Some of these heat exchangers can operate up to a peak temperature of 1370°C [68]. Slip casting, tape casting, throwing, injection molding, and dry pressing are the common processes for fabrication of ceramic heat transfer surfaces. For example, injection molding was used by Fedarzoni et al. [69] to fabricate a plate-and-frame heat exchanger out of alumina with channel size of 0.5 mm x 0.5 mm. Similarly, shape molding [70] has been used to fabricate a plate-and-frame heat exchanger; slip casting has been used to fabricate a finned ceramic shell heat exchanger [71]; and a combination of stereolithography and additive manufacturing technique with injection molding has been used to fabricate a plate-and-frame heat exchanger [1], all with features sizes as small as 250 microns.

Bonding of ceramic heat exchangers can be categorized into two categories: non-monolithic bond (non-permanent) and monolithic bond (permanent). A non-monolithic bond is a non-permanent bond whose structure can be easily de-bonded. Mechanical joints and seals are examples of non-monolithic bonds. A damaged heat exchanger fabricated using a non-permanent bond can be easily fixed by replacing the broken component. However, the bond is much weaker than monolithic bonds. Therefore, non-monolithic bonds are not suitable for high pressure heat exchanger applications. In addition, CTE mismatch

is a problem for non-monolithic bonding between two different materials. On the other hand, a monolithic bond is a permanent bond whose structure cannot be de-bonded later. Monolithic bonds offer a stronger bond compared to non-monolithic bonds. Several examples of monolithic bonding techniques include polymer infiltration and pyrolysis (PIP), tape bonding, firing, and laser brazing. PIP is the most common technique for bonding ceramic heat exchangers. The process involves deposition of low viscosity polymer between ceramic structures followed by pyrolysis. The pyrolysis is usually performed in an oxygen-free environment at temperatures of 800-1300°C. This process has been successful in bonding ceramic heat exchangers [70, 72]. These bonds were reported to tolerate pressure difference up to 9 MPa. Another technique for ceramic bonding is tape bonding. The process involves the use of sheets and ceramic powder as an interlayer bonding agent between the ceramic plates. Tape bonding is expected to provide a joint stronger than PIP. However, the process requires processing temperatures higher than PIP, which causes extensive creep on the heat exchanger. Lewinsohn et al. [73] showed that a heat exchanger fabricated using tape bonding had a higher shear strength than the one fabricated using PIP.

Ceramic heat exchangers have also been fabricated using AM. Ross et al. [74] attempted to fabricate a compact 4 cubic inch ceramic heat exchanger out of zirconia-toughened mullite (ZTM) using the LOM process. Initial delamination of the layers during the fabrication was eliminated by decreasing the binder burnout rate and adding a tape cleaning step. The heat exchanger was successfully tested at 700°C. Larger dimensions, however, were a challenge to fabricate due to the cracks caused by the defects. In another work by Alm et al. [1], a ceramic heat exchanger was fabricated using a combination of AM techniques (stereolithography) and injection molding. Additive manufacturing was used to create the injection molding mold. The use of AM allowed fabrication of the molds with feature size as small as 0.25 mm, which showed the promise of AM in ceramic HX manufacturing.

2.5 Generative Design for Heat Exchangers

Advances in 3D printing provide the opportunity to fabricate complex geometries which are too challenging using conventional manufacturing methods [5, 75–78]. Normally, limited number of manufacturable geometries as shown in previous sections are considered for the design purpose. Generative Design (GD) is a generative engine which can close the gap between flexibility provided by AM and computational design. There are several data-driven GD techniques which use a pre-existing dataset which might not be useful for many engineering design. Therefore, shape and Topology Optimization (TO) receive more

attention as mathematical methods that optimize geometry. TO has been used for decades in a wide range of industrial applications from structural to biomechanics applications [79, 80]. Generally, design optimization can be performed using size, and shape and topology optimization as shown in Fig. 2.14. Several methods have been used for TO such as density based, phase field, and shape derivative methods [13]. The density-based topology optimization procedure is the most popular method in structural optimization. Thermo-fluid design is more challenging than structural topology optimization since Navier-Stokes and convection-diffusion equations cause nonlinearity in the design problem. Particular challenges regarding boundary conditions also should be considered in heat exchanger design optimization which require a clear boundary definition [15].

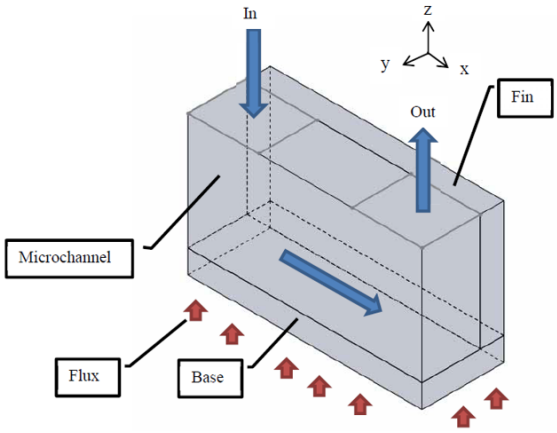

(a)

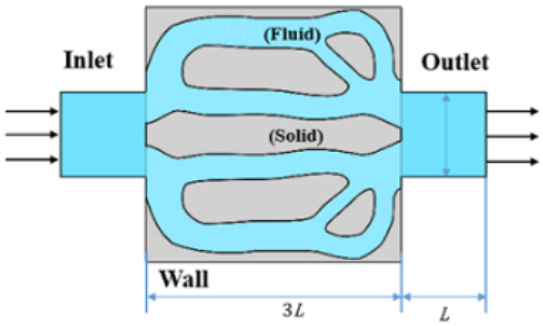

(b)

Figure 2.14: Design schematics for (a): Size optimization , (b): Shape and topology optimization [81, 82]

Pixel-based design space exploration can keep a clear boundary, but this method suffers from the curse of dimensionality. Recently, Florian et al [83] used null space and gradient methods to maintain clear shape boundaries during the shape optimization. The results presented are promising, but require further improvement in terms of constraint implementation. The state-of-the-art methods in heat transfer shape optimization rely on adjoint method which computes the derivative of the objective with respect to design variables to specify the direction of the search algorithm which could be trapped in local optimal solutions [84, 85].

2.5.1 Reinforcement Learning for Generative Design

Deep RL has been proven to be a powerful tool for robotics, navigation, and stock trading. Application of RL in shape and topology optimization was also studied by few recent studies. Deep RL was successfully implemented for modeling 3D shapes [86] as well as structural TO [87] of a cantilever with elementally discretized domain. Conventional tabular RL are only effective for the decision-making problems in which state-action pairs can be approximated and stored in arrays. While it is not hard to store all possible states and actions in memory, it is almost impossible for the RL agent to iterate over all possible states and actions to find optimal solution for a specific problem. A Deep Neural Network (DNN) acts as an approximator and estimates the values of states or state-actions. In other words, DNNs are predictors used in modern RL as an alternative to the tables to estimate the value functions or a policy. This method is useful particularly when the design space suffers from the curse of dimensionality. Aerodynamic shape optimization using degenerate deep RL was performed which shows an agent can optimize aerodynamic shapes without any prior knowledge of the final shape. Application of deep RL in a degenerate form to control heat transfer by changing position of the air supply position is demonstrated which has a wide application in indoor thermal comfort [88]. Controlling Natural convection in limited 2D square and fixed Prandtl number was successfully performed using RL [89]. Rabault et al [90] also used parallel CFD environments for active flow control. Application of RL in shape and topology optimization of heat transfer devices, however, remains intact. For heat exchanger design automation and more generally the mechanical design application, CFD solver is the limiting factor for the speed of execution because of the CPU-intensive simulation environment [91–95]. For the case of the CFD simulation, particularly shape optimization with the curved surfaces, we always deal with nonlinear data for which classical machine learning fail in practical implementation. In the next section, accelerated methods are discussed that can provide more data for policy learning in RL and engineering design.

2.5.2 Accelerated Computation for Iterative Engineering Design

As it was mentioned, engineering design often require Finite Element Analysis (FEA) or CFD to assess the performance of the output design which is a restricting factor of using RL in GD [96]. These numerical approaches are computationally expensive and require human expertise [7]. Gaussian process regression also known as Kriging metamodel in CFD community was conventionally used as a geostatistical estimator of the CFD computation to accelerate design automation [97, 98]. Modern ML, however, opened a new pass toward surrogate modeling. Convolutional Neural Network (CNN) is a class of DL which has gained popularity in recent years with numerous applications in computer vision, radiology, and most recently in CFD and design community [99–104]. CNN can recognize features in variable 2D shapes which makes it an appropriate model to predict simulation results of different physical shapes [8, 96]. CNN also benefits from parameter sharing which leads to smaller number of trainable parameters compared to Fully Connected (FC) Layers [105]. Guo et al. [106] suggested CNN surrogate model to predict steady state laminar velocity profile generated using Lattice Boltzmann Method (LBM). They used CNN operating on Signed Distance Functions (SDFs) sampled on a 2D grid. Several research studies have been carried out to accelerate time-dependent CFD simulation [107–109]. Accelerated CFD models using CNN were introduced for turbulent flow prediction without the presence of boundaries which results in faster simulation even with fine grids [110]. These models have wide applications in fluid flow prediction particularly in weather forecast that there is no complex boundary condition or complex topology. Google Deepmind reported a model for velocity and pressure prediction of two dimensional fluid flow of a cylinder with 1-2 orders of magnitude faster computation than the finite element solver [111]. Continuous convolutions are used for Lagrangian fluid simulation without the presence of morphing shapes [112].

U-Net architecture was used as a tool to reconstruct the CFD results of cylinder flow [113, 114]. Regular CNN was also used for pressure prediction in flow around a cylinder [115]. CNNs were applied to two dimensional velocity field estimation of blood flow in artificial lungs using a dataset with the size of 5000 cases [116]. Generation of high fidelity velocity field from low fidelity data was studied using GANs [117]. A data-driven model based on FC layers for drag prediction of rectangular obstacle with different aspect ratios representing building geometry was reported with as low as 3.17% error in prediction [118]. Graph Neural Network has also shown promising results as a fluid dynamics surrogate model in predicting next-step velocity profile for time-dependent flow [119–121]. The effort in time-dependent accelerated CFD is to minimize error accumulation that occurs during timesteps of the estimation [110, 122]. Error accumulation in next-step pre-

diction particularly in turbulent flow causes distortion from ground truth values after few timesteps. Han et al. [122] used pivotal nodes to summarize information of graphs acquired from mesh representation into a latent vector and predicted the next-step velocity using FC layers. The information is then decoded through the pivotal nodes. This method reduced error accumulation and computational cost associated with transient physics prediction.

In design optimization process, time-averaged properties are favorable [100, 123, 124]. Viquerat et al. [8] used VGG network for drag prediction of the shapes generated using bezier curve at low Reynolds and steady state condition. Zhou and Ooka used FC layers to predict CFD results for fixed cubic geometry for indoor air flow application [125]. They used parameters of the physics as the input of the neural network and velocity and temperature tensors as the output. They reported less than 12% error for thermal distribution prediction. Neural Network in FC form was also used for drag coefficient prediction of multiple shapes representing cars [126]. Inter-vehicular distance was used as the input of the model to predict drag coefficient.

2.6 Conclusion

In this chapter, a review on heat exchanger design and manufacturing was presented starting from traditional to generative designs. Recent studies in RL and surrogate models in engineering design were also discussed.

Chapter 3

Heat Exchanger Size Optimization and Process Development

3.1 Introduction

This chapter presents the usage of genetic algorithm for the size optimization of Manifold-Microchannel Heat Exchangers (MMHXs) which was introduced in chapter 2. Manufacturing and process development for size optimized novel MMHX is introduced. Direct Metal Laser Sintering (DMLS) is used to fabricate compact MMHXs. Compared to the state-of-the-art heat exchangers, MMHXs have been proven to yield superior performances [63,64]. However, fabrication of manifold-microchannel heat exchangers using conventional fabrication methods is a challenge due to their complex geometry. Additive manufacturing processes, like DMLS, allow fabricating the MMHX as a single component, which significantly simplify its production process. Part of this chapter is base on IEEE ITherm Conference paper entitled "Additive manufacturing of compact manifold-microchannel heat exchangers utilizing direct metal laser sintering" [75].

3.2 Manifold-Microchannel Heat Exchanger

The MMHX is a novel heat exchanger design that can enhance heat transfer and reduce pressure drop, compared to state-of–the-art HXs. Manifold-microchannel geometry is composed of a manifold on top of array of microchannels for better flow distribution, and shorter flow in the microchannels, as shown in Fig. 3.1. The short flow length can

significantly reduce the pressure drop and enhance the heat transfer by forcing the flow in the developing region. A more detailed description of MMHX is presented by Ohadi et al. [64].

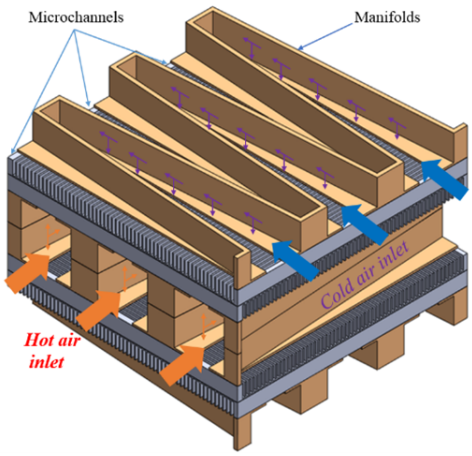

Figure 3.1: Manifold-microchannel design schematic

Fig. 3.1 shows the design schematic of the fabricated MMHX, with straight fin and straight manifolds. Previous works fabricated MMHX with inclined fins and inclined manifolds due to fabrication limitations, as reported in [65]. In this work, the manufacturing process has been improved using a different building orientation, to allow fabrication of straight fins and manifolds.

3.3 MMHX Size Optimization

In order to fully utilize the performance potential of MMHXs, a design space is considered for exploration using genetic algorithm and a Fluent CFD solver. The design space is shown in Fig. 3.2. Heat transfer and pressure drop inside manifolds were calculated using an approximation method introduced and validated by multiple studies [62,127]. The detail description of the method can be found in Ref. [60]. Single microchannel CFD results were computed using Fluent commercial software. The height, width, and length of the channel and manifold along with the mesh generation were controlled by changing the position of the points in MATLAB. The constructed geometry and mesh file were feed to the Fluent software for CFD results in microchannel part. The size optimization framework is shown

in Fig. 3.3. The objective of the size optimization is to maximize the heat transfer so that the overall effectiveness of the heat exchanger is above 90% while the pressure drop remains lower than 30% of the system pressure. The Kriging metamodel toolbox in MATLAB is used for the metamodel creation [128]. The metamodel prediction is validated by the actual values from CFD and hybrid method as shown in Fig. 3.3. Once this single cell is optimized, the overall heat transfer and pressure drop will be computed based on the number of single cell used in the design.

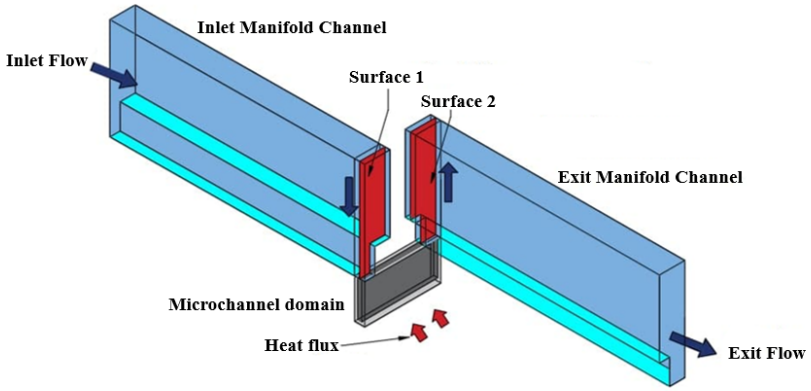

Figure 3.2: Schematics of the design domain for MMHX size optimization

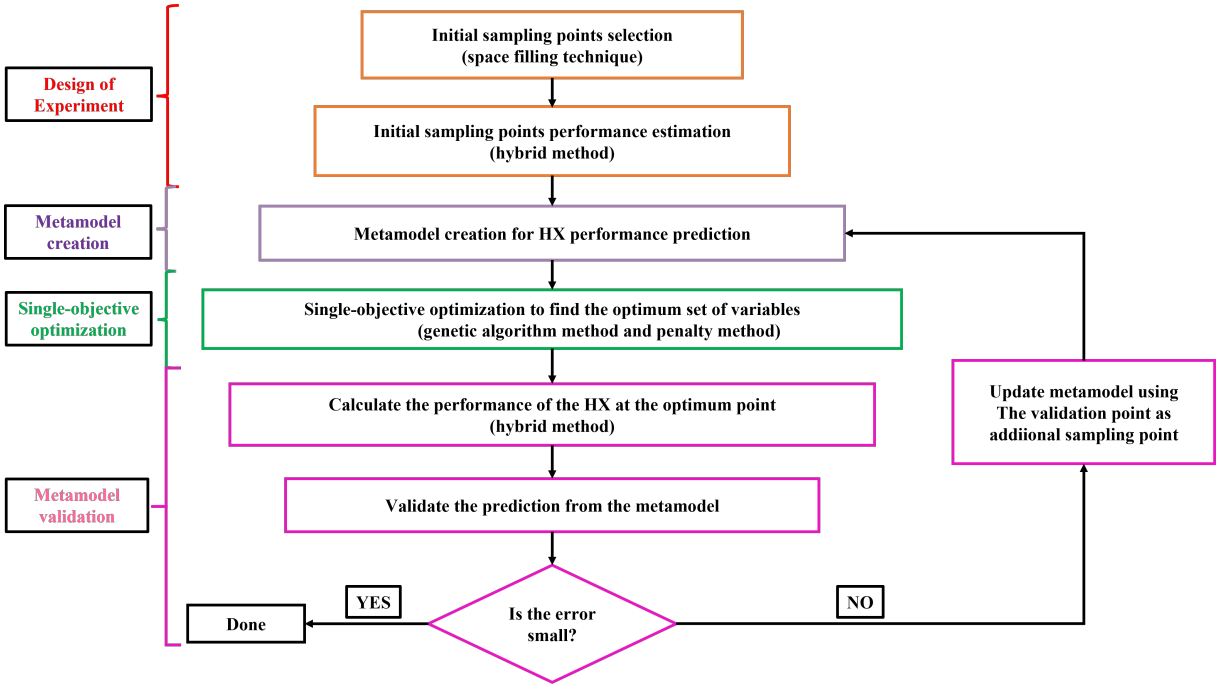

Figure 3.3: MMHX size optimization framework

Since the majority of the mass, space, and pressure drop is specified to manifold, small fins (0.1-0.2 mm) and channels (0.2-0.3 mm) are required to reach the target heat transfer. Therefore, three different 3D printing machines were used to study the effect of geometries and printing parameters, such as laser power, powder size, and layer thickness, on the fins and channel size of the fabricated microchannel heat exchangers. A comprehensive study has been performed to achieve fin thickness as small as 0.110 mm.

The minimum base thickness, which separates the hot and cold streams, plays an important role. The base thickness needs to withstand the designed pressure, thus ideally increasing its thickness. However, the thinner the base, the more reduction in mass is achieved, without affecting the thermal performance. Base thickness study is a crucial optimization problem sice it balances the need to withstand high pressure and lower cost. In the current work, multiple MMHX coupons were fabricated with different fin thicknesses to determine the smallest fins that AM can successfully fabricate. A similar approach was applied for the pressure test coupons. The lessons learned were used to fabricate a 3"×3" ×3" size and a 4" x 4" x 4" MMHXs with straight fins and straight manifolds. Pressure containment tests were also performed to evaluate the minimum base thickness that can hold the designed pressure. A 3"×3" ×3" size microchannel heat exchangers was then

successfully fabricated with straight fins of 0.133 mm out of Maraging Steel, and a 4"×4" ×4" size microchannel heat exchangers was successfully fabricated with fin size of 0.22mm out of Inconel 718.

3.4 Fabrication Orientation

In order to successfully print MMHXs using DMLS, fins' angle with respect to the build plate should not be less than 45°. Otherwise, support structure will need to be added. Since support removal from the interior structure of MMHXs is not possible, fins should be placed in more than 45° angle. A cross flow MMHX consists of fins in both the hot and cold sides, which are perpendicular to each other as shown in Fig. 3.1. Therefore, for successful fabrication, the MMHX should be fabricated at 45 degree angle with respect to the build plate as shown in Fig. 3.4. In this orientation, fins in both sides will be fabricated at 45° angle. Additionally, in order to anchor the HX to the build plate, support structures should be placed between the plate and the interface of the MMHX, that is faced downwards, as shown in Fig. 3.4.

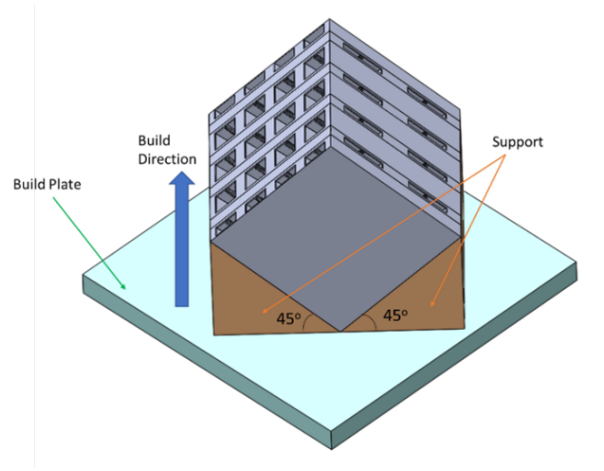

(a)

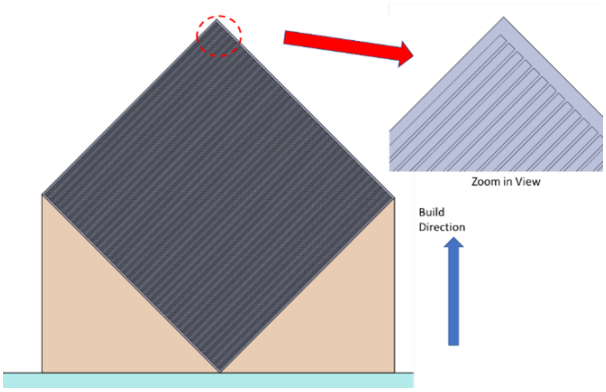

(b)

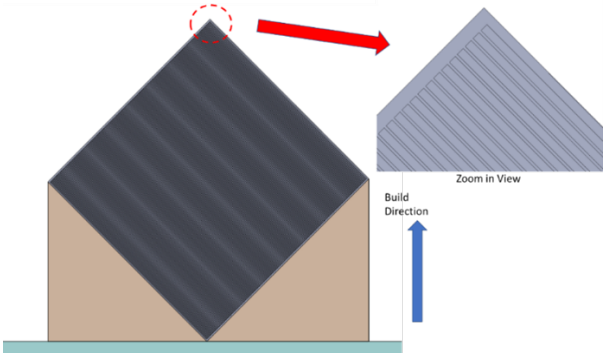

(c)

Figure 3.4: Build orientation: (a) Complete View (b) Cross-section view – Cold-side fins (c) Cross-section view – Hot-side manifold

3.5 Fin Thickness Study

In order to evaluate the capability of AM to fabricate MMHX with small fin size, multiple coupons with different fin thicknesses and channel sizes were fabricated using different 3D printer machines. These coupons were fabricated in the same orientation as the full scale MMHX (see Fig. 3.4), to be representative of the final HX. A schematic drawing of the fabricated coupon and its printing orientation are shown in Fig. 3.5. The coupon consists of fins with three different sizes: 0.100 mm, 0.125 mm, and 0.150 mm. They are separated by a thick wall for convenience of measurement. Fin spacing is considered to be constant and equal to 0.260 mm, thus the channel width varies between 0.110 mm, 0.135mm, and 0.160 mm for section with fin thickness of 0.150 mm, 0.125 mm, and 0.100 mm respectively. Multiple coupons with the same design and orientation as shown in Fig. 3.5 were fabricated using ProX DMP 200, ProX DMP 300, and EOSINT M 290 3D printer. Table 3.1 lists the material used for each print, the maximum printer build size and the layer thickness. Fig. 3.6 shows the fabricated fin thickness compared to the design fin thickness, for different 3D printer machines.

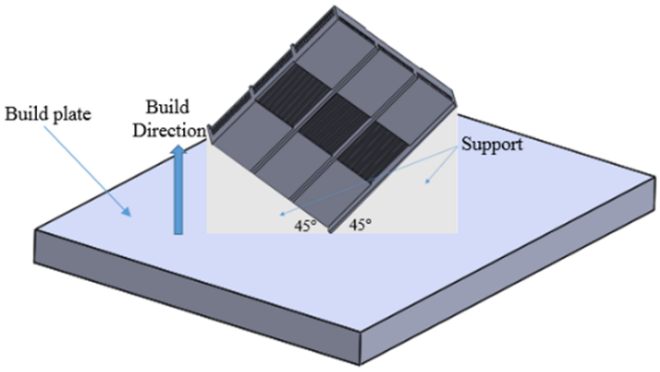

(a)

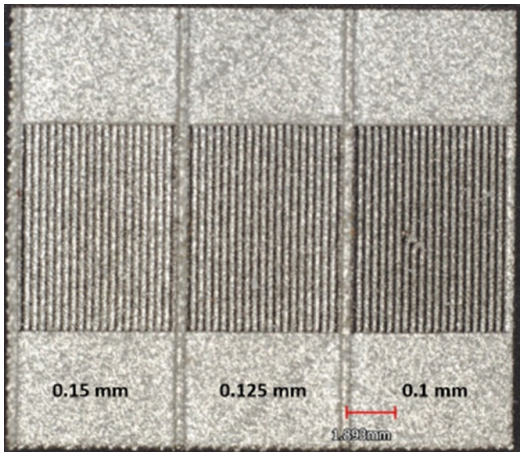

(b)

Figure 3.5: (a) Build orientation for fin thickness study coupon and (b) image of the printed coupon for fin thickness study

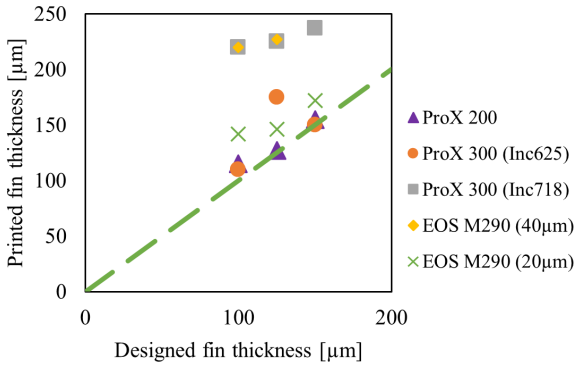

Figure 3.6: Printed fin thickness versus design fin thickness for different 3D printer machines

Table 3.1: Printers details including material used, maximum build size and layer thickness

Printer Model	**Material**	**Printer build size [inch3]**	**Layer thickness [µm]**
ProX 200	Maraging Steel	$5.51 \times 5.51 \times 4.92$	30
ProX 300 (Inc625)	Inconel 625	$9.84 \times 9.84 \times 13$	40
ProX 300 (Inc718)	Maraging Steel	$9.84 \times 9.84 \times 13$	40
EOS M290 (40µm)	Inconel 718	$9.85 \times 9.85 \times 12.8$	40
EOS M290 (20µm)	Inconel 625	$9.85 \times 9.85 \times 12.8$	20

Fig. 3.6 shows that ProX 200 machine has the best concurrence between the design fin size and actual fin size. This result can be understood by checking the information reported in Table 1. First, Maraging Steel is easier to be worked with, due to lower tensile stress properties and thermal resistance to high temperature when compared to superalloy. Second, the printer has a smaller build volume, meaning the distance between the laser and the build plate is smaller compared to the other printers. This allows a higher resolution in the printing feature. Third, the layer thickness is smaller than the conventional 40 µm. The printer was used as an initial test because it is located at the University of Maryland, College Park (MD) and it is easily accessible for the authors of this work. Despite these promising results, Maraging Steel is not suitable for high temperature applications which require superalloy materials. Maraging Steel, in fact, has a maximum service temperature of 400°C, while Inconel 625 and 718 can withstand up to 900°C [19]. On the other hand, the need for a bigger printer to accommodate bigger HX (considering the build orientation negatively affects the build size requirement) led to exploiting other machines and different

materials. ProX 300 machine has been investigated in two different configurations. ProX 300 (Inc625) showed a small deviation from the fin design values for 0.100 and 0.150 mm, but a significant deviation for 0.125 mm. The lack of consistency in the printer can become an issue when printing bigger part. On the contrary, ProX 300 (Inc718) showed a more consistent trend, but the deviation from the desired values has to be carefully taken in consideration during the design stage: knowing that the printed part will be bigger than the CAD file, the features need to be designed smaller to mitigate the deviation. A similar trend was also shown by EOS M290 (40µm).

3.6 Layer Thickness Effect on Fin Size

As shown in Fig. 3.6 when comparing EOS M290 (40µm) with EOS M290 (20µm), a significant improvement in the fin thickness can be obtained when reducing the layer thickness. Changing the layer thickness of Inconel 625 from 40 to 20 µm allows to get feature size deviating only 20 µm, which is the particle size itself. Both powder sizes show consistency in the trend, making EOS M290 a more robust machine, which requires smaller layer thickness to get the same results in terms of fin resolution. The drawbacks of reducing the powder size are longer printing time (double, if halving the powder size) and higher cost, due to more expensive powder and longer printing time. Smaller powder size has therefore to be selected only in those cases where resolution and consistency are needed to their maximum capabilities.

3.7 Laser Power Effect on Fin Size

Printing parameters can be adjusted by machine operator and can significantly affect the quality of the printed parts [129]. Laser power is a crucial factor that affects the fabrication quality of the parts, printed using DMLS. The effect of laser power on the fins' size was investigated through printing multiple single manifold-microchannel coupons using Maraging Steel for the PROX 200 at University of Maryland, College Park, as shown in Fig. 3.7. Six coupons were fabricated with three different fin sizes and two different laser power settings, as shown in Fig. 3.7.

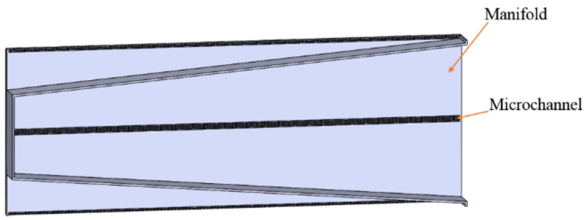

(a)

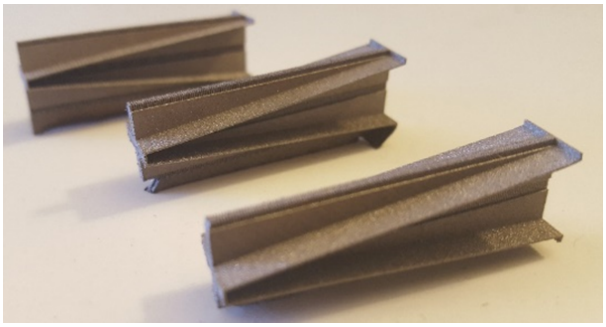

(b)

Figure 3.7: (a) CAD model of a single manifold-microchannel , and (b) Picture of single manifold-microchannel fabricated at different laser power

Table 3.2: Effect of laser power on the fin size (sizes in µm)

Design fin thickness	**300 W laser power**	**225 W laser power**
100	133	115
125	156	131
150	188	157

Table 3.2 shows design fin thickness and fabricated fin thickness which were fabricated using 300 and 225 W laser power setting in ProX 200 machine. It can be concluded that smaller fins size can be fabricated using smaller laser power. This is due to the fact that, the higher the laser power, the larger the melting pool, and the more difficult it is to fabricate fine features. Fig. 3.8 shows the microscopic image of the fins of 115 µm size.

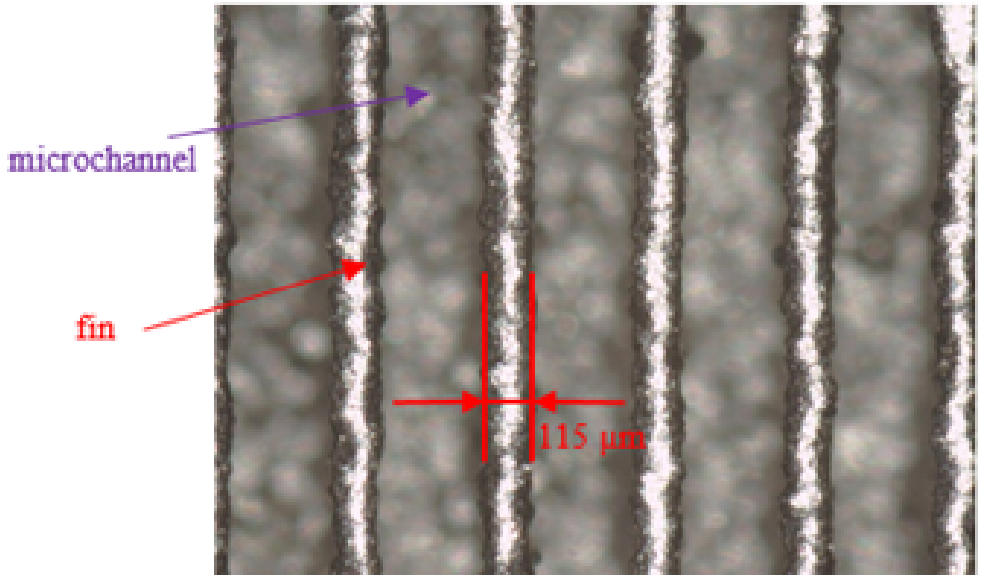

Figure 3.8: Microscopic image of the fins with 115 µm thickness

3.8 Base Thickness Study

Another important design limitation is the minimum base thickness that is required to withstand the pressure. Ideally, the smaller the base, the better results the HX can provide, both in terms of thermal performance and mass reduction. Reducing the base thickness, in fact, allows to minimize the thermal resistance due to the conductive term. At the same time, a reduction in the base requirements positively affect the total mass of the HX. However, there are some limitations faced when using AM. In fact, the part is obtained by sintering metal powder into a single structure. During this process some impurities can be trapped in the structure and porosity can affect the product quality. This may result in a final component that withstand pressure requirements differently, or less than the component fabricated conventionally from bulk material. In order to study this behavior, a series of coupon with different base thicknesses were printed, as shown in Fig. 3.9. Each coupon consists of a chamber and a pipe connection through which it is possible to connect the coupon to the pressurized system. The fittings were machined to guarantee perfect sealing during the pressure containment test. The printers selected for this study were the ones giving the most consistent results during the fin thickness study: ProX 300 (Inc718) and EOS M290 (20µm). Each machine printed three coupons, of chamber walls of respectively 300, 350 and 400 µm, as reported on each coupon (see Fig. 3.9).

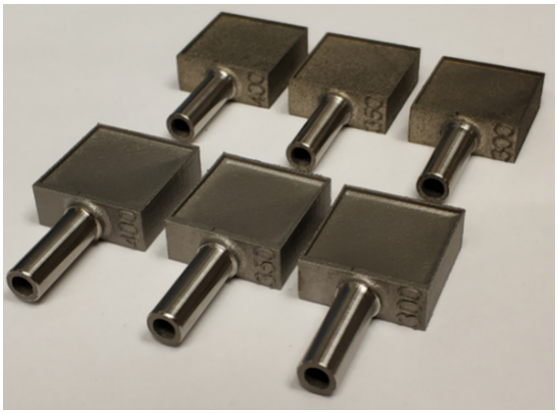

Figure 3.9: Pressure check coupon sets. Front line set: ProX 300 (Inc718), back line set: EOS M290 (20µm)

Layer thickness effect on base thickness size High temperature HXs for airplane applications generally operate under 50 psia (339 kPa) pressure. For this reason, the six coupons were pressurized under the design condition, using nitrogen as test medium. The test results are shown in Table 3.3.

Table 3.3: Results of pressure containment check coupons

Design base thickness	**ProX 300 (Inc718)**	**EOS M290 (20µm)**
300 µm	Small leakage	No leakage
350 µm	No leakage	No leakage
400 µm	No leakage	No leakage

As reported in Table 3.3, EOS M290 (20µm) proved the capability of printing three pressure tight coupons, demonstrating dense structures for the three selected base thicknesses. ProX 300 (Inc718) failed in the smallest base thickness selected. As expected, moving from 40 to 20 µm layer thickness proved to give better results. The requirement to lower the layer thickness to obtain leak proof HXs, varies based on the pressure selected. For the current study, the selected pressure of 50 psia (339 kPa) necessitated moving from 40 to 20 µm layer thickness, when printing base thickness smaller than 350 µm. A direct measurement of the base thickness is not possible without cutting the coupons. The "indirect" method used to validate the printed base thickness was based on the volume check of the coupons. The volume of the coupons was measured using Archimede's principle through a precision dynamometer. The liquid used for these measurements was ethyl-alcohol 200

proof. Having a lower surface tension than water, ethyl-alcohol 200 proof becomes a better choice, making sure that air microbubbles do not attach to the internal parts, thus compromising the results. The volume calculated was then compared to the design volume. For both printers, the deviation from design to actual volumes was in the order of 2-3%, which falls under the uncertainty of the measurements (in the order of 3%). By this, the results obtained for the coupons are considered as similar to the actual dimensions.

3.9 MMHX Units Fabrication

MMHX fabrication was performed through multiple steps from small heat exchanger units to a larger scale HX. Fig. 3.10 shows three MMHXs fabricated out of Maraging Steel using ProX 200, and one MMHX fabricated out of Inconel 625, using ProX 300 (Inc718). In order to fabricate a 3" x 3" x 3" size MMHX, which is the maximum build size capability of ProX 200, multiple coupons were fabricated from small to larger size. To investigate whether the heat exchanger was leak free, a 1" x 1" x 1" MMHX was fabricated and leak tightness was proven through a leakage test, based on pressurizing the HX with air. Based on this promising result, two larger MMHXs with the size of 2" x 2" x 2" and 3" x 3" x 3"were fabricated.

(a)

(b)

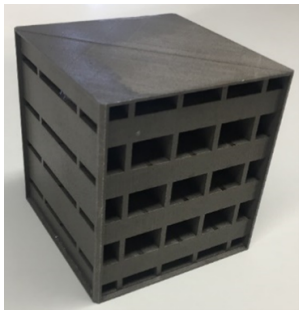

(c)

(d)

Figure 3.10: Image of the (a) 1"×1"×1", (b) 2"×2"×2", (c) 3"×3"×3" MMHX unit fabricated out of Maraging Steel, and 4"×4"×4" MMHX fabricated out of Inconel 625

In order to investigate the quality of the fabricated MMHX, the 2" x 2" x 2" MMHX was cut. The cut section image of the is shown in Fig. 3.11. By analyzing the cross section view, it can be seen that the fins are successfully fabricated without clogging or defects.

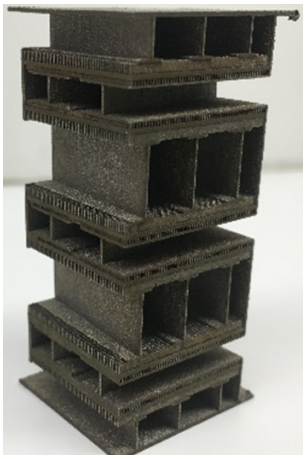

Figure 3.11: Cut view of 2” x 2” x 2” MMHX (Fig. 3.5(b))

Based on the knowledge learned from the fin thickness study, the fins were designed at 0.100 mm. The fin size of the three Maraging Steel MMHXs were measured to be between 0.110 and 0.130 mm, which is consistent with the results of the fin thickness study. This successful fabrication of straight fin and straight manifold MMHX, with fin size as small as 110 µm, can significantly enhance the performance of the MMHX. ProX 300 (Inc718) machine was used to fabricate the 4” x 4” x 4” MMHX. In order to fabricate this MMHX with a minimum fin thickness, the designed fin thickness was set at 0.100 mm. The actual fin thickness of the 4” x 4” x 4” MMHX fabricated using ProX 300 (Inc718) was then shown to be 0.220 mm. All of the fabricated MMHXs have been tested to prove leak tightness under the designed pressure, confirming also the base thickness results.

3.10 Conclusion

A size optimization framework along with the process development of metallic MMHXs were introduced. With the use of genetic algorithm and a hybrid CFD model, as well as DMLS fabrication method, MMHXs were optimized and fabricated for a target design performance. In order to achieve high performance for the MMHX, the fin needs to be fabricated as thin as possible. The base also needs to be fabricated as thin as possible to have no leakage. A study was performed to determine the smallest fins size that can be fabricated using DMLS. Multiple coupons with different fins sizes were printed using multiple printers with different printer parameters. The results show that fins as small as 0.110 mm can be fabricated using the ProX 200. ProX 300 and EOS M290 machines

are less accurate in printing small fins, but can accommodate bigger HXs. Reducing the layer thickness and laser power can improve the fabrication quality. The superior results are also reflected in the leak-proof minimum base thickness. For 50 psi (339 kPa), a base thickness of 300 µm proved to be leak-proof. Based on the knowledge acquired from the coupons study, multiple MMHXs were fabricated starting from smaller size of 1"x 1" x 1" up to a 4" x 4" x 4" HX. Leak tightness of the MMHXs have been proven through leakage test under design pressure.

Chapter 4

BREP-based Generative Thermal Design Utilizing Single-Agent Deep Reinforcement Learning

This chapter presents a parametric approach for heat exchanger shape optimization utilizing deep RL and BREP. It is shown that continuous geometric representation of the fluid and solid domain facilitates the implementation of boundary conditions and design space exploration in contrast to traditional TO. The proposed framework consists of a Deep Neural Network (DNN), and a CFD solver with an automatic body-fitted mesh generation to solve a single fin shape optimization. The learning is performed using Proximal Policy Optimization (PPO) in combination with a CFD environment in FEniCS. The RL agent successfully explores the design space and maximizes heat transfer and minimizes pressure drop for geometric design with as low as 12 degrees of freedom represented by composite Bézier curves. Higher degree of freedom results in higher reward of the agent. This method alleviates the curse of dimensionality compared to voxel and pixel-based optimization of coupled thermal fluid-structure. Results show the manufacturability and efficiency of the output of the presented framework. Over 30 percent improvement in overall heat transfer while lowering the pressure drop by more than 60 percent compared to the rectangle reference geometry is achieved. Part of this chapter is based on a peer-reviewed article published in "International Journal of Heat and Mass Transfer" entitled "Deep reinforcement learning for heat exchanger shape optimization" [130].

4.1 Introduction

In this chapter, a new approach for generative design of heat exchangers using deep RL and parallel computing is proposed. Parallel training is a useful tool that can be used in conjunction with an on-policy algorithm called PPO. Introduced workflow is designed to perform CFD in multiple parallel environments. BREP-based geometry is used to reduce the dimension of the problem with reducing the design parameters to a number of control points that construct the geometry. This method provides continuous solid-fluid interface to support shapes beyond Euclidean geometries on which boundary condition could be applied. It is shown that an autonomous agent controlled by the developed algorithm observes the CFD environment defined in FEniCS, an open-source software, and provides actions to optimize the geometry of the fin. Parallel computing has been used for simulation to provide the data required for PPO algorithm. Utilizing the proposed methodology presented in this chapter enables the moving surfaces in BREP to be the main optimization variable. The mathematical precise definition of the surfaces controlled by points makes the output geometry an ideal design for manufacturing purpose particularly in microchannel design. In density-based methods such as SIMP method or Navier-Stokes/Brinkman model, however, the computational domain is considered a porous media without a clear interface representation of the solid and fluid-structure. The free form nature of density-based methods, impose manufacturing challenges particularly in heat exchanger applications. Parametric optimization in combination with reinforcement learning alleviates undesirable shapes considering penalties for certain area of the design space. Recent advancement in Learning from BREP provides effective function approximation which can accelerate the optimization [131].

4.2 Methodology

The focus of this chapter is to present a model for conjugate heat transfer of laminar incompressible fluid in a constraint heat exchanger. The design space is a two dimensional space $D = \overline{\Omega_f} \cup \overline{\Omega_s} \subset \mathbb{R}^2$ occupied by a solid, and an incompressible fluid. The solid component Ω_s consists of composite Bézier curves controlled by moving control points which causes incremental changes in the fluid domain Ω_f. Defining geometry using BREP facilitiates mathematical implementation of moving boundary conditions during incremental changes in the computational domain.

4.2.1 BREP-based Geometry

Curves can be defined as implicit, explicit, or parametric. Here, the focus is on parametric expression of curves which is mostly used in computer graphics and geometric modeling. Composite Bézier curves are parametric curves initially used for designing body of cars and later in Computer Aided Design (CAD) and Robotics [132]. A composite Bézier curve is a piecewise Bézier curve where the initial and final points are joined together to form a continuous geometry. These curves have also been used in image manipulation and Generative Adversarial Network (GAN) for design space exploration [133]. In this chapter, geometries are defined utilizing the composite Bézier curve because its mathematical definition facilitates the implementation of iterative process and defining b-spline kernels for future consideration of Geometric Deep Learning. The key component that makes composite Bézier curves well-suited for shape optimization is the continuous derivative on the curve which is extremely useful for Neumann boundary condition implementation. The original Bézier curve with a set of control points P_i with n+1 parameters are defined as following:

$$\alpha(u) = \sum_{i=0}^{n} P_i B_{i,n}(u); u \in [0,1] \tag{4.1}$$

where $B_{i,n}(u)$ is the i'th function of degree n defined by Bernstein polynomials

$$B_{i,n}(u) = \binom{n}{i} n^i (1-u)^{n-i}; i = 0, .., n \tag{4.2}$$

4.2.2 CFD Environment

A CFD environment is created for the design space which is shown in Fig. 4.1. Internal square shows the design space in which the agent receives a reward where the rectangle space is the total design space. The ratio of the spaces are shown in Fig. 4.1. The environment is written utilizing FEniCS open source software all in python [134]. FEniCS is based on the Finite Element Method(FEM) used to solve the governing equations 4.3 and 4.5 given bellow. Boddy-fitted mesh generation of the geometry is performed in GMSH [135]. The robustness of these packages have been demonstrated by several studies [136, 137].

Eq.4.3 and Eq. 4.5 formulate the incompressible Navier-Stokes equation, and convection-diffusion equations (effects of gravity on momentum is considered to be negligible)

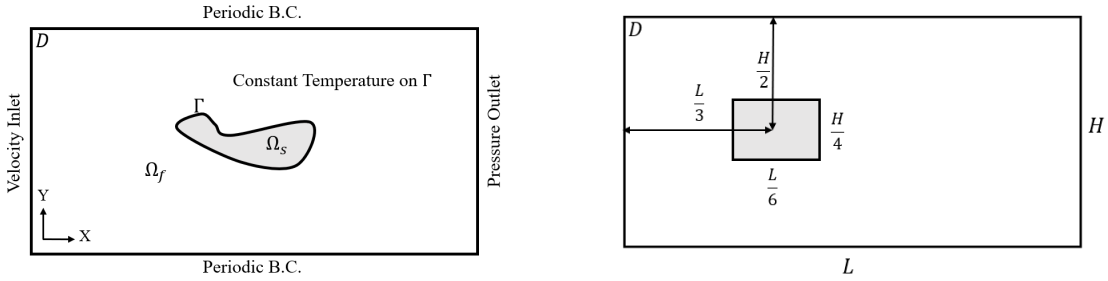

(a) (b)

Figure 4.1: Setting of design space exploration (a): Rewarded design space represented by boundary Γ, (b): Total design space

$$\begin{cases} \rho\frac{\partial \boldsymbol{u}}{\partial t} + \rho((\boldsymbol{u}\cdot\nabla)\boldsymbol{u}) - \nabla(\sigma_f(\boldsymbol{u},p)) = 0 \quad in \quad \Omega_f \\ \nabla\cdot\boldsymbol{u} = 0 \quad in \quad \Omega_f \\ \boldsymbol{u} = \boldsymbol{u}_0 \quad on \quad \Omega_{f,in} \\ \sigma_f(\boldsymbol{u},p)\cdot\boldsymbol{n} = 0 \quad on \quad \Omega_{f,out} \\ \boldsymbol{u} = 0 \quad on \quad \Gamma \end{cases} \tag{4.3}$$

Where $\sigma_f(\boldsymbol{u},p)$ is considered as Newtonian fluid:

$$\sigma_f(\boldsymbol{u},p) = 2\nu e(\mathbf{u}) - pI, e(\boldsymbol{u}) = \frac{1}{2}(\nabla\boldsymbol{u} + \nabla\boldsymbol{u}^T) \tag{4.4}$$

In which I is the identity matrix and p $\equiv p(\Omega_f)$ is the pressure.

$$\begin{cases} \rho c_p\frac{\partial T}{\partial t} + \rho c_p(\boldsymbol{u}\cdot\nabla T) - \nabla\cdot(k_f\nabla T) = 0 \quad in \quad \Omega_f \\ T = T_{in} \quad on \quad \Omega_{f,in} \\ T = T_0 \quad on \quad \Omega_{f,t=0} \\ T_f = T_s \quad on \quad \Gamma \\ -k_f\frac{\partial T_f}{\partial n} = -k_s\frac{\partial T_s}{\partial n} \quad on \quad \Gamma \end{cases} \tag{4.5}$$

Where $\boldsymbol{u}$ is the velocity field, and T is the temperature,

Traditionally, Finite Volume Method (FVM) was used more frequently for CFD computation; Traditional FEM without standardization struggled to solve CFD problems due to

the nonlinearity of the convection term which makes the problem unsymmetrical. However, recently, FEM has widely been used in both academia and commercial software packages because of the geometric flexibility of the method and advancement in computer hardware [138, 139]. In this study, we use FEM to solve discretized Navier–Stokes and convection-diffusion equations along with BDF2 time scheme for Navier–Stokes equations and BDF1 time scheme for convection-diffusion equation. The numerical timestep is considered according to convergence condition by Courant–Friedrichs–Lewy. The weak form of equations are given in A.1

Periodic boundary condition is implemented in the vertical direction. Dirichlet boundary for the fluid variables $\boldsymbol{u} = \boldsymbol{u}_0 = 1m/s$ is considered for the inlet flow as well as Neumann boundary for the fluid variables $\sigma_f(\boldsymbol{u}, p) \cdot \boldsymbol{n} = 0$ at the outlet. Isothermal boundary for the inlet temperature and solid-fluid interface is considered $T_{in} = 27\,^{\circ}\mathrm{C}$, $T_s = 177\,^{\circ}\mathrm{C}$, respectively.

Heat transfer and pressure drop across the domain are computed by Eq. 4.6 and Eq. 4.7. Final time of the computation is considered to be twice the value of the number of timesteps required for convergence based on the Courant–Friedrichs–Lewy condition. Average values are obtained from Eq. 4.6 and Eq. 4.7 between the inlet and outlet boundaries specified in Fig. 4.1 over the final half of the computation.

$$Q(\Omega_f, \boldsymbol{u}, T) = \int_{\partial\Omega_f} \rho c_p T \boldsymbol{u} \cdot \boldsymbol{n}\, dy \tag{4.6}$$

$$DP(\Omega_f, p) = \int_{\partial\Omega_f \cap \partial\Omega_{f,in}} p\, dy \; - \int_{\partial\Omega_f \cap \partial\Omega_{f,out}} p\, dy \tag{4.7}$$

4.2.3 Deep Reinforcement Learning

RL is a sub-field of ML used for sequential decision making processes. In RL, an agent interacting with an environment, learns the optimal policy used for optimal decisions over time. Deep RL uses DNN as a predictor for high dimensional action space. Thermal shape optimization problem is a complex task, and tabular methods of Reinforcement learning are not effective in predicting the heat transfer and fluid properties. A Deep Neural Network representation of the physics of the CFD environment is required due to the stochastic nature of the design space [140]. Several algorithms have been widely used for interaction of Neural Network with RL agent such as Deep Q-Network (DQN) in which Q-value updates are a relation between the predicted and target values derived from the Bellman equation

[141]. Several methods also have been developed for policy gradient updates such as the vanilla policy gradient methods, Trust Region Policy Optimization (TRPO) and Advantage actor-critic (A2C) methods [142]. DQN works well on discrete action spaces; however, it is not a powerful tool for complex continuous problems. Vanilla policy gradient methods exhibit poor robustness; TRPO is complicated to implement particularly when dealing with complicated numerical simulations with the chance of failed meshing or equation solving. In this study, Proximal Policy Optimization (PPO) Algorithm is used with improved stability of the stochastic policy updates during training and parallel environment implementation. PPO use a clipping ratio to alternate between sampling data through interaction with the environment, and optimizing a surrogate objective function using stochastic gradient ascent [143]. In this study, we use three fully connected hidden layer with ReLU activation function written in Tensorflow. Hyperparameter values are given in A.2 to facilitate the reproducibility of the Results.

4.2.4 Policy Gradient Methods

Policy gradient methods use gradient estimator as the form of Eq. 4.8 in combination with gradient ascent 4.9.

$$\nabla_\theta J(\pi_\theta) = \underset{\tau\sim\pi_\theta}{\mathrm{E}} \sum_{t=0}^{T} \nabla_\theta \log \pi_\theta(a_t|s_t) A^{\pi_\theta}(s_t, a_t) \tag{4.8}$$

Where π_θ denote a policy with parameters θ, and $J(\pi_\theta)$ denote the expected finite-horizon undiscounted return of the policy. The gradient of $J(\pi_\theta)$, τ is a trajectory and A^{π_θ} is the advantage function for the current policy. $a_t \in \mathcal{A}$ and $s_t \in \mathcal{S}$ are action and state from action and state space $\mathcal{A}$ and $\mathcal{S}$ shown in Fig. 4.2.

Gradient ascent updates the policy parameters θ according to Eq. 4.9

$$\theta_{k+1} = \theta_k + \alpha \nabla_\theta J(\pi_{\theta_k}) \tag{4.9}$$

Where α is a learning rate and $k \in \{0, 1, 2, ...\}$ are the update numbers.

The primary challenge in policy gradient method is the high variance observed in Eq. 4.8. As it can bee seen in Eq. 4.9, high variance of the gradient can damage the learning process particularly in presence of potential occasional divergence in computation environment. There are two options of constraining learning rate (α) which makes the learning process slow or constraining the policy gradient. TRPO is introduced as a substitute to

line search for optimal point [144]. This method defines a trust region (δ) based on the new and old policy so that the policy update is constrained inside the trust region. The objective function in TRPO (L^{TRPO}) is defined according to Eq. 4.10 subjected to a constraint defined by KL-divergence (D_{KL}) between new and old policy via Eq. 4.11.

$$L^{TRPO} = \frac{\pi_\theta(a_t|s_t)}{\pi_{\theta_k}(a_t|s_t)} A^{\pi_{\theta_k}}(s_t, a_t) \tag{4.10}$$

$$\bar{D}_{KL}(\theta||\theta_k) = \underset{s\sim\pi_{\theta_k}}{\mathrm{E}} \left[D_{KL}\left(\pi_\theta(\cdot|s)||\pi_{\theta_k}(\cdot|s)\right)\right] \leq \delta \tag{4.11}$$

As it can bee seen, the KL-divergence impose additional computation burden on the optimization. The implementation of the TRPO is also complicated.

4.2.5 Proximal Policy Optimization

Several different algorithm exist for deep RL implementation among which PPO provides a robust and uncomplicated framework for parallel training. There are two primary policy updates methods using PPO known as PPO-Penalty and PPO-Clip. In the present study, we use PPO-Clip policy updates which remains stable in case of mesh failure since remeshing process are prone to failure. PPO-Clip updates policies via Eq. 4.12 [143].

$$\theta_{k+1} = \arg\max_\theta \underset{s,a\sim\pi_{\theta_k}}{\mathrm{E}} \left[L(s_t, a_t, \theta_k, \theta)\right] \tag{4.12}$$

Where L is according to the Eq. 4.13

$$L(s_t, a_t, \theta_k, \theta) = \min\left(\frac{\pi_\theta(a_t|s_t)}{\pi_{\theta_k}(a_t|s_t)} A^{\pi_{\theta_k}}(s_t, a_t),\ \ \mathrm{clip}\left(\frac{\pi_\theta(a_t|s_t)}{\pi_{\theta_k}(a_t|s_t)}, 1-\epsilon, 1+\epsilon\right) A^{\pi_{\theta_k}}(s_t, a_t)\right) \tag{4.13}$$

Where ϵ is a hyperparameter controlling the correlation between new and old policy considered to be 0.2 in this study, and advantage $A^{\pi_{\theta_k}}(s_t, a_t)$ is according to Eq. 4.14

$$A^{\pi_{\theta_k}}(s_t, a_t) = \delta_t + (\gamma\lambda)\delta_{t+1} + \cdots + \cdots + (\gamma\lambda)^{T-t+1}\delta_{T-1} \tag{4.14}$$

Where t is the timestep and T is the final time.

$$\delta_t = r_t + \gamma V(s_{t+1}) - V(s_t) \tag{4.15}$$

Where $V(s_t)$ is the estimated value function and r_t is the reward.

An ideal fin is expected to cause maximum heat transfer and minimum pressure. The agent is supposed to find an optimal policy that can maximize the discounted cumulative reward. In this chapter, reward of the agent is calculated according to Eq. 4.16. We also provide the results based on the reward using Webb and Eckert's method according to Eq. 4.17 [145].

$$r_t = \frac{Q}{Dp} \tag{4.16}$$

$$r_{t_{Webb}} = \frac{Q}{Dp^{1/3}} \tag{4.17}$$

The reward is computed numerically with FEM in CFD environment written in FEniCS. Reward shaping is a technique used to construct the reward function that can provide a better convergence for our learning process [146]. In CFD, particularly, the interaction between the agent and the environment is expensive due to the fact that solving the Navier-Stocks, convection-diffusion equations, and other governing equations require extensive processing power and memory. Advancement in technology, Graphic Processing Units(GPUs), and cloud computing has facilitated the computer simulation. However, CFD simulations are still expensive and mostly rely on CPU and memory to save cell information rather than GPU. Therefore, receiving proper reward based on the understanding of the environment can speed up the learning [147]. The value of the reward can be multiplied by a constant number based on the physics of the design domain. In this study, the reward was multiplied by a small number in order to achieve convergence since the pressure drop value was small compared to heat transfer.

The action taken by the agent is changing the position of the control point represented in Eq. 4.1. The PPO assumes a large trajectory is obtained from the CFD environment through sub-iterations. One epoch is one forward pass and one backward pass of all training data and the PPO does several epochs over training batch during training. The level steps of the execution can be found in algorithm 1.

DNN design in this study includes one input layer and three consecutive hidden layers of size 256 each, and one output layer. The classic rectified linear unit (ReLU) function is used as an activation function applied to hidden layers. The reward function, presented in the Eq. 4.16 and Eq. 4.17 guides the network toward lower cost and higher performance in design.

Algorithm 1

Input: Initial control points, initial policy parameters θ_0,
For K=0,1,..., episode
Solve Eq. 4.3 and Eq.4.5 using weak form of the equations (given in appendix) by running policy $\pi_k = \pi(\theta_k)$
Collect a set of trajectories $\mathcal{D}_k = \tau_i$
Compute reward using Eq. 4.16 or Eq. 4.17
Update the policy by maximizing the PPO-Clip Objective with Adam optimizer:

$$\theta_{k+1} = argmax_\theta \frac{1}{|\mathcal{D}_k|\mathsf{T}} \sum_{\tau \in \mathcal{D}_k} \sum_{t=0}^{\mathsf{T}} L(s_t, a_t, \theta_k, \theta)$$

Update the control points based on the new policy
End for

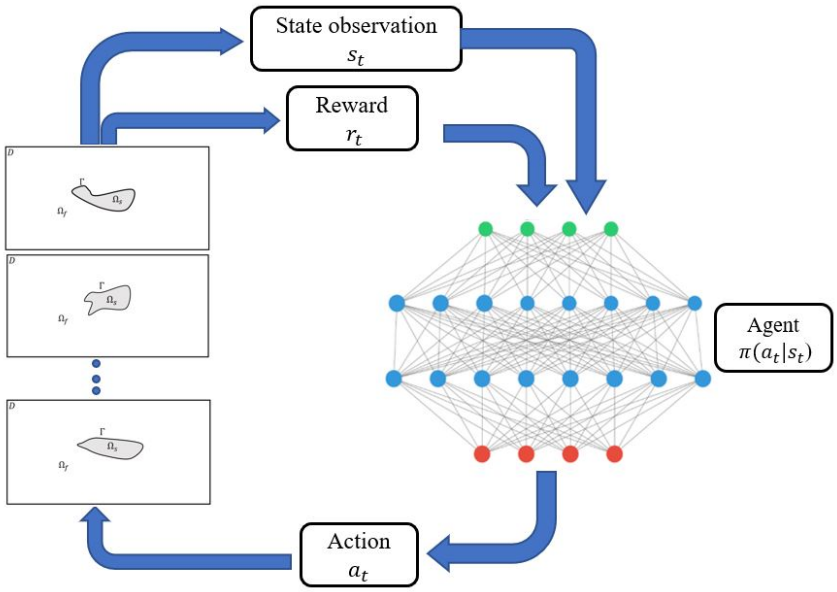

Figure 4.2: Deep RL workflow with parallel CFD environments

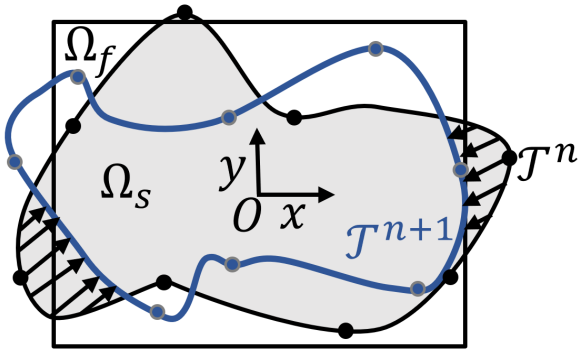

Figure 4.3: Geometric control applied to the design domain

4.2.6 Parallel Computing

Parallel environments run the FEM numerical solution in different CPU cores. Fig. 4.2 shows the workflow configuration. The same random seed is used for all parallel environments so that shape deformations would stay close. In other words, a single agent learns new policy from a batch of data acquired from parallel CFD computation (i.e. heat transfer and pressure drop). Batch size of 50 sample process is used in this workflow.

4.3 Results and Discussion

The results show that starting from a reference rectangle fin shape which is frequently used in HVAC devices, the agent is able to increase heat transfer and reduce pressure drop through a proper trajectory. Shape evolution over 500 episodes of training is shown in Fig. 4.4. At the beginning of the training, the agent explores wider range of the design space beyond the domain specified in Fig. 4.1 with the expectation of receiving reward by increasing heat transfer area; however, proper learning is obtained by the agent since reward penalization is considered based on the distance of the control points from the specified design space according to Fig. 4.3. The reward is reduced by the percentage of the distance from the desired action space, e.g. $(|y| - \frac{H}{8})/\frac{H}{8} \times r_t$ in y direction. The same penalization method is applied for x direction. It can be inferred from the shape evolution over the training episodes that the agent is on the pass to increase the heat transfer surface while reducing the frontal area that causes pressure drop.

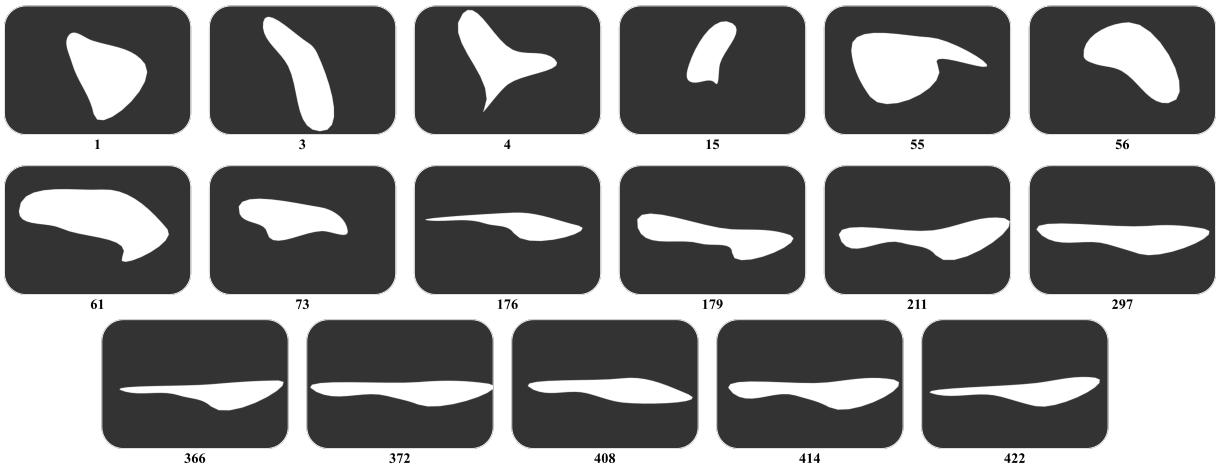

Figure 4.4: Shape evolution for the case starting from rectangle for 15 DOF at Re = 100, Pr = 0.05

To consider the effect of starting shape on the optimized geometry, we studied a circular shape as the starting point. Shape evolution for the case with circle as the initial geometry is shown in Fig. 4.5. Immediately after initial point, the agent tries some random shapes; Fig. 4.5 shows that the agent's understanding of the environment is not limited to the initial shape. Optimized shapes from Fig. 4.4 and Fig. 4.5 are similar in terms of performance and geometry.

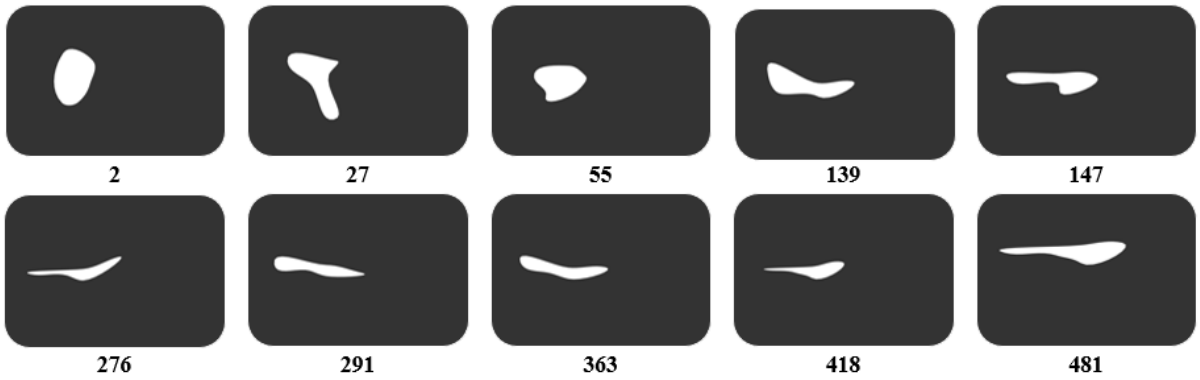

Figure 4.5: Shape evolution for the case starting from circle for 15 DOF at Re = 100, Pr = 0.05

An interesting observation is that similar to Mekki et al. [22], the optimized geometries are asymmetric; this might be due to agent's understanding to expose the surface to the stream with higher temperature gradient while not to impose pressure drop on both sides of the shape. Mekki et al. [22] reported 45 % improvement in performance mostly due to increase in heat transfer while pressure drop increased in their case. Our framework reduces the pressure drop by 60 percent while increasing the heat transfer rate by more than 30 percent.

Reference design and an arbitrary shape design are shown in Figs. 4.6 and 4.7, respectively. Body-fitted mesh generation used in the iterative training process is seen in Fig. 4.7. It can be seen that how mesh around the corners and boundaries are adapted to provide a robust numerical approach. Since the number of mesh is changing in each episode through adapted body-fitted mesh, mesh-independency could not be performed using number of meshes. Instead, we use a clipping method between number of meshes and mesh size on the curve constructed between points. This clipping method limits the mesh size to remain smaller than $L/200$, and number of meshes between points to remain higher than 15 cells. This method results in number of unstructured grid between 10000 to 18000 based on the number of control points chosen for optimization and constructed geometry in each iteration. Fig. 4.8 shows the dimensionless temperature, $T^{+}(\frac{T_s - T}{T_s - T_{in}})$, at the outflow using different number of meshes for the reference shape with five control points. This figure shows that with minimum number of 15 meshes between control points, consistent results can be obtained.

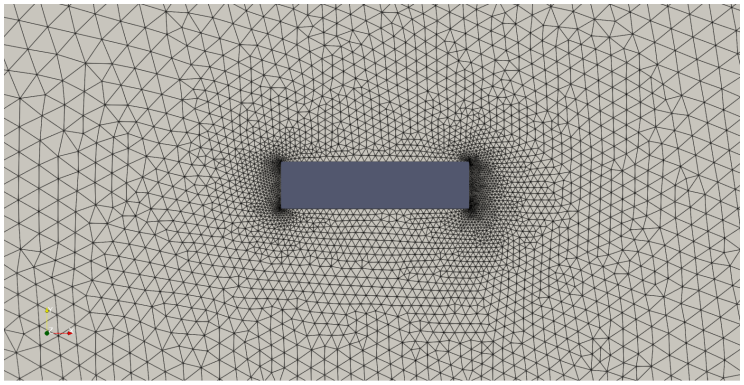

Figure 4.6: Meshed domain showing the reference geometry

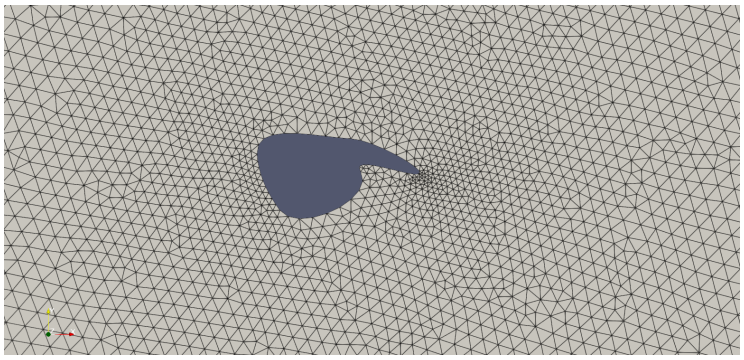

Figure 4.7: Body-fitted mesh variation during the learning process

Fig. 4.9 shows rewards for each single iteration along with the moving averaged value of 20 neighboring data points for the case of the shape with 15 Degree Of Freedom at Reynolds number equal to 100 and Prandtl number equal to 0.05.

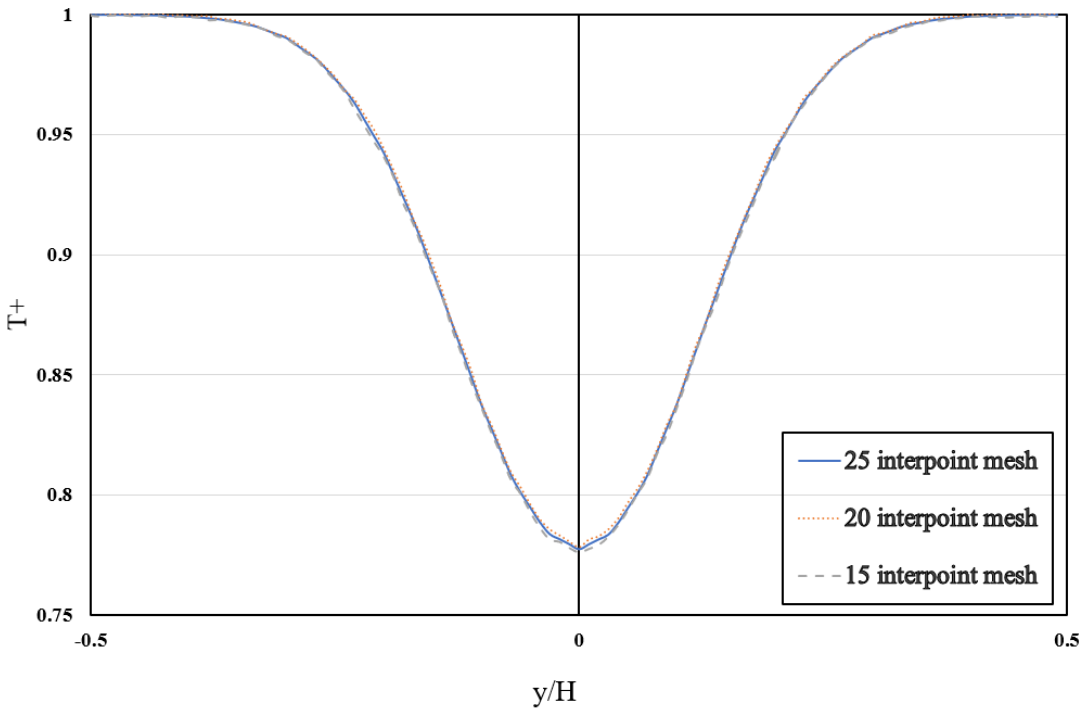

Figure 4.8: Averaged dimensionless temperature profile at the outlet at Re = 100, Pr = 0.05

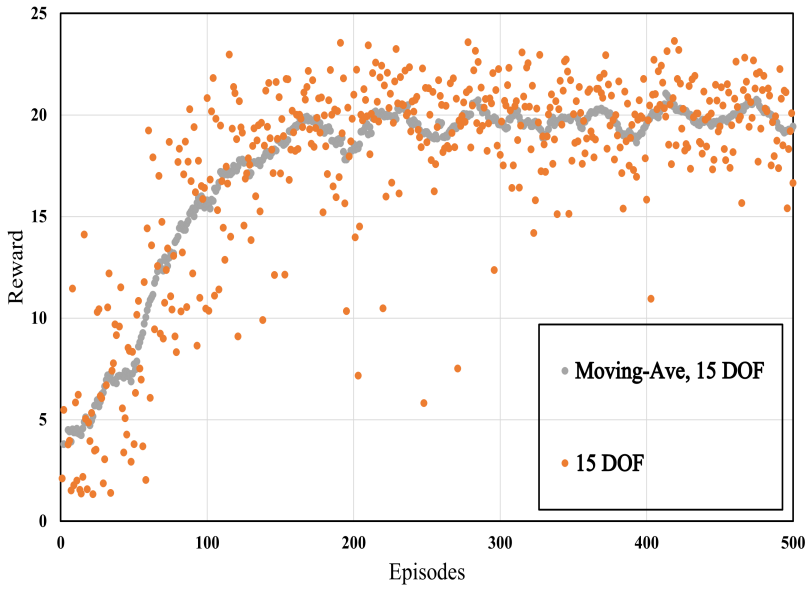

Figure 4.9: Learning curve (instant and moving average) for shape with 15 DOF at Re = 100, Pr = 0.05

Fig. 4.10 shows the moving average reward for different DOF. It can bee seen that providing the setting with higher DOF, increases the reward of the RL algorithm since the agent is able to explore more variation in shape and receive more rewards. Higher reward is equivalent to reduced cost of the pumping power and improved performance which is desired for many HVAC devices. However, higher DOF is accompanied by higher computational cost particularly when extended to 3D space.

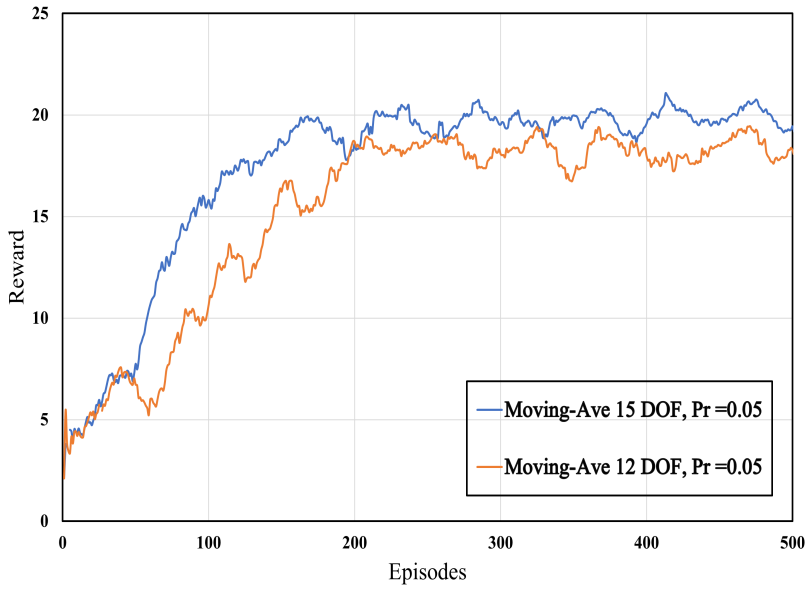

Figure 4.10: Learning curve comparison for shapes with 12, and 15 DOF at Re = 100, Pr = 0.05

Fig. 4.11 shows the learning curve at RE = 100 and Pr = 0.7. It can be seen in Fig. 4.11 that the reward value is pertinent to the fluid flow properties like Pr and RE number since the reward values are different from Fig. 4.9. According to Eq. 4.16, the value of the reward is computed by heat transfer and pressure drop that can change by Prandtl number. Topologies reach a performance plateau based on the degree of freedom given to the shapes. It can bee seen that in case of 12 DOF, 200 episodes of training is required for the moving-averaged solution to reach the plateau while for 15 DOF it takes close to 300 episodes of training.

Fig. 4.12 shows the dimensionless heat transfer and pressure drop with respect to the reference geometry for shapes over 500 episodes in two different parallel CFD environment explained in parallel computing section. This results is related to the shapes with 15 DOF at RE = 100 and Pr = 0.05. As the same random seed is used in the different environments, shapes and performances stay close. One of the optimized shapes with higher reward value, an airfoil-like shape, and reference shape are shown in the Fig.4.12. It can bee seen that the airfoil-like shape which is a common shape in HVAC heat exchangers is among the well-performing shapes; however, the best performing shapes in Fig. 4.12 have 35 % less pressure drop compared to airfoil-like shape as well as higher heat transfer rate. Fig.

4.13 also shows temperature distribution for one of the best performing designs and the reference geometry.

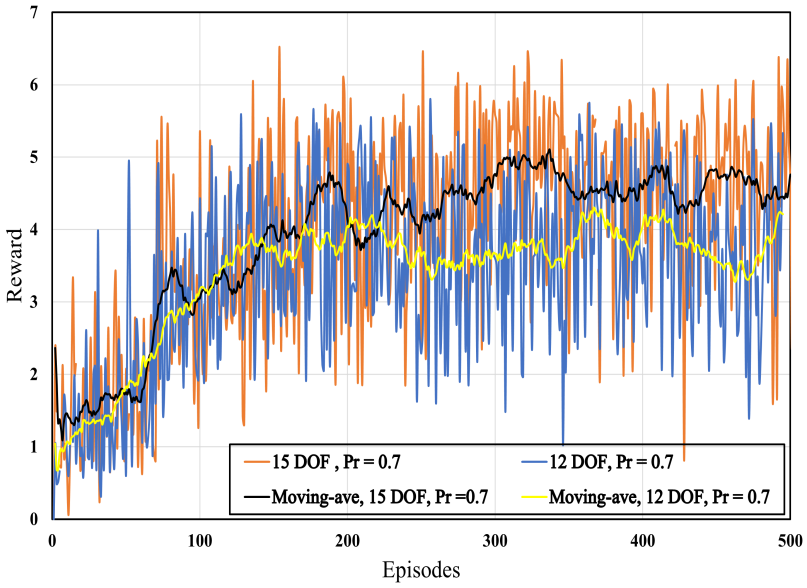

Figure 4.11: Learning curve comparison for shapes with 12, and 15 DOF at Re = 100, Pr = 0.7

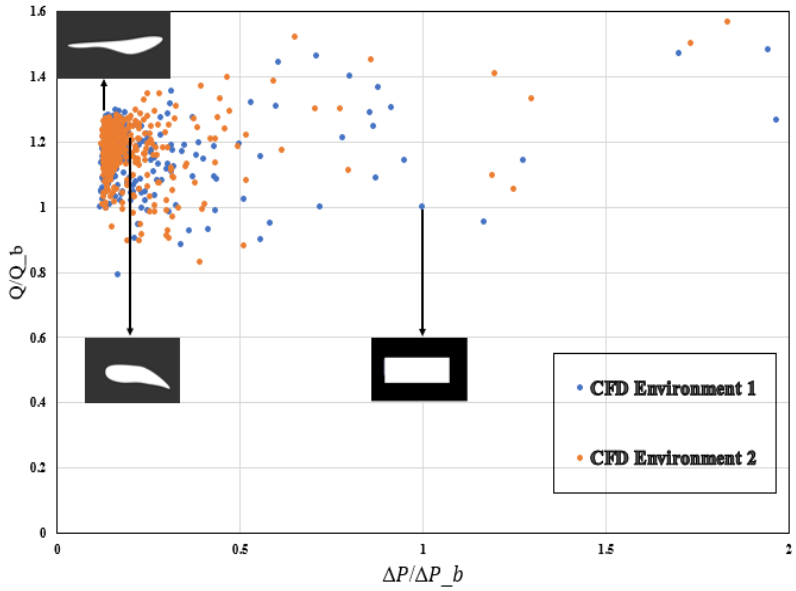

Figure 4.12: Dimensionless heat transfer and pressure drop with respect to the reference geometry for 15 DOF at RE = 100 and Pr = 0.05

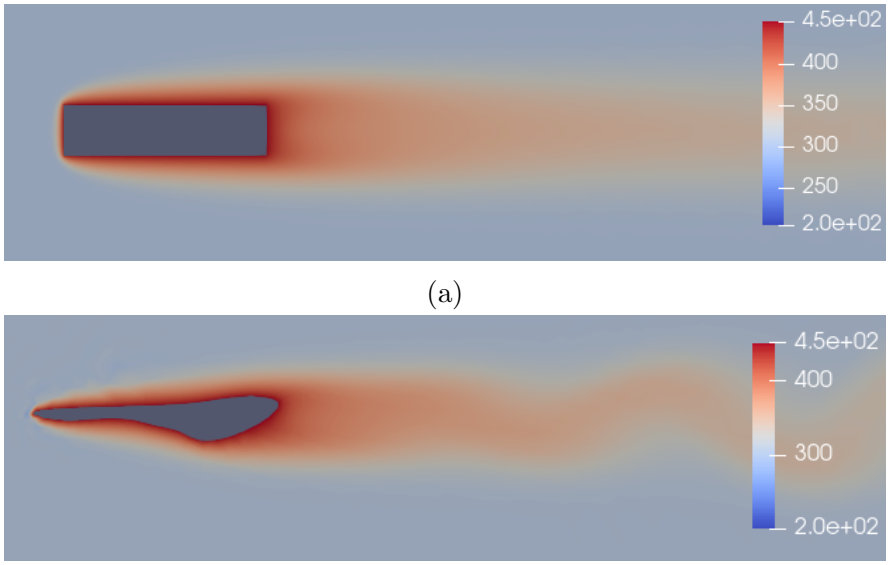

Figure 4.13: Temperature distribution for (a): The reference geometry, (b): One of the best performing shapes

Fig. 4.14 illustrates the reward history along with the pressure drop and heat transfer for RE = 100 and Pr = 0.05. It can be inferred that the agent receives higher reward by decreasing the pressure drop compared to increasing the heat transfer according to the reward definition. This, however, could change based on the application. We provide the results using the reward function based on Eq. 4.17 [145]. Fig. 4.15 shows the reward history during the shape optimization using Webb and Eckert reward definition. Definition of the reward function using Webb and Eckert's method results in larger shapes with higher pressure drop. The rational exponent for pressure drop in the reward function reduces the effect of pressure drop on the shape optimization. Some of the well-performing shapes along with one of the initial shapes are shown in Fig. 4.15.

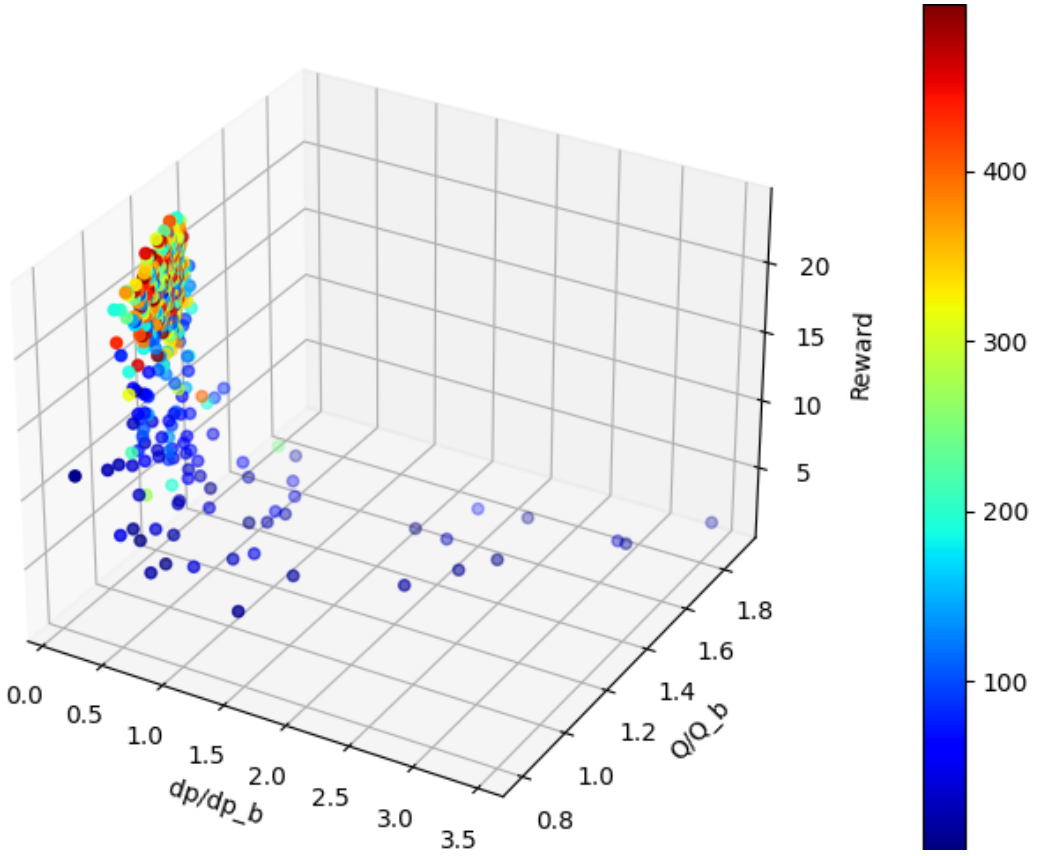

Figure 4.14: Reward history as a function of pressure drop and heat transfer (colorbar shows the episode number)

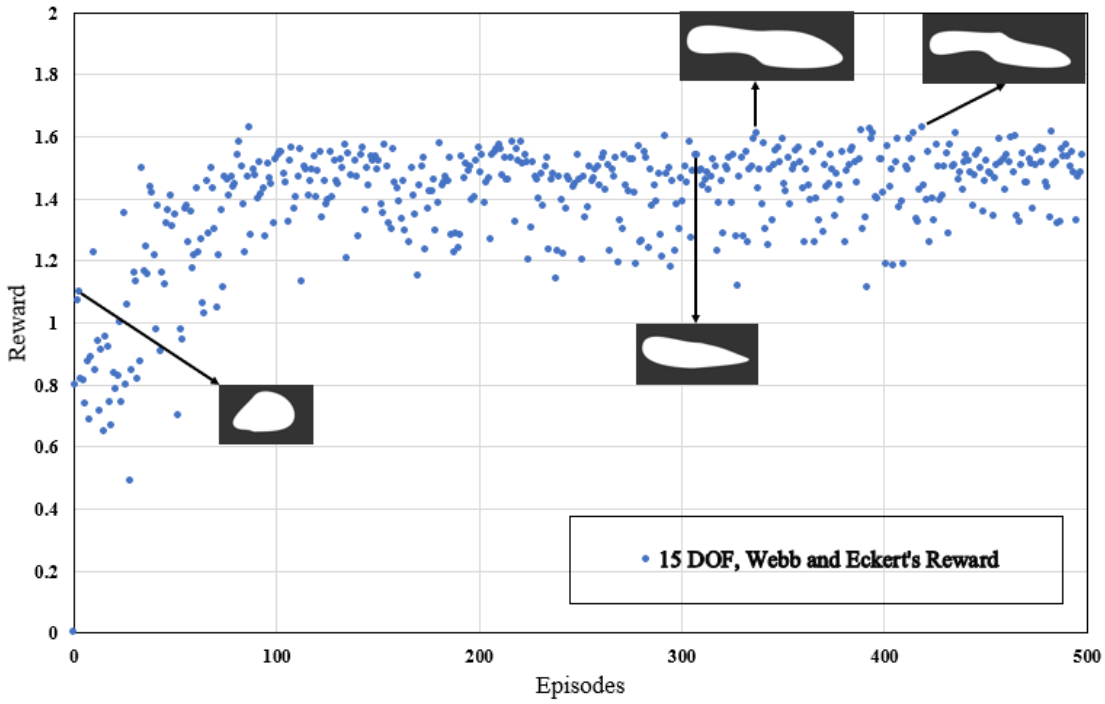

Figure 4.15: Learning curve according to the reward from Webb and Eckert (Eq. 4.17) for shapes with 15 DOF at Re = 100, Pr = 0.05

4.4 Conclusion

In this chapter, a deep reinforcement learning approach for thermal shape optimization using BREP was introduced. A parametric geometry represented by composite Bézier curve was used for design space exploration to reduce the dimensionality of the thermofluid shape optimization problem. Parallel computing architecture was implemented for CFD solver to provide data for the learning. An interacting framework which consists of parallel heat transfer simulation and deep RL was presented. Starting from a rectangle reference geometry, the reinforcement learning agent is able to reduce the pressure drop by 60 percent while increasing the heat transfer by more than 30 percent without any enforcement. The rectangle geometry was presented as a reference while the framework can work without any initial geometry. The robustness of the presented algorithm was demonstrated in different Reynolds and Prandtl numbers. The proposed framework keeps a neat boundary using BREP throughout the optimization. Maintaining a clear boundary provides higher

flexibility in terms of implementing boundary conditions and using different working fluid. Increasing the degree of freedom in the presented deep RL workflow results in higher computational cost which makes 3D exploration expensive. However, with the rapid progress in deep learning, methods such as geometric deep learning could speed up the optimization process empowering function approximator in deep RL algorithm.

Chapter 5

Convolutional Neural Network for CFD Results Prediction of BREP Topologies

In this chapter, surrogate models are presented for heat transfer and pressure drop prediction of complex geometries generated using composite Bézier curve. It can be inferred from chapter 4 that the limiting factor in thermal design space exploration is CFD computation. In this chapter, Convolutional Neural Networks (CNNs) are used to predict the CFD results directly from topologies saved as images. These predictive models can be directly applied to design space exploration algorithms as a substitute to the CFD solver. This chapter is based on some parts of the article which is submitted to " "International Journal of Heat and Mass Transfer" entitled" Convolutional surrogate and degrees of freedom in thermal design".

5.1 Introduction

Previous studies were performed on prediction of velocity, pressure, and drag coefficient for constant geometries. In some cases, few geometrical parameters such as aspect ratio were considered. Details on recent studies are discussed in chapter 2, section 2.5.2. In this chapter, modern optimized CNN architectures are used for direct heat transfer and pressure drop estimation of morphable shapes in contrast to previous studies performed on constant geometries. This study focuses on heat transfer and pressure drop prediction

directly from images without the need for mesh representation. Xception model along with a network optimized CNN are used in this study. By applying these models, the time required for domain heat transfer and pressure drop computation for varied morphable topologies can be reduced to few seconds.

5.2 Methodology

The focus of this chapter is to develop a predictor for the design space used in chapter 4. Here, a summarized information about the domain is provided. The problem remains a conjugate heat transfer with laminar incompressible fluid in a constraint heat exchanger. The design space is a two dimensional space $D = \overline{\Omega_f} \cup \overline{\Omega_s} \subset \mathbb{R}^2$ occupied by a solid, and an incompressible fluid.

5.3 High Fidelity Simulation

A CFD solver is created for the physics shown in Fig. 5.1. Incompressible Navier-Stokes equation, and convection-diffusion equation are solved using FEniCS. For further details, please refer to chapter 4, section 4.2.2. Parallel computing using 16 cores and 32 threads is used for high fidelity simulation in FEniCS.

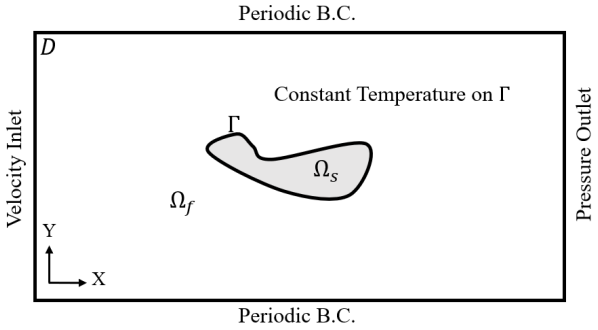

Figure 5.1: CFD domain for data generation

5.4 CNN models

Several CNN architectures have been proposed in the past few years [148, 149]. These architectures range from regular CNNs stacked together to develop very deep layers all the way to more complex engineered architecture after google presented inception network [150]. Most of them are competitive in benchmark image classification problems [151]. Their performances in real world predictive tasks are, however, apart from the benchmark datasets [152, 153]. Xception network along with a custom network optimized model are deployed in this study. Xception architecture consists of a modified version of depthwise separable convolution introduced in Inception model to work in a series of operation to improve utilization of computing power [154]. For further details please refer to the original reference [148].

5.4.1 Dataset Generation

Geometries are generated using mathematical method explained in chapter 4, section 4.2.1, which provide 2D space for Eulerian simulation. Mesh generation is based on adaptive method and heuristics. The fluid properties are controlled by Reynolds and Prandtl number which considered to be 100 and 0.7, respectively. Since flow is time-dependent, time-averaged numerical result is considered for a long period of time over the third part of the computation. Temperature profile for some of the shapes at one of the final time instances are shown in Fig. 5.2. 4000 shapes using 4 and 5 control points are generated and saved as images. The size and resolution of the images are considered to be constant with a single channel, and 506×506 pixels. CFD results are saved and labeled accordingly. 70% of the data are used for training and the remainder for cross-validation and test purpose.

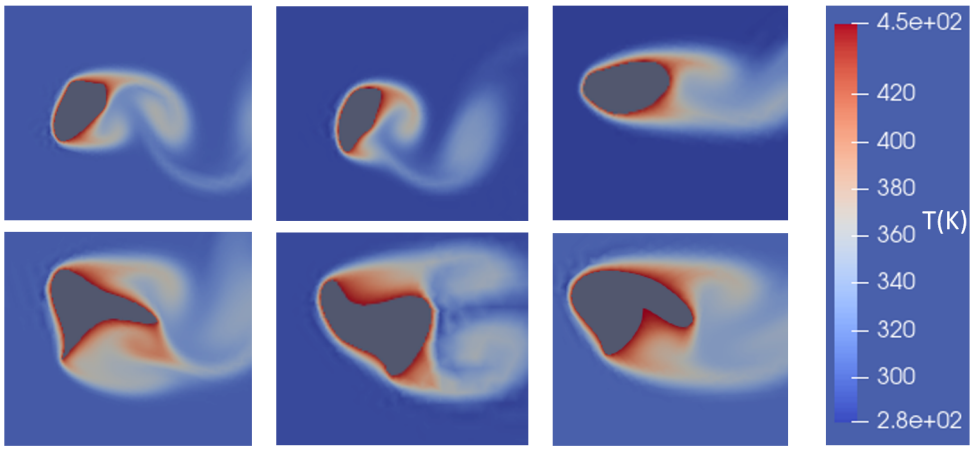

Figure 5.2: Temperature profile of some random shapes in the dataset

5.4.2 Experimental Setup

All experiments were conducted on a single AMD Ryzen workstation. The workstation was equipped with Ubuntu 20.04 LTS, 16-Core Processor 3.40 GHz CPU, 32.0 GB RAM, and one NVIDIA GeForce RTX 3080 Graphics Processing Unit (GPU). Python 3.8.9, CUDA 10.1, TensorFlow, and Keras are used for deep learning implementation.

5.5 Results and Discussion

5.5.1 Hyperparameter Optimization

Hyperparameter tuning in DL models is often performed using either grid search or random search [155]. In this study, random search is used for number of feature extraction layers ($3 <$ feature extraction layers < 10), number of filters in each layer ($8 <$ number of filters < 96), and number of FC layers ($2 <$ FC layers < 5) . After few experiments with kernel size for the convolution operators, it is found that changes in accuracy and convergence between 3×3 and 5×5 kernel size are negligible since the location of information is in the center of the image. For efficient use of computational resources, 3×3 kernel size for convolutional layers and 2×2 kernel size for maxpooling layers are used. The schematics of the CNN architecture used for direct heat transfer prediction is shown in Fig 5.3. It contains of six successive feature extraction layers with two convolutional layers

and one max pooling layer in each of them. Some of the hyperparameters of the model are shown in Appendix A.3 . Total number of trainable parameters for the proposed model is 1,160,305. Architecture of the optimized network is shown in AppendixA.4. Xception model consists of more than 17 million parameters. Hyperparameter values for Xception model are considered to be the same as those explained in the original article with the exception of those shown in Appendix A.5 [148]. Batch size for Xception is considered to be 256 while batch size of 128 leads to the best performance in regular CNN. Training time for heat transfer prediction using regular CNN and Xception network on our experimental setup are 45 minutes and 135 minutes, respectively. The same method and architecture is used for pressure drop considering the output neuron as pressure drop value. Training for pressure drop estimation takes almost one hour for regular CNN and an average of 170 minutes for Xception model.

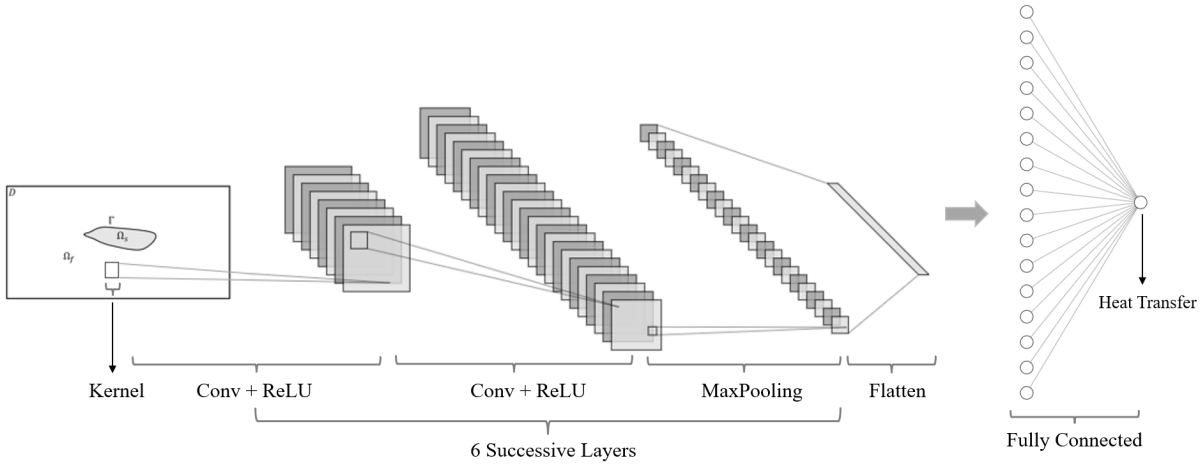

Figure 5.3: CNN architecture for heat transfer prediction

5.5.2 Error Behavior

Root Mean Squared Error (RMSE), Mean Square Error (MSE), and Mean Absolute Error (MAE) are used frequently in the literature for loss function definition to evaluate the quality of a machine learning model during training [122]. In this study, MSE is used as given in Eq. 5.1 to train the models [122]. In this equation, $\hat{y}_i$ is the predicted value, and y_i is the ground truth value from high fidelity simulation. N is the number of data points in the batch sample.

$$MSE(\mathbf{y}_i, \hat{\mathbf{y}}_i) = \frac{\Sigma_{i=1}^{N}(y_i - \hat{y}_i)^2}{N} \tag{5.1}$$

MSE values for each epoch of training and validation of optimized CNN model and Xception model are shown in Fig. 5.4, and Fig. 5.5, respectively. As it can be seen in these figures, Xception model has lower final MSE value.

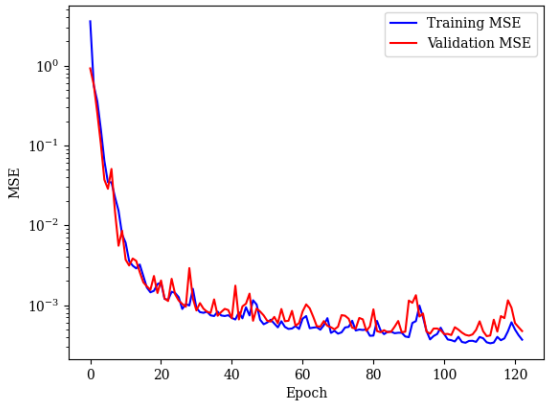

Figure 5.4: MSE value as a function of epoch during the training of optimized CNN architecture for heat transfer prediction

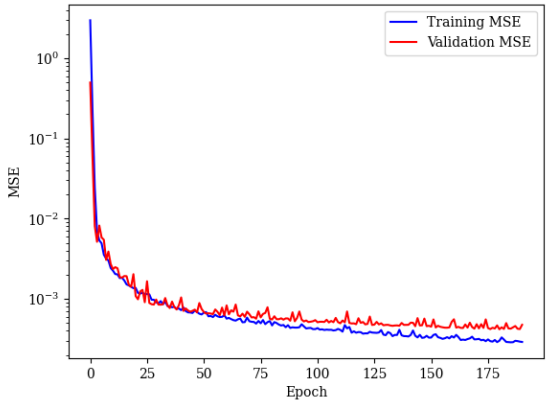

Figure 5.5: MSE value as a function of epoch during the training of Xception model for heat transfer prediction

5.6 Prediction Performance

Here, the performance of surrogate models are analyzed using R^2 value also known as coefficient of determination which is computed by Eq. 5.2.

$$R^2 = 1 - \frac{\Sigma_i (y_i - \hat{y}_i)^2}{\Sigma_i (y_i - \overline{y})^2} \tag{5.2}$$

where $\overline{y}$ is the baseline prediction which is considered to be the mean of actual values.

MAE is also used to evaluate the model accuracy according to Eq. 5.3

$$MAE(\mathbf{y}_i, \hat{\mathbf{y}}_i) = \frac{\Sigma_{i=1}^{N} (y_i - \hat{y}_i)}{N} \tag{5.3}$$

In order to better visualize the estimated values, confidence interval and residual plots are also used. Fig. 5.6 and Fig. 5.7 show the predicted and ground truth values for heat transfer using optimized CNN model, and Xception model, respectively. On each plot, 150 data points of the same shapes in the test dataset are used to avoid clutter. 99 percent confidence intervals are also plotted in Fig. 5.6 and Fig. 5.7 which are barely visible. This shows high accuracy in prediction. The trained model generalizes well beyond the training dataset as can be seen from the predicted values from the test dataset.

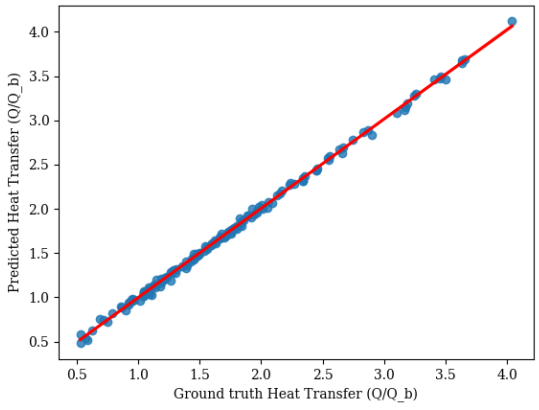

Figure 5.6: Predicted and ground truth heat transfer using optimized CNN model

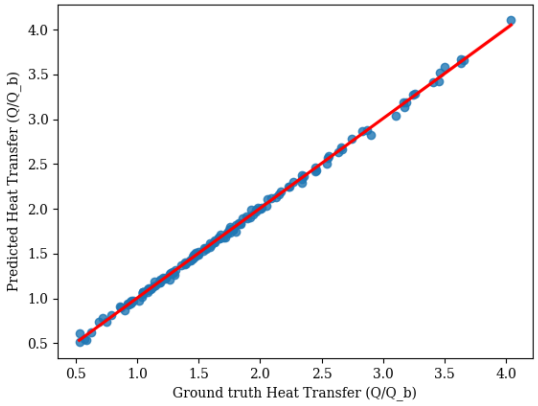

Figure 5.7: Predicted and ground truth heat transfer using Xception network

Fig. 5.8 and Fig. 5.9 show the residual plot for heat transfer estimation models. Residual is defined as a difference between the predicted and actual values in the test dataset. Distribution of the residuals and data are also shown on the right hand side and top of the plot, respectively. One important observation from residual plot is that shapes with smaller heat transfer have higher deviation from the actual values. Higher prediction errors are associated with smaller heat transfer values which are pertinent to smaller shapes. This might be addressed by choosing the norm based on the shape area and normalizing the input data based on the shape area computed using Green's theorem [156]. However, area normalization was not performed since the accuracy of the models are within a great range. This normalization can be applied for higher complexity physics problems.

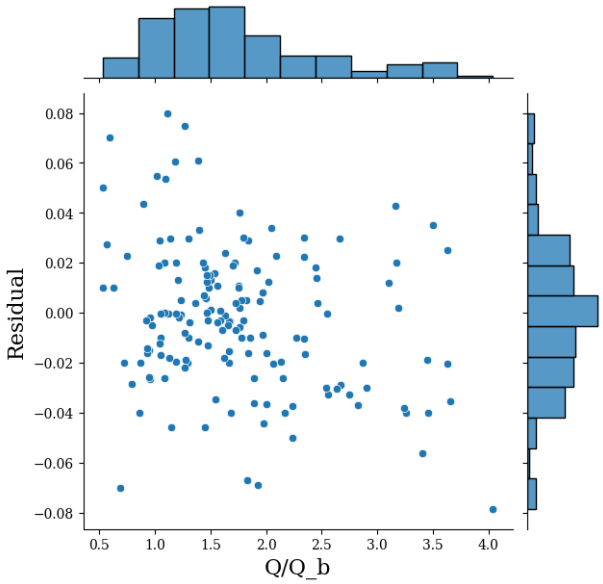

Figure 5.8: Residual plot for heat transfer estimation using optimized CNN model

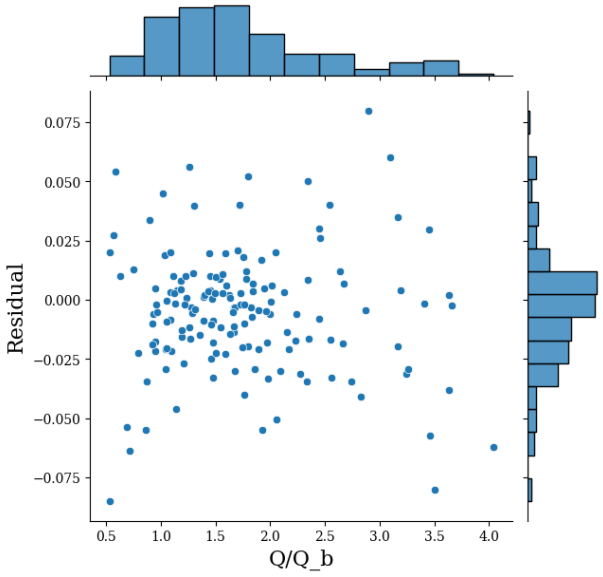

Figure 5.9: Residual plot for heat transfer estimation using Xception network

Table 5.1 shows the statistical summary for both heat transfer estimation models. As

it can be seen from the table, both models provide high accuracy prediction with Xception network having slightly higher performance. The coefficient of determination value is close to one and very hard to achieve in regression models. The order of the errors are small particularly for concept design optimization where exact values are not crucial for the design process.

Table 5.1: Statistical results summary of the heat transfer surrogate models for a single morphable shape

Model	R^2	MAE
CNN	0.997	0.022
Xception	0.998	0.019

Fig 5.10 shows the predicted and ground truth values for pressure drop estimation using optimized CNN for 200 data points. Fig. 5.11 shows the estimated values for Xception network. It can be seen that predicted heat transfer values are closer to the identity line compared to pressure drop values for both models. This is because of the data distribution of the pressure values. Even though the same shapes are used for training the models, CFD results distribution for heat transfer values are more compact than pressure drop values. The fact that heat transfer and pressure drop can be predicted directly from the BREP saved as images with a small dataset provides more attention to the machine learning-accelerated solutions for thermo-fluid structures with nonlinearity [157].

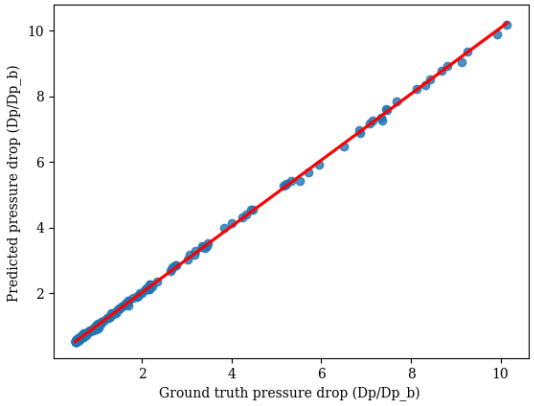

Figure 5.10: Predicted and ground truth pressure drop using optimized CNN model (99 percent confidence interval is also plotted)

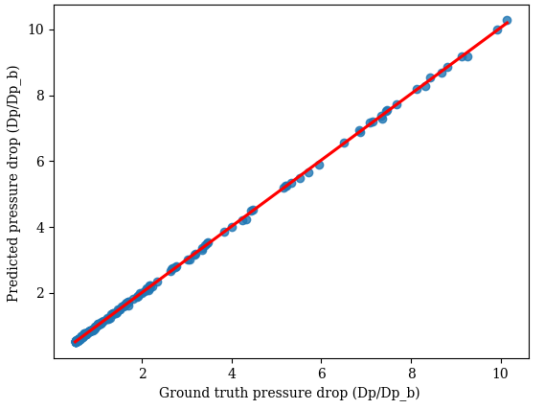

Figure 5.11: Predicted and ground truth pressure drop using Xception network (99 percent confidence interval is also plotted)

Fig. 5.12 and Fig. 5.13 show the residual for pressure drop using CNN and Xception network, respectively. Residual plot for optimized regular CNN shows very small bias in predicting pressure drop. The histogram is far from being right-skewed, but the peak distribution is not exactly at zero line. Small overestimation can be observed in the prediction which can be accumulated over the test set and cause larger MAE. Table 5.2 shows the statistical summary for the pressure drop prediction. As it was mentioned, CNN model has a larger MAE. From the residual plot and MAE, it can be inferred that Xception works better for both pressure drop and heat transfer prediction.

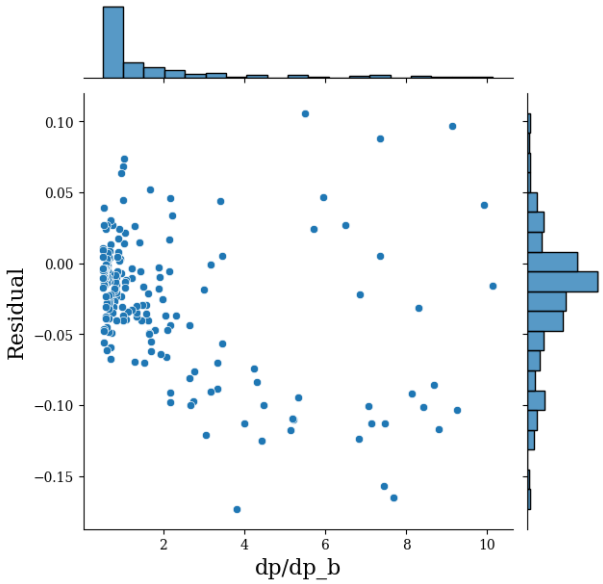

Figure 5.12: Residual plot for pressure drop estimation using optimized CNN model

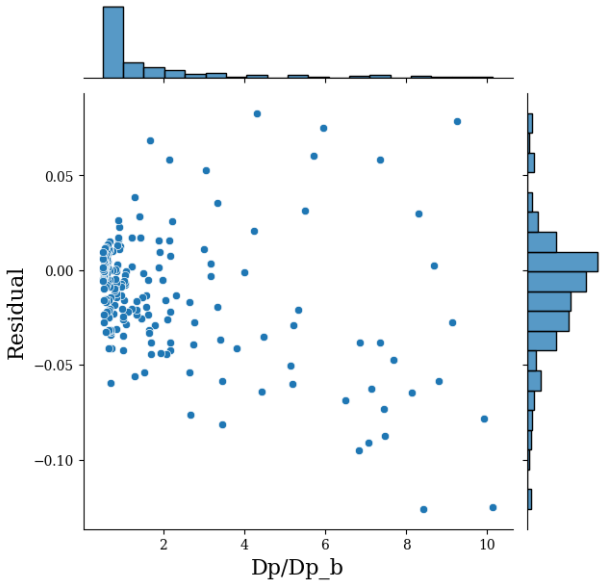

Figure 5.13: Residual plot for pressure drop estimation using Xception network

Table 5.2: Statistical results summary of the pressure drop surrogate models for a single morphable shape

Model	R^2	MAE
CNN	0.999	0.0378
Xception	0.999	0.023

Table 5.3 shows the average time required for the CNN models and CFD solver. Regular CNN provides faster computation compared to other methods. CFD solver occasionally fails because of the failure in mesh adaptation during the shape morphing in presence of sharp edges or acute angles. DL-based computation does not require mesh generation and provides more robust algorithm. High fidelity simulation has higher standard deviation in terms of computing time since variation of the shape causes change in number of meshes which leads to change in computation time.

Table 5.3: Computation time for different computing methods

Model	**Average prediction time**
CNN	0.42 seconds
Xception	2.03 seconds
High fidelity simulation	45 minutes

5.7 Conclusion

In this chapter, modern convolutional neural networks were utilized to predict heat transfer and pressure drop of single shapes generated using composite Bézier curve without expensive CFD computation. An optimized CNN network using regular convolutions as well as an Xception model were deployed to predict heat transfer and pressure drop values. Xception network showed more accurate prediction compared to regular CNN. Time-averaged CFD results were predicted directly from images of the geometries without using mesh representation.

Chapter 6

Generative Thermal Design Through Multi-Agent Cooperative Environment

In this chapter, the design space of the thermal design is expanded to multiple shape optimization through multi-agent reinforcement learning. A generative thermal design solution is presented using cooperative multi-agent environment. First, surrogate models based on Xception network are trained to predict the CFD results of multiple fins inside the design space, similar to what was performed in chapter 5. The accuracy of the surrogate models are reported and are compared to the case with single fin shape. The pre-trained surrogate models are converted to an environment for the MARL framework. The learning is performed in a centralized way while actions are made in a decentralized way to tackle the instability of the problem. Part of this chapter is based on a paper that is accepted at Thirty-ninth International Conference on Machine Learning for Computational Design entitled " Generative Thermal Design Through Broundary Representation and Multi-Agent Cooperative Environment".

6.1 Introduction

In previous chapters, we showed the need for design automation and demonstrated how thermal problems are different from mechanical designs. GANs generate new designs from an existing dataset utilizing a generator and a discriminator which are usually Deep Neural

Networks (DNNs). The objective function of GANs should be differentiable to utilize gradient-based optimization while RL works as a semi-supervised ML algorithm and the reward of a deep RL can be defined based on the design requirements [158]. However, RL needs experience from the search domain. This was the main motivation of the previous chapter in which the possibility of using a surrogate model was assessed.

In this work, we utilize a surrogate model based on modern Convolutional Neural Network (CNN) to estimate the CFD results directly from geometries which is then used as a computational engine for the RL environment. This was previously used for other optimization algorithms in aerodynamics problems. Baque et al. [159] used CNNs as a surrogate model for CFD of aerodynamic shapes in conjunction with gradient-based optimization in which the objective function should be differentiable with respect to the shape parameters. Mark C. Messner assessed the accuracy of a CNN surrogate model for predicting mechanical properties which was then used for topology optimization [160].

Several high dimensional action space problem were solved using deep RL in multi-agent framework with a huge computational resources [161]. In MARL framework, convergence is more critical than the single-agent RL. Most of the multi-agent RL problems are solved using off-policy RL such as Q-learning since On-policy RL was known to be less sample efficient [162]. However, new research show effectiveness of on-policy MARL [163]. The information transferred during training and execution between the agents, policy and value function is crucial to convergence [164]. MARL can be performed either in a centralized or decentralized way. Decentralized learning method optimizes the agents independently and agents do not have access to the reward or policy of the collaborators or competitors. This causes instability in learning since the environment changes as a consequence of the actions of other agents. Centralized learning is simply an extension of single-agent RL and a single policy is learned for a collection of actions and states with one reward value.

Each of these methods show instability in complex tasks. Recent studies used Centralized Training and Decentralized Execution (CTDE) to bridge the chasm in complex continuous tasks [163, 165]. In this chapter, we use the same method to address the non-convergence in action space.

6.2 Methodology

The design space is a two dimensional space $D = \overline{\Omega_f} \cup \overline{\Omega_s} \subset \mathbb{R}^2$ occupied by solids and an incompressible fluid for Eulerian simulation similar to those in chapter 4 and chapter 5. The solid components Ω_s, however, consist of multiple composite Bézier curves constructing

multiple fin geometries in the fluid domain Ω_f. The BREP design space is shown in Fig. 6.1 in conjunction with the discrete space used in conventional TO.

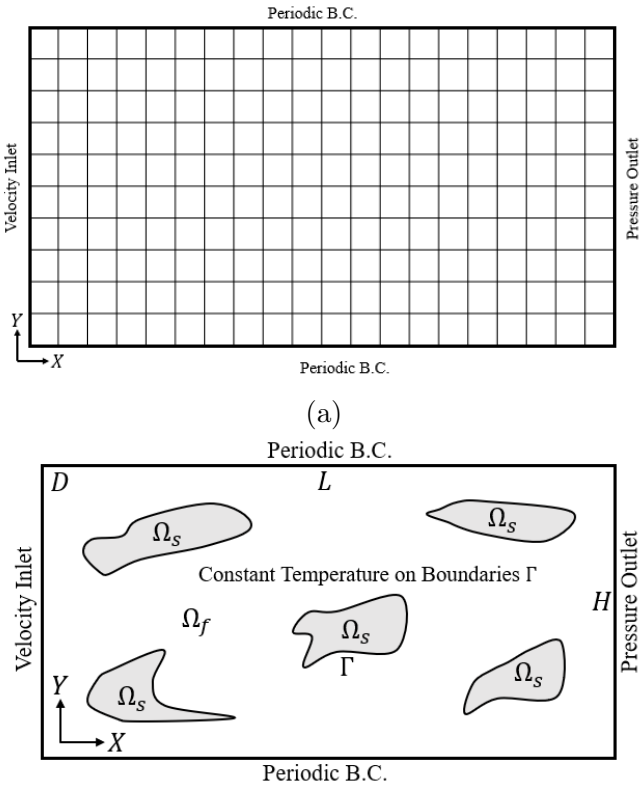

Figure 6.1: Setting of design space exploration for (a) discrete space, and (b) BREP space

6.2.1 High Fidelity Environment

High fidelity simulation engine is the same as what was mentioned in chapter 4. Here, mesh heuristic for multiple shape inside the domain is presented. five sets of geometries are considered which are randomly sampled among the shapes constructed during primary running of the framework. The same clipping method described in chapter 4 is used for MARL framework. However, with the increase in the number of shapes, minimum mesh size is set to be L/150, and number of meshes between points remain higher than 12. Minimum number of meshes are decreased compared to the single-agent framework; in case

of single shape, the meshes were constructed between the shape with small meshes and boundaries of the domain with larger cells. In MARL framework, meshes are constructed between multiple shapes with small cells on their boundaries which result in high number of meshes. Fig 6.2 shows the meshes constructed in a selected geometry. Implementation of this method results in number of grids between 22,000 and 30,000 which depend on the size and shape of the geometries. Figure 6.3 shows the mesh heuristics based on the minimum cell numbers between the points. It can be seen that after considering minimum of 12 cells between the points, amounts of heat transfer remain consistent.

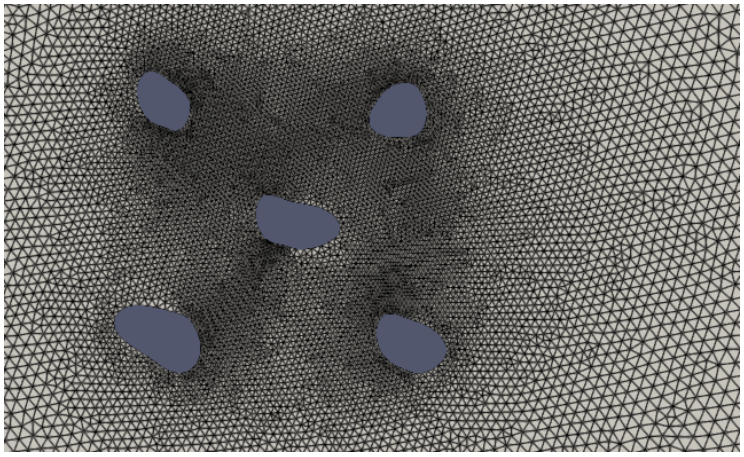

Figure 6.2: Body-fitted mesh resolution of a selected geometry in multi-agent framework

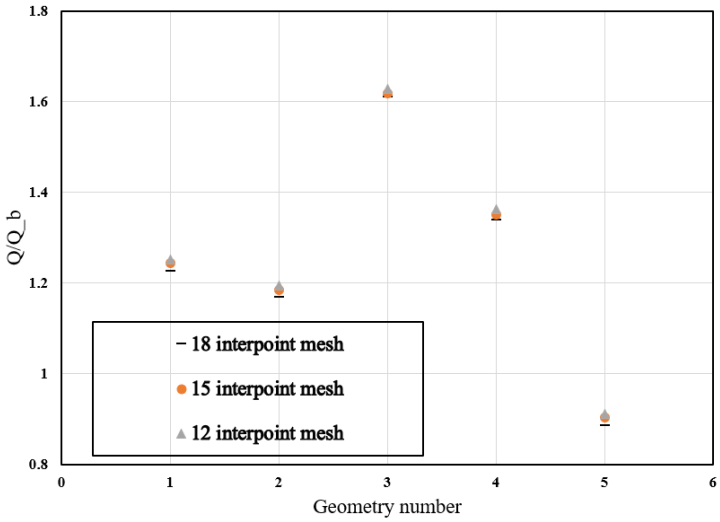

Figure 6.3: Dimensionless heat transfer for five random geometry settings with different meshing sizes at Re = 10 and Pr = 0.7

6.2.2 Surrogate Model Environment

An increase in number of shapes and control points results in larger action space which requires more iteration for policy learning. Therefore, a surrogate model is required to enhance the speed of learning. In chapter 5, a surrogate model for a single shape was provided. Here, an Xception network [148] is trained as a surrogate model to predict heat transfer and pressure drop directly from the generated multishape geometries. This selection is based on the superiority of the Xception network that was seen in chapter 5 for the case with single shape. 34,000 images generated using four and five control points along with their CFD results are used for training the surrogate model. The size and resolution of the images are considered to be constant with a single channel, and 506 $\times$ 506 pixels.

6.2.3 Multi-Agent Reinforcement Learning

In chapter 4, we used PPO as a single agent RL algorithm for shape optimization of a single fin. Here, we use Multi-Agent PPO (MAPPO) which shares the same algorithm as the single-agent PPO. CTDE is used with homogeneous agents utilizing parameter sharing. The agents learn from the state gathered from all the agents and act independently based on their own state observation. Input value function becomes important since more accuracy

in value function can reduce the variance in policy updates. In MAPPO used in the current study, value function receives global state on top of the state observation for each agent. Fig. 6.4 shows the MAPPO framework used in this research. In order to study the difference between the centralized and decentralized learning, a multi-agent benchmark environment is considered. Particle-world environment (MPE) with multiple agents is experimented with a decentralized execution and both case of centralized and decentralized learning. Please refer to Lowe et al. [166] for further details about the MPE environment. Benchmark MARL is implemented in PyTorch while GD framework is implemented using Tensorflow.

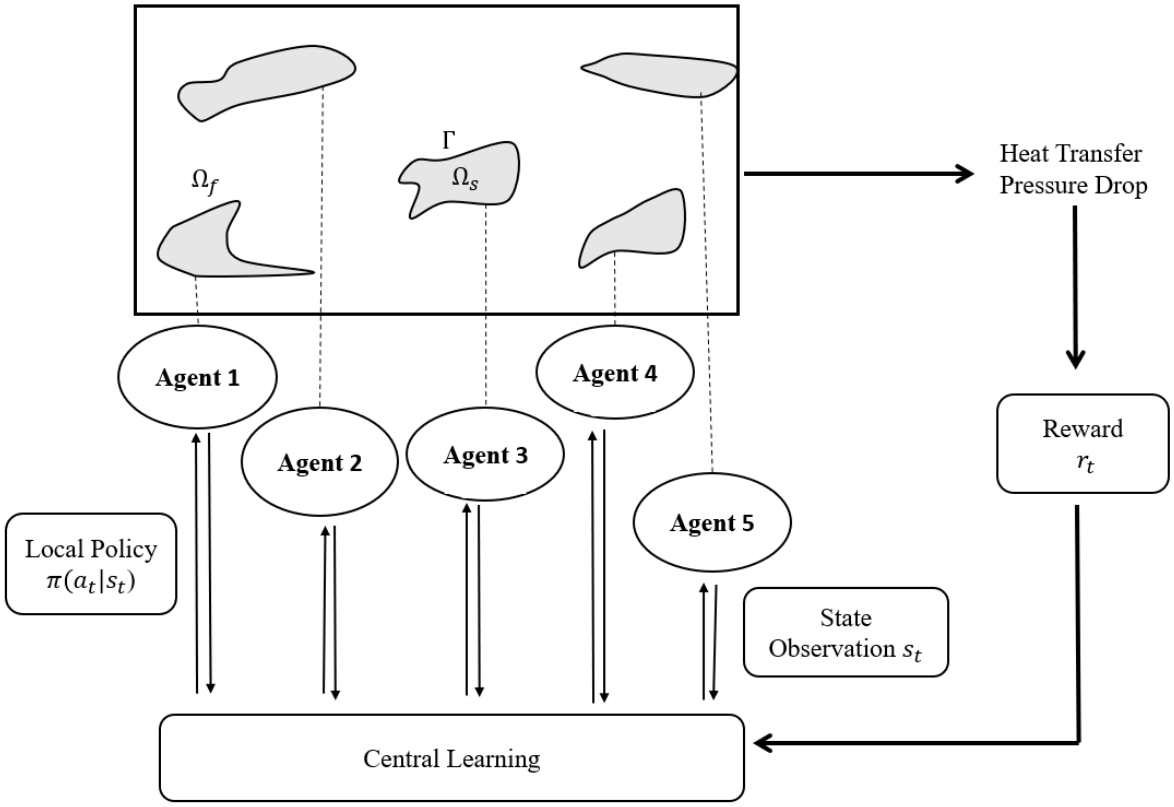

Figure 6.4: Multi-agent framework for multiple shape optimization

Each agent is responsible for the geometry of one single shape taking action a_i using shared policy π_θ with parameters θ. The heat transfer domain is a combination of geometries produced by actions $A = (a_1, ..., a_n)$ in which n is the number of agents. Each shape

is allowed to occupy a rectangle with the size of $H/4$ and $L/3$. Therefore, all agents act in the same environment with the same action space.

6.3 Experiments

All experiments were conducted on a single workstation equipped with Ubuntu 20.04 LTS, 16-Core Processor 3.40 GHz CPU, 32.0 GB RAM, and one GeForce RTX 3080 Graphics Processing Units (GPUs). Python 3.8.9, TensorFlow, PyTorch, Keras, and Tensorforce are used for ML implementation, as well as multiprocessing to leverage multiple processors for parallel computing.

6.3.1 Experiments for Model Accuracy

Temperature profile for a collection of random geometries from the dataset that is used for training the Xception network is shown in Fig. 6.5. Unity-based normalization is used since heat transfer values for five shapes can go above 1000 watts.

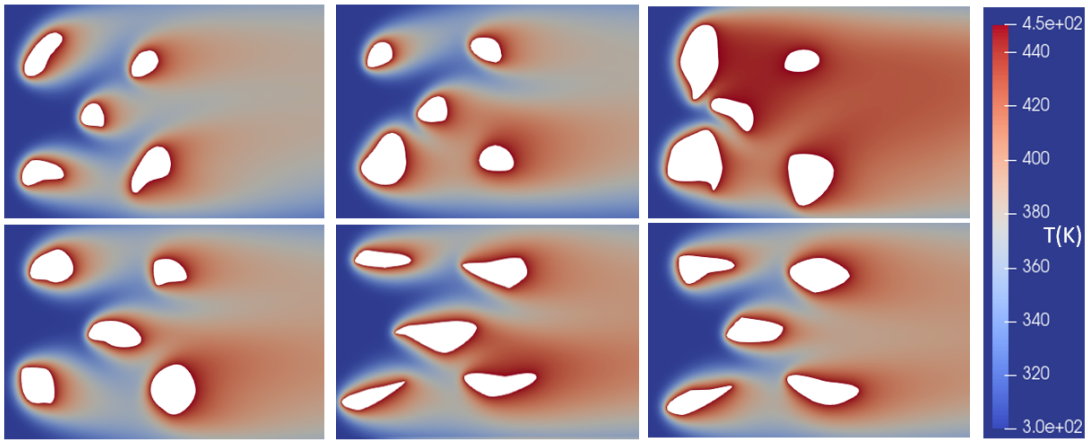

Figure 6.5: A collection of random shapes in the dataset which is used for training the surrogate model of the physics for the case with multiple shapes inside the domain

First, the performance of the surrogate model is shown here. Fig. 6.6 shows the residual for heat transfer test dataset with the size of 200 images. Comparing the surrogate model

performance to the ones presented in chapter 5, it can be inferred that by increasing the number of shapes and consequently DOF, accuracy of the machine learning model decreases. Challenges to improve the ML model for higher accuracy remains open for ML community and competitions. Our takeaway from the error behavior is that increasing design freedom is associated with sacrificing accuracy in prediction. Higher DOF in design requires larger dataset for training the surrogate model. The model shows a reasonable performance with R^2 values of 0.968 and MAE of 0.032. Residual plot shows that overall bias of the model can be considered very little to none. Normal distribution of the residual with a center at almost zero residual shows the high accuracy of the model. The distribution of the data on top of the chart in Fig. 6.6 shows that the center of the distribution is around the Q/Q_b value of 1.3 which is associated with minimum residual as well. This provides high accuracy around this point which will be discussed in MARL results. In general, the model overestimates the larger values of heat transfer and underestimates the smaller values. However, order of errors are small and can be considered as an accurate model. Fig 6.7 shows predicted and ground truth values with 99 percent confidence interval around the identity line. As can be seen, the model can be used for heat transfer prediction with high confidence.

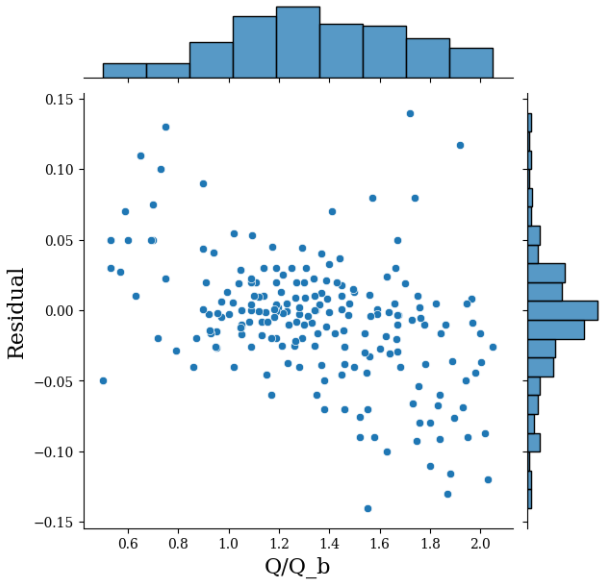

Figure 6.6: Residual plot of heat transfer prediction for multiple fin shapes

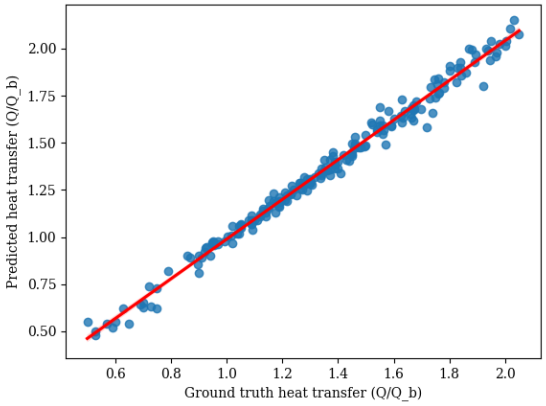

Figure 6.7: Predicted and ground truth heat transfer for multiple shape surrogate environment (99 percent confidence interval is also plotted around the identity line)

Xception network is also used for pressure drop prediction with minimum hyperparameter search and without any specific changes. Further details are provided in Appendix A.6. Fig 6.8 shows the residual plot for Xception network trained for pressure drop prediction. Residual plot for pressure drop shows almost a normal distribution centered around zero value which indicates the model is fitted properly. Coefficient of determination is reported to be 0.98. Higher distribution is seen between the Dp/Dp_b of 0.6 and 0.8 which is due to fact that some portion of the data are collected during the primary attempts to use the MARL framework without a surrogate model. Residual values are close to zero in this region which is valuable to use the trained model as an estimator engine in the RL algorithm. MAE value of 0.033 is reported which is close to the heat transfer prediction value.

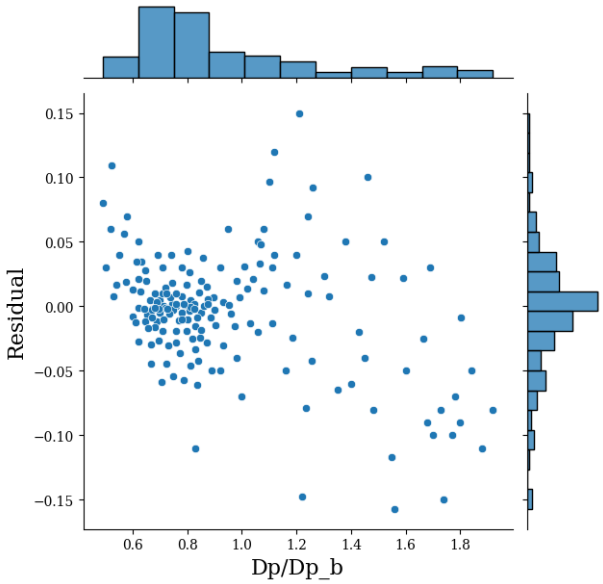

Figure 6.8: Residual plot of pressure drop values for multiple shape surrogate model

Fig. 6.9 shows estimated values of pressure drop and actual values computed using high fidelity simulation. The red line shows the identity line with 99 percent confidence interval around the line. Less confidence around the higher values of pressure drop are seen. However, 99 percent confidence is of great value for design automation tasks.

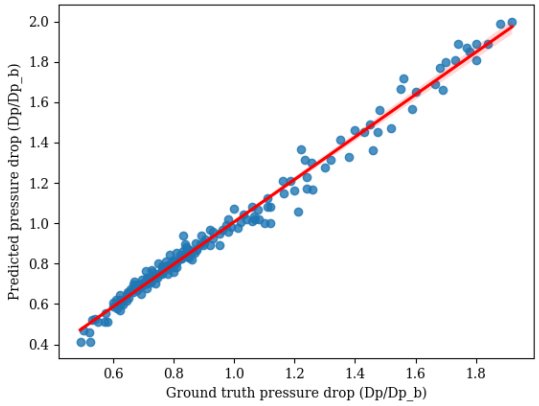

Figure 6.9: Predicted and ground truth values of pressure drop with 99 percent confidence interval for multiple shape estimation using Xception network

6.3.2 Experiments for Multi-agent Generative Design

In MARL method, the action of each agent is to change the position of the points pertinent to the assigned shape. High dimension of the multi-agent framework makes it crucial to select the input to value function optimally.

First, we present the results for the MPE as a primary assessment of the CTDE performance for high dimensional environment. Two cooperative MPE scenarios are experimented. In these environments, the collective reward incentivizes collaboration between the agents. The results for simple reference MPE with two agents and three landmarks, and simple spread MPE are presented. As it can be seen in Fig. 6.10, centralized learning provides higher reward and faster convergence in simple reference MPE benchmark environment. Fig. 6.11 shows the learning curve for simple spread scenario with five agents and five landmarks which demonstrates a clear outperformance of the CTDE method for high number of agents. Simple spread MPEs with lower number of agents show less difference in performance using different value learning methods. However, increasing the number of agents and landmarks shows that centralized value learning outperforms the fully independent method. This shows centralized learning while executing in a decentralized way provides better convergence for high dimensional environments. Hyperparameters used for the simple reference and simple spread MPE are available at A.7 and A.8, respectively.

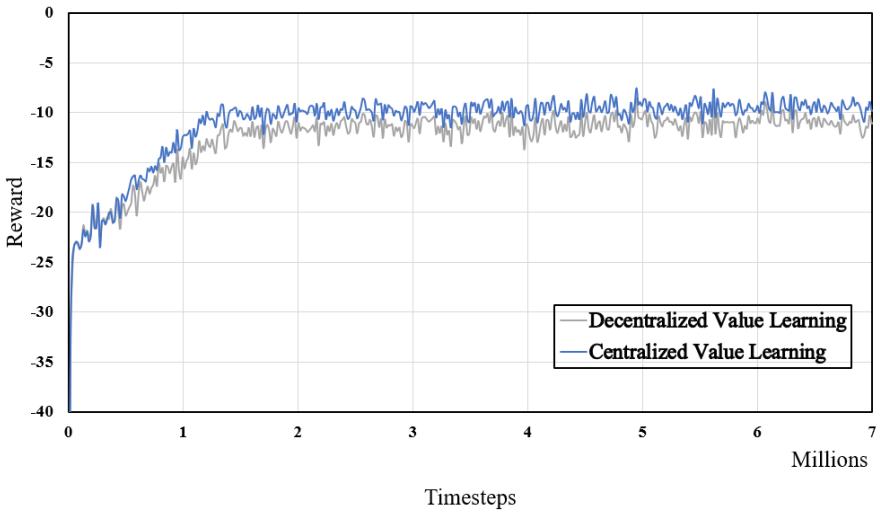

Figure 6.10: Reward history during training the simple reference MPE

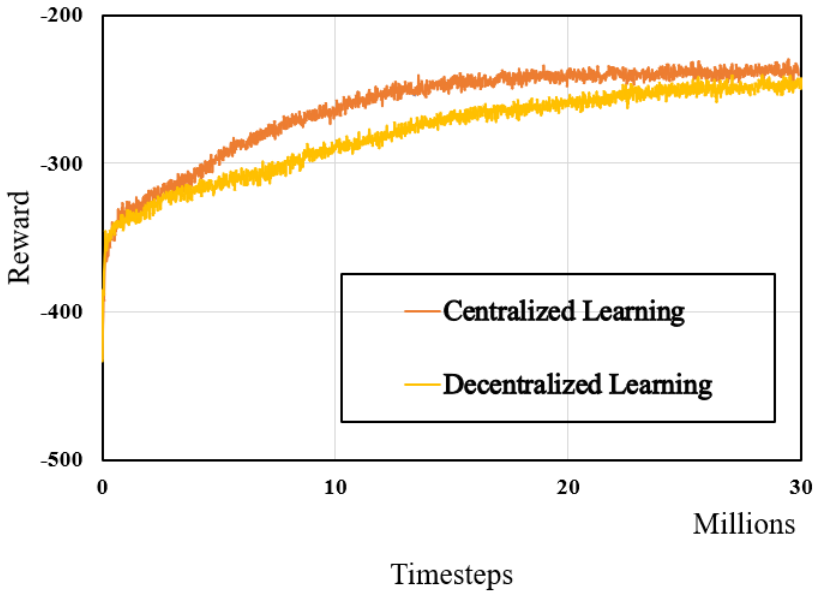

Figure 6.11: Reward history during training the simple spread MPE

Different methods for passing the state vector to the value function of the MARL framework for GD was experimented. In case of value function receiving a global state observation of the points, better preliminary learning is observed in GD framework. Decentralized learning does not provide convergence in GD framework. This might be due to the fact that our state observation vector is not a high dimensional state such as those in pixel dimension of images. The state observation is a numpy array with the same size as the DOF and action vector. Value function is crucial in convergence when the state and action space both are increased in the same time. Therefore, multiple timesteps is considered in each episode to benefit from value learning while our reward can be obtained in each timestep. Parallel training is used to run the surrogate environment with 16 parallel environments and a batch size of 40. Hyperparameters for MAPPO can be found in appendix A.9. Reward is the desired output which is heat transfer divided to cost which is pressure drop. An ideal array of fins fin is expected to cause maximum heat transfer and minimum pressure drop. The reward function is considered to be calculated the same as single-agent framework using Webb and Eckert according to Eq. 6.1 which is an objective widely used in heat transfer community. The agents find optimal policies that can maximize the discounted cumulative reward. The reward function, presented in the Eq. 6.1 guides the network toward the pressure drop reduction and heat transfer enhancement through changing the boundaries of each shape separately.

$$r_t = \frac{Q}{Dp^{1/3}} \tag{6.1}$$

Fig. 6.12 shows the shape evolution of multiple shapes during the learning process of the MARL framework at Re = 10, and Pr = 0.7. It can be seen starting from a reference geometry, agents find the policy to optimize the shapes. However, agents fail to establish symmetry in geometry while the physics of the problem is symmetric since each agent acts independently. It is important to mention that the shapes in Fig. 6.12 are selected intentionally with the highest symmetry in the shapes. Most of the well-performing design solutions lack the symmetry in solution.

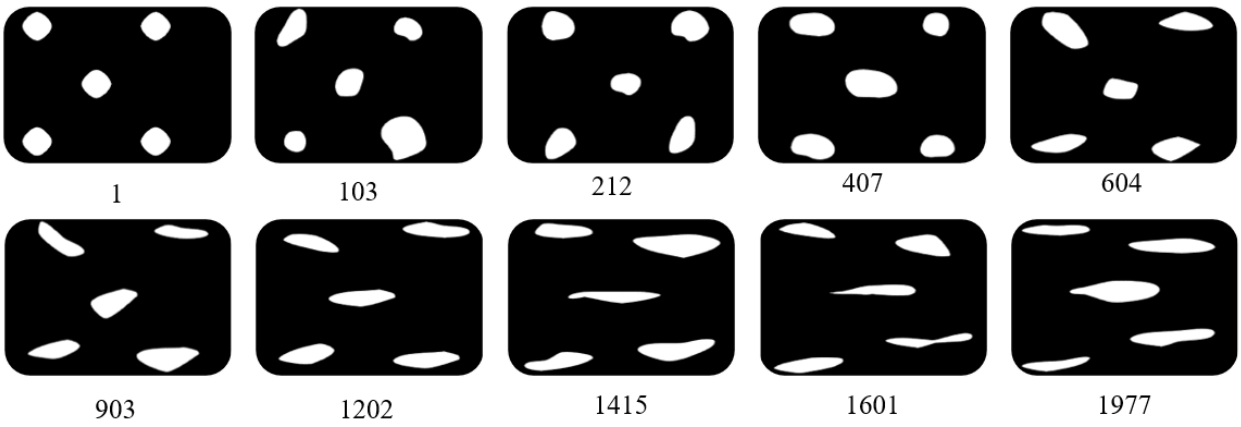

Figure 6.12: Shape evolution during the learning process in multi-agent framework

Fig. 6.13 shows the reward history during the training of the MARL framework. Both instantaneous and moving averaged rewards are shown in the figure. In chapter 4, it was seen that the reward of the single shape with 15 DOF reaches a plateau after less than 300 episodes of training. MARL framework with five agents has a large action space. However, after less than 2000 episodes and almost two hours of training, well-performing design with increased performance are generated. It is important to mentioned that, parallel environments are used in this study. Therefore, experience seen by the agent is larger than the episode in Fig 6.13.

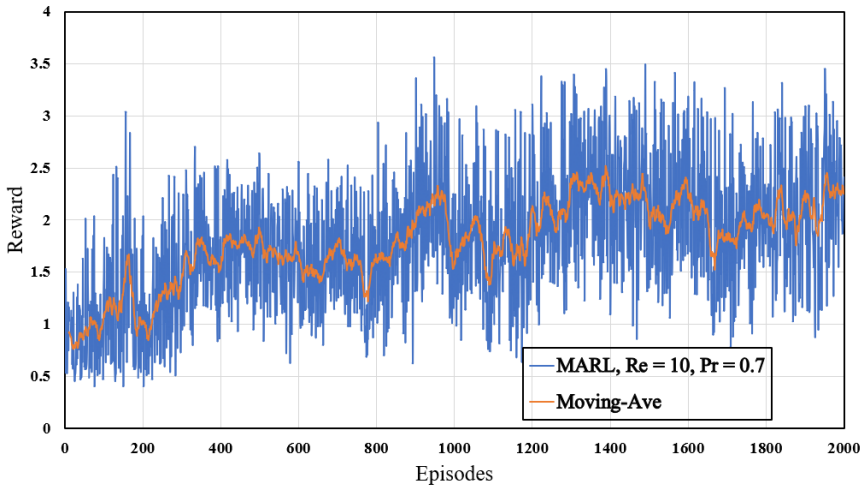

Figure 6.13: Instantaneous and moving averaged reward during training of the MARL framework

Fig. 6.14 and Fig. 6.15 show temperature profile for one of the well-performing designs and reference design, respectively.

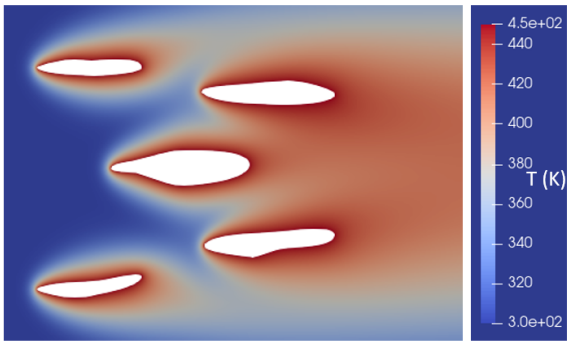

Figure 6.14: Temperature profile for one of the well-performing designs in case of multi-agent framework

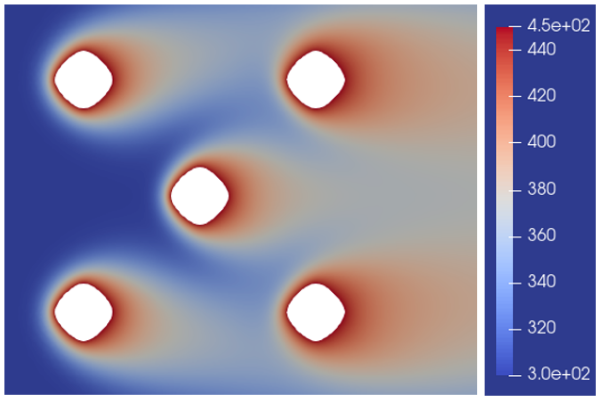

Figure 6.15: Temperature profile for the reference geometry in MARL method

Fig 6.16 shows the dimensionless heat transfer and pressure drop with respect to the reference geometry for Pareto front design solutions. It can be seen that even for low Reynolds number and large Prandtl number ($Re = 10, Pr = 0.7$) which results in less heat transfer, over 25 percent increase in heat transfer and 25 percent reduction in pressure drop are seen in well-performing designs. This results prove the effectiveness and robustness of the developed framework for heat exchanger design automation.

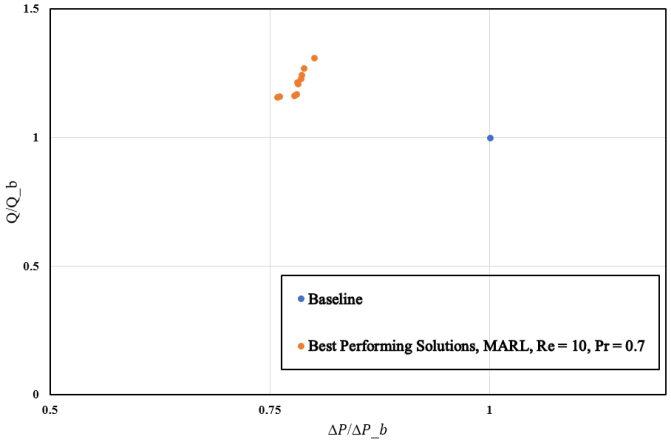

Figure 6.16: Dimensionless heat transfer and pressure drop with respect to the reference geometry for the best performing designs in MARL framework

Considering that the efficiency of fins in engineering application is high [167], two dimensional framework developed assuming constant temperature is a practical implemen-

tation. There might be a special research need for expanding the current framework to three dimensions for which the action and state space are the same as 2D case. The Open CASCADE library inside the FEniCs provides a convenient extrusion of the geometry by adding a dimension in the third coordinate for each fin. Three dimensional implementation can add one degree of freedom for the height of each fin. 3D simulation requires higher computation time for one iteration of learning and surrogate-assisted RL is necessary for achieving high performance design.

6.4 Conclusion

In this chapter, multi-agent deep reinforcement learning was used to generate multiple optimized fin shapes directly from boundary representation. Centralized training and decentralized execution (CTDE) was used to train reinforcement learning agents for the large continuous action space of up to four control points for each shape. An Xception network was used as a surrogate model to provide accelerated iterative process for agents. Utilizing accelerated experience of the agents from the surrogate model, multiple shapes with enhanced performance were generated.

Chapter 7

Summary, Conclusion and Future Work

7.1 Summary and Conclusion

This dissertation was developed to address the growing need in computational design methods for microscale thermal devices.

Genetic algorithm along with commercial software were used for heat exchanger size optimization which do not provide an efficient use of both time and space. This often resulted in manufacturing challenges imposed by inefficient use of design space.

A deep reinforcement learning approach which uses parallel environments for heat transfer computation was proposed for the optimization of fin shape. An existing problem in micro-scale thermal shape and topology optimization was addressed by introducing boundary representation approach that provides clear boundary condition throughout the optimization process. The introduced method requires high fidelity simulation in each episode of training. High fidelity computation is a CPU-intensive task which requires enormous memory space to save computation in each node during the simulation. Occasional failed computation is expected when running for multiple different geometries. Final optimization result is not affected by the failed computation, but the robustness of the framework is.

Modern convolutional neural networks were utilized to predict heat transfer and pressure drop of the shapes generated using composite Bézier curve without expensive CFD

computation. Time-averaged CFD results were predicted directly from images of the geometries without using mesh representations. This provides a reduction in time required for heat transfer and pressure drop computation from several minutes to less than two seconds. An optimized CNN network using regular convolutions as well as an Xception model were deployed to predict the CFD results with high level of accuracy. Xception network provided more robust prediction compared to regular CNN which then used for larger problem.

The design space was expanded to multiple shape optimization through multi-agent reinforcement learning. Proximal policy optimization was used for multi-agent framework in which each agent takes action to optimize a specified fin shape. These agents work cooperatively with other agents toward maximizing a shared reward by changing the control points of composite Bézier curves. In order to provide accelerated experience for agents, pre-trained Xception networks were used in an environment to predict heat transfer and pressure drop of the generated geometries in few seconds. These developments resulted in a framework for generative thermal design using cooperative environment and continuous geometric representation of the fluid and solid domain. It was shown that the developed multi-agent framework can learn the policy for design strategy using multi-objective reward without the need for shape derivation or differentiable objective function. A Centralized Training Decentralized Execution (CTDE) method was utilized to tackle the instability in learning of the multiple agent and high dimensional design space. The effectiveness of this method for high dimensional space was also proved using benchmark multi-agent particle world environment.

The superiority of the proposed method in low dimensional state and action space as well as the feasibility of the framework for large action space were demonstrated. The extension of the method remains for future research to explore the performance of the proposed method in real world engineering design which is provided in the next section.

7.2 Limitations and Future Work

Several research opportunities are opened based on the findings and limitations of the current research. Bellow, the main avenues are described.

7.2.1 Utilization of Transfer Learning to Minimize the Need for High Fidelity Simulation

Current study showed that using surrogate models provided by convolutional networks can accelerated iterative process in generative design. However, the supervised learning provided in this study requires a large labeled dataset which is not an efficient way to develop a surrogate model. A comprehensive study is required for using advanced transfer learning methods to fully utilize the available archive data toward a reliable surrogate model that can be used with high accuracy in design automation process. Topology-aware graph neural network which uses a graph to structure the data for the geometry is a viable option for developing a sample-efficient surrogate model. In this method, instead of the images with high dimensional pixels, the topology of the fins can be stored in graphs saving the information of the entire geometry. These graphs can be used for a neural network surrogate model.

7.2.2 Action Masking and Sample Efficiency in Design Automation

Action masking was used in discrete action spaces in order to avoid invalid actions. In heat transfer simulation, eliminating actions that are computationally demanding would save optimization time. There is no solid report on sample efficiency of action masking in real world continuous task such as the one implemented in this study. Sample efficiency is the key to the effectiveness of the design automation. In this research work, only preliminary investigation was performed on the effect of state observation on the learning of multi-agent framework. A comprehensive study on a combination of state observation as an input for value function is another immediate avenue of research.

7.2.3 Bridging the Gap Between Virtual Simulation and Real World Manufacturing

In chapter 3, a method that was developed by previous researchers was used for a real world design automation and manufacturing challenge. From chapter 4 to the end of this contribution, a new method addressing the existing problems in design automation was developed. It would be a great opportunity for a hands-on researcher to utilize this method for an industry-level development with specified target performance. In case three

dimensional framework is required for particular boundary conditions or working fluids, e.g. slip flow, details for extrusion in Open CASCADE is explained in chapter 6.

References

[1] B. Alm, R. Knitter, J. Hausselt, Development of a ceramic micro heat exchanger–design, construction, and testing, Chemical Engineering & Technology: Industrial Chemistry-Plant Equipment-Process Engineering-Biotechnology 28 (12) (2005) 1554–1560.

[2] A. D. Series, High-temperature characteristics of stainless steels, Nickel Development Institute, American Iron and Steel Institute.

[3] M. Anheden, Analysis of gas turbine systems for sustainable energy conversion, Ph.D. thesis, Kemiteknik (2000).

[4] H. Keramati, F. Battaglia, M. A. Arie, F. Singer, M. M. Ohadi, Additive manufacturing of compact manifold-microchannel heat exchangers utilizing direct metal laser sintering, in: 2019 18th IEEE Intersociety Conference on Thermal and Thermomechanical Phenomena in Electronic Systems (ITherm), IEEE, 2019, pp. 423–429.

[5] X. Zhang, H. Keramati, M. Arie, F. Singer, R. Tiwari, A. Shooshtari, M. Ohadi, Recent developments in high temperature heat exchangers: A review.

[6] S. Oh, Y. Jung, S. Kim, I. Lee, N. Kang, Deep generative design: Integration of topology optimization and generative models, Journal of Mechanical Design 141 (11).

[7] L. Regenwetter, A. H. Nobari, F. Ahmed, Deep generative models in engineering design: A review, Journal of Mechanical Design 144 (7) (2022) 071704.

[8] J. Viquerat, E. Hachem, A supervised neural network for drag prediction of arbitrary 2d shapes in laminar flows at low reynolds number, Computers & Fluids 210 (2020) 104645.

[9] A. Sanchez-Gonzalez, N. Heess, J. T. Springenberg, J. Merel, M. Riedmiller, R. Hadsell, P. Battaglia, Graph networks as learnable physics engines for inference and control, in: International Conference on Machine Learning, PMLR, 2018, pp. 4470–4479.

[10] C. Deng, Y. Wang, C. Qin, Y. Fu, W. Lu, Self-directed online machine learning for topology optimization, Nature Communications 13 (1) (2022) 1–14.

[11] X. Chen, R. Chen, Q. Wan, R. Xu, J. Liu, An improved data-free surrogate model for solving partial differential equations using deep neural networks, Scientific Reports 11 (1) (2021) 1–17.

[12] T. Kodippili, S. Lambert, A. Arami, Data-driven prediction of forging outcome: Effect of preform shape on plastic strain in a magnesium alloy forging, Materials Today Communications 31 (2022) 103210.

[13] F. Feppon, G. Allaire, C. Dapogny, P. Jolivet, Topology optimization of thermal fluid–structure systems using body-fitted meshes and parallel computing, Journal of Computational Physics 417 (2020) 109574.

[14] D. Wen, Nanoparticle-related heat transfer phenomenon and its application in biomedical fields, Heat transfer engineering 34 (14) (2013) 1171–1179.

[15] J. S. Lee, S. Y. Yoon, B. Kim, H. Lee, M. Y. Ha, J. K. Min, A topology optimization based design of a liquid-cooled heat sink with cylindrical pin fins having varying pitch, International Journal of Heat and Mass Transfer 172 (2021) 121172.

[16] R. Foresti, S. Rossi, S. Selleri, Bio composite materials: Nano functionalization of 4D bio engineered scaffold, in: 2019 IEEE International Conference on BioPhotonics (BioPhotonics), IEEE, 2019, pp. 1–2.

[17] G. Pingen, K. Maute, Optimal design for non-newtonian flows using a topology optimization approach, Computers & Mathematics with Applications 59 (7) (2010) 2340–2350.

[18] B. Zhang, X. Liu, J. Sun, Topology optimization design of non-newtonian roller-type viscous micropumps, Structural and Multidisciplinary Optimization 53 (3) (2016) 409–424.

[19] K. E. S. Hasund, Topology optimization for unsteady flow with applications in biomedical flows, Master's thesis, NTNU (2017).

[20] D. H. Alonso, E. C. N. Silva, Topology optimization for blood flow considering a hemolysis model, Structural and Multidisciplinary Optimization 63 (5) (2021) 2101–2123.

[21] B. Zhang, X. Liu, Topology optimization study of arterial bypass configurations using the level set method, Structural and Multidisciplinary Optimization 51 (3) (2015) 773–798.

[22] B. S. Mekki, J. Langer, S. Lynch, Genetic algorithm based topology optimization of heat exchanger fins used in aerospace applications, International Journal of Heat and Mass Transfer 170 (2021) 121002.

[23] L. A. Rocha, S. Lorente, A. Bejan, Constructal Law and the unifying principle of design, Springer, 2012.

[24] A. Bejan, S. Lorente, The constructal law and the evolution of design in nature, Physics of life Reviews 8 (3) (2011) 209–240.

[25] W. Zhang, Q. Jiang, W. Feng, S.-K. Youn, X. Guo, Explicit structural topology optimization using boundary element method-based moving morphable void approach, International Journal for Numerical Methods in Engineering 122 (21) (2021) 6155–6179.

[26] X. Guo, W. Zhang, W. Zhong, Doing topology optimization explicitly and geometrically—a new moving morphable components based framework, Journal of Applied Mechanics 81 (8).

[27] X. Qian, Topology optimization in b-spline space, Computer Methods in Applied Mechanics and Engineering 265 (2013) 15–35.

[28] T. J. Hughes, J. A. Cottrell, Y. Bazilevs, Isogeometric analysis: Cad, finite elements, nurbs, exact geometry and mesh refinement, Computer methods in applied mechanics and engineering 194 (39-41) (2005) 4135–4195.

[29] C. F. McDonald, Low-cost compact primary surface recuperator concept for microturbines, Applied Thermal Engineering 20 (5) (2000) 471–497.

[30] M. M. Ohadi, S. G. Buckley, High temperature heat exchangers and microscale combustion systems: applications to thermal system miniaturization, in: Thermal Sciences 2000. Proceedings of the International Thermal Science Seminar. Volume 1, Begel House Inc., 2000.

[31] X. Zhang, M. A. Arie, D. Deisenroth, A. Shooshtari, S. Dessiatoun, M. Ohadi, Impact of additive manufacturing on performance enhancement of heat exchangers: a case study on an air-to-air heat exchanger for high temperature applications, in: IX Minsk International Seminar on Heat Pipes, Heat Pumps, Refrigerators, Power Sources, 2015, pp. 7–10.

[32] K. Thulukkanam, Heat exchanger design handbook, CRC press, 2000.

[33] K. Brun, P. Friedman, R. Dennis, Fundamentals and applications of supercritical carbon dioxide (sCO2) based power cycles, Woodhead publishing, 2017.

[34] L. Chordia, M. A. Portnoff, E. Green, High temperature heat exchanger design and fabrication for systems with large pressure differentials, Tech. rep., Thar Energy, LLC, Pittsburgh, PA (United States) (2017).

[35] R. Smyth, A proposal for the use of a very high temperature ceramic heat exchanger in gas turbine power production, in: IECEC-97 Proceedings of the Thirty-Second Intersociety Energy Conversion Engineering Conference (Cat. No. 97CH6203), Vol. 3, IEEE, 1997, pp. 1696–1701.

[36] D. Aquaro, M. Pieve, High temperature heat exchangers for power plants: Performance of advanced metallic recuperators, Applied Thermal Engineering 27 (2-3) (2007) 389–400.

[37] C. F. McDonald, Recuperator considerations for future higher efficiency microturbines, Applied Thermal Engineering 23 (12) (2003) 1463–1487.

[38] B. Sunden, High temperature heat exchangers (hthe), in: Proceedings of the 5th International Conference on Science, Engineering and Technology, VIT University, Vellore, India, 2005.

[39] I. Nikulin, R. Kaibyshev, V. Skorobogatykh, High temperature properties of an austenitic stainless steel, in: Journal of Physics: Conference Series, Vol. 240, IOP Publishing, 2010, p. 012071.

[40] M. Ohadi, X. Zhang, H. Keramati, M. Arie, F. Singer, R. Tiwari, A. Shooshtari, Recent developments in high temperature heat exchangers: A review, Frontiers in Heat and Mass Transfer (FHMT) 11.

[41] N. EFSA Panel on Dietetic Products, A. (NDA), Scientific opinion on dietary reference values for chromium, EFSA Journal 12 (10) (2014) 3845.

[42] S. Zhang, W. Seiya, 3d printing as an alternative manufacturingmethod for the micro gas turbine heat exchanger (2015).

[43] E. B. Magrab, S. K. Gupta, F. P. McCluskey, P. Sandborn, Integrated product and process design and development: the product realization process, CRC Press, 2009.

[44] Q. Li, G. Flamant, X. Yuan, P. Neveu, L. Luo, Compact heat exchangers: A review and future applications for a new generation of high temperature solar receivers, Renewable and Sustainable Energy Reviews 15 (9) (2011) 4855–4875.

[45] C. Luzzatto, A. Morgana, S. Chaudourne, T. O'Doherty, G. Sorbie, A new concept composite heat exchanger to be applied in high-temperature industrial processes, Applied Thermal Engineering 17 (8-10) (1997) 789–797.

[46] J. Schulte-Fischedick, V. Dreißigacker, R. Tamme, An innovative ceramic high temperature plate-fin heat exchanger for efcc processes, Applied Thermal Engineering 27 (8-9) (2007) 1285–1294.

[47] C. Schmitt, D. W. Agar, F. Platte, S. Buijssen, B. Pawlowski, M. Duisberg, Ceramic plate heat exchanger for heterogeneous gas phase reactions, Chemical Engineering & Technology: Industrial Chemistry-Plant Equipment-Process Engineering-Biotechnology 28 (3) (2005) 337–343.

[48] M. Rohde, I. Südmeyer, A. Urbanek, M. Torge, Joining of alumina and steel by a laser supported brazing process, Ceramics International 35 (1) (2009) 333–337.

[49] A. Sommers, Q. Wang, X. Han, C. T'Joen, Y. Park, A. Jacobi, Ceramics and ceramic matrix composites for heat exchangers in advanced thermal systems—a review, Applied Thermal Engineering 30 (11-12) (2010) 1277–1291.

[50] M. A. Arie, A. H. Shooshtari, V. V. Rao, S. V. Dessiatoun, M. M. Ohadi, Air-side heat transfer enhancement utilizing design optimization and an additive manufacturing technique, Journal of Heat Transfer 139 (3).

[51] S. Kandlikar, S. Garimella, D. Li, S. Colin, M. R. King, Heat transfer and fluid flow in minichannels and microchannels, elsevier, 2005.

[52] M. A. Arie, A. H. Shooshtari, R. Tiwari, S. V. Dessiatoun, M. M. Ohadi, J. M. Pearce, Experimental characterization of heat transfer in an additively manufactured polymer heat exchanger, Applied Thermal Engineering 113 (2017) 575–584.

[53] W. D. Gerstler, D. Erno, Introduction of an additively manufactured multi-furcating heat exchanger, in: 2017 16th IEEE Intersociety Conference on Thermal and Thermomechanical Phenomena in Electronic Systems (ITherm), IEEE, 2017, pp. 624–633.

[54] E. Utriainen, B. Sunde´ n, Evaluation of the cross corrugated and some other candidate heat transfer surfaces for microturbine recuperators, J. Eng. Gas Turbines Power 124 (3) (2002) 550–560.

[55] J. Stasiek, Experimental studies of heat transfer and fluid flow across corrugated-undulated heat exchanger surfaces, International Journal of Heat and Mass Transfer 41 (6-7) (1998) 899–914.

[56] J.-W. Seo, C. Cho, S. Lee, Y.-D. Choi, Thermal characteristics of a primary surface heat exchanger with corrugated channels, Entropy 18 (1) (2016) 15.

[57] W. M. Rohsenow, J. P. Hartnett, Y. I. Cho, et al., Handbook of heat transfer, Vol. 3, McGraw-Hill New York, 1998.

[58] E. Lara-Curzio, P. Maziasz, B. Pint, M. Stewart, D. Hamrin, N. Lipovich, D. DeMore, Test facility for screening and evaluating candidate materials for advanced microturbine recuperators, in: Turbo Expo: Power for Land, Sea, and Air, Vol. 36061, 2002, pp. 1135–1141.

[59] S. A. David, J. Siefert, J. DuPont, J. Shingledecker, Weldability and weld performance of candidate nickel base superalloys for advanced ultrasupercritical fossil power plants part i: fundamentals, Science and Technology of Welding and Joining 20 (7) (2015) 532–552.

[60] M. A. Arie, Air side heat transfer enhancement in heat exchangers utilizing innovative designs and the additive manufacturing technique, Ph.D. thesis (2016).

[61] D. C. Deisenroth, R. Moradi, A. H. Shooshtari, F. Singer, A. Bar-Cohen, M. Ohadi, Review of heat exchangers enabled by polymer and polymer composite additive manufacturing, Heat Transfer Engineering 39 (19) (2018) 1648–1664.

[62] E. Cetegen, Force fed microchannel high heat flux cooling utilizing microgrooved surfaces, University of Maryland, College Park, 2010.

[63] R. Tiwari, R. S. Andhare, A. Shooshtari, M. Ohadi, Development of an additive manufacturing-enabled compact manifold microchannel heat exchanger, Applied Thermal Engineering 147 (2019) 781–788.

[64] M. Ohadi, K. Choo, S. Dessiatoun, E. Cetegen, Next generation microchannel heat exchangers, Springer, 2013.

[65] X. Zhang, R. Tiwari, A. H. Shooshtari, M. M. Ohadi, An additively manufactured metallic manifold-microchannel heat exchanger for high temperature applications, Applied Thermal Engineering 143 (2018) 899–908.

[66] M. Eesa, G. Marriott, Photochemical etching of heat exchanger plates (2018).

[67] D. Shiferaw, R. Broad, Diffusion bonded heat exchangers (pches) in fuel gas heating to improve efficiency of ccgts, in: ASME Power Conference, Vol. 46087, American Society of Mechanical Engineers, 2014, p. V001T03A001.

[68] M. Ferrato, B. Thonon, A compact ceramic plate-fin heat exchanger for gas turbine heat recovery, in: Compact Heat Exchangers for the Process Industries, Begel House Inc., 1997.

[69] L. Federzoni, J.-A. Gruss, J.-A. Brochard, Heat exchanger manufactured by ceramic injection moulding, in: CFM 2007-18ème Congrès Français de Mécanique, AFM, Maison de la Mécanique, 39/41 rue Louis Blanc-92400 Courbevoie, 2007.

[70] J. Schmidt, M. Scheiffele, M. Crippa, P. F. Peterson, E. Urquiza, K. Sridharan, L. C. Olson, M. H. Anderson, T. R. Allen, Y. Chen, Design, fabrication, and testing of ceramic plate-type heat exchangers with integrated flow channel design, International Journal of Applied Ceramic Technology 8 (5) (2011) 1073–1086.

[71] H. Strumpf, D. Kotchick, M. Coombs, High-temperature ceramic heat exchanger element for a solar thermal receiver.

[72] P. F. Peterson, H. Zhao, F. Niu, W. Huang, J. Schmidt, J. Schulte-Fischedick, Development of C-SiC Seramic Compact Plate Heat Exchangers for High Temperature Heat Transfer Applications, American Institute of Chemical Engineers, 2006.

[73] C. A. Lewinsohn, M. A. Wilson, J. R. Fellows, H. S. Anderson, Fabrication and joining of ceramic compact heat exchangers for process integration, International Journal of Applied Ceramic Technology 9 (4) (2012) 700–711.

[74] H. Shulman, N. Ross, Additive manufacturing for cost efficient production of compact ceramic heat exchangers and recuperators, Tech. rep., Ceralink Incorporated, Troy, NY (United States) (2015).

[75] H. Keramati, F. Battaglia, M. A. Arie, F. Singer, M. M. Ohadi, Additive manufacturing of compact manifold-microchannel heat exchangers utilizing direct metal laser sintering, in: 2019 18th IEEE Intersociety Conference on Thermal and Thermomechanical Phenomena in Electronic Systems (ITherm), IEEE, 2019, pp. 423–429.

[76] R. Mathur, 3d printing in architecture, International journal of innovative science, engineering & technology 3 (7) (2016) 583–591.

[77] I. Kaur, P. Singh, State-of-the-art in heat exchanger additive manufacturing, International Journal of Heat and Mass Transfer 178 (2021) 121600.

[78] I. L. Collins, J. A. Weibel, L. Pan, S. V. Garimella, A permeable-membrane microchannel heat sink made by additive manufacturing, International Journal of Heat and Mass Transfer 131 (2019) 1174–1183.

[79] H. Keramati, A. Sadeghi, M. H. Saidi, S. Chakraborty, Analytical solutions for thermo-fluidic transport in electroosmotic flow through rough microtubes, International Journal of Heat and Mass Transfer 92 (2016) 244–251.

[80] M. TOKSOY, Z. H. KARADENIZ, 3d printing of hvac systems.

[81] H. Kobayashi, K. Yaji, S. Yamasaki, K. Fujita, Topology design of two-fluid heat exchange, Structural and Multidisciplinary Optimization 63 (2) (2021) 821–834.

[82] A. Zou, R. Chuan, F. Qian, W. Zhang, Q. Wang, C. Zhao, Topology optimization for a water-cooled heat sink in micro-electronics based on pareto frontier, Applied Thermal Engineering (2022) 118128.

[83] F. Feppon, G. Allaire, C. Dapogny, P. Jolivet, Body-fitted topology optimization of 2d and 3d fluid-to-fluid heat exchangers, Computer Methods in Applied Mechanics and Engineering 376 (2021) 113638.

[84] W. Liu, M. Jin, C. Chen, Q. Chen, Optimization of air supply location, size, and parameters in enclosed environments using a computational fluid dynamics-based adjoint method, Journal of Building Performance Simulation 9 (2) (2016) 149–161.

[85] S. Yan, F. Wang, J. Hong, O. Sigmund, Topology optimization of microchannel heat sinks using a two-layer model, International Journal of Heat and Mass Transfer 143 (2019) 118462.

[86] C. Lin, T. Fan, W. Wang, M. Nießner, Modeling 3d shapes by reinforcement learning, in: European Conference on Computer Vision, Springer, 2020, pp. 545–561.

[87] N. Brown, A. Garland, G. Fadel, G. Li, Deep reinforcement learning for engineering design through topology optimization of elementally discretized design domains, in: AAAI 2022 Workshop on AI for Design and Manufacturing (ADAM), 2021.

[88] E. Hachem, H. Ghraieb, J. Viquerat, A. Larcher, P. Meliga, Deep reinforcement learning for the control of conjugate heat transfer, Journal of Computational Physics 436 (2021) 110317, publisher: Elsevier.

[89] G. Beintema, A. Corbetta, L. Biferale, F. Toschi, Controlling rayleigh–bénard convection via reinforcement learning, Journal of Turbulence 21 (9-10) (2020) 585–605.

[90] J. Rabault, A. Kuhnle, Accelerating deep reinforcement learning strategies of flow control through a multi-environment approach, Physics of Fluids 31 (9) (2019) 094105, publisher: AIP Publishing LLC.

[91] V. Makoviychuk, L. Wawrzyniak, Y. Guo, M. Lu, K. Storey, M. Macklin, D. Hoeller, N. Rudin, A. Allshire, A. Handa, others, (Isaac Gym: High performance GPU-based physics simulation for robot learning), arXiv preprint arXiv:2108.10470.

[92] M. Sheikholeslami, H. Keramati, A. Shafee, Z. Li, O. A. Alawad, I. Tlili, Nanofluid mhd forced convection heat transfer around the elliptic obstacle inside a permeable lid drive 3d enclosure considering lattice boltzmann method, Physica A: Statistical Mechanics and its Applications 523 (2019) 87–104.

[93] K. Maute, E. Ramm, Adaptive topology optimization, Structural optimization 10 (2) (1995) 100–112.

[94] N. Gilmore, V. Timchenko, C. Menictas, Manifold microchannel heat sink topology optimisation, International Journal of Heat and Mass Transfer 170 (2021) 121025.

[95] S. Ozguc, L. Pan, J. A. Weibel, Topology optimization of microchannel heat sinks using a homogenization approach, International Journal of Heat and Mass Transfer 169 (2021) 120896.

[96] S. Hoyer, J. Sohl-Dickstein, S. Greydanus, Neural reparameterization improves structural optimization, arXiv preprint arXiv:1909.04240.

[97] P. M. Zadeh, M. Sayadi, A. Kosari, An efficient metamodel-based multi-objective multidisciplinary design optimization framework, Applied Soft Computing 74 (2019) 760–782.

[98] C. Liu, Z. Wan, Y. Liu, X. Li, D. Liu, Trust-region based adaptive radial basis function algorithm for global optimization of expensive constrained black-box problems, Applied Soft Computing 105 (2021) 107233.

[99] S. Hoyer, J. Sohl-Dickstein, S. Greydanus, Neural reparameterization for optimization of physical designs, uS Patent App. 16/722,587 (Jun. 24 2021).

[100] D. Lee, W. Chen, et al., Deep generative models for geometric design under uncertainty, arXiv preprint arXiv:2112.08919.

[101] J. Zhuang, D. Kochkov, Y. Bar-Sinai, M. P. Brenner, S. Hoyer, Learned discretizations for passive scalar advection in a two-dimensional turbulent flow, Physical Review Fluids 6 (6) (2021) 064605.

[102] K. R. Allen, T. Lopez-Guevara, K. Stachenfeld, A. Sanchez-Gonzalez, P. Battaglia, J. Hamrick, T. Pfaff, Physical design using differentiable learned simulators, arXiv preprint arXiv:2202.00728.

[103] R. Yamashita, M. Nishio, R. K. G. Do, K. Togashi, Convolutional neural networks: an overview and application in radiology, Insights into imaging 9 (4) (2018) 611–629.

[104] W. Chen, A. Ramamurthy, Deep generative model for efficient 3d airfoil parameterization and generation, in: AIAA Scitech 2021 Forum, 2021, p. 1690.

[105] D. R. Rutkowski, A. Roldán-Alzate, K. M. Johnson, Enhancement of cerebrovascular 4d flow mri velocity fields using machine learning and computational fluid dynamics simulation data, Scientific reports 11 (1) (2021) 1–11.

[106] X. Guo, W. Li, F. Iorio, Convolutional neural networks for steady flow approximation, in: Proceedings of the 22nd ACM SIGKDD international conference on knowledge discovery and data mining, 2016, pp. 481–490.

[107] R. Vinuesa, S. L. Brunton, The potential of machine learning to enhance computational fluid dynamics, arXiv preprint arXiv:2110.02085.

[108] S. L. Brunton, Applying machine learning to study fluid mechanics, Acta Mechanica Sinica (2022) 1–9.

[109] A. Mendible, W. Lowrie, S. L. Brunton, J. N. Kutz, Data-driven modeling of two-dimensional detonation wave fronts, Wave Motion (2022) 102879.

[110] D. Kochkov, J. A. Smith, A. Alieva, Q. Wang, M. P. Brenner, S. Hoyer, Machine learning–accelerated computational fluid dynamics, Proceedings of the National Academy of Sciences 118 (21).

[111] T. Pfaff, M. Fortunato, A. Sanchez-Gonzalez, P. W. Battaglia, Learning mesh-based simulation with graph networks, arXiv preprint arXiv:2010.03409.

[112] B. Ummenhofer, L. Prantl, N. Thuerey, V. Koltun, Lagrangian fluid simulation with continuous convolutions, in: International Conference on Learning Representations, 2019.

[113] H. Ma, Y. Zhang, N. Thuerey, X. Hu, O. J. Haidn, Physics-driven learning of the steady navier-stokes equations using deep convolutional neural networks, arXiv preprint arXiv:2106.09301.

[114] A. Abucide-Armas, K. Portal-Porras, U. Fernandez-Gamiz, E. Zulueta, A. Teso-Fz-Betoño, A data augmentation-based technique for deep learning applied to cfd simulations, Mathematics 9 (16) (2021) 1843.

[115] S. Ye, Z. Zhang, X. Song, Y. Wang, Y. Chen, C. Huang, A flow feature detection method for modeling pressure distribution around a cylinder in non-uniform flows by using a convolutional neural network, Scientific reports 10 (1) (2020) 1–10.

[116] C. Birkenmaier, L. Krenkel, Convolutional neural networks for approximation of blood flow in artificial lungs, in: STAB/DGLR Symposium, Springer, 2020, pp. 451–460.

[117] M. Pourbagian, A. Ashrafizadeh, Super-resolution of low-fidelity flow solutions via generative adversarial networks, SIMULATION (2021) 00375497211061260.

[118] J. Sang, X. Pan, T. Lin, W. Liang, G. Liu, A data-driven artificial neural network model for predicting wind load of buildings using gsm-cfd solver, European Journal of Mechanics-B/Fluids 87 (2021) 24–36.

[119] J. Chen, E. Hachem, J. Viquerat, Graph neural networks for laminar flow prediction around random two-dimensional shapes, Physics of Fluids 33 (12) (2021) 123607.

[120] P. W. Battaglia, J. B. Hamrick, V. Bapst, A. Sanchez-Gonzalez, V. Zambaldi, M. Malinowski, A. Tacchetti, D. Raposo, A. Santoro, R. Faulkner, et al., Relational inductive biases, deep learning, and graph networks, arXiv preprint arXiv:1806.01261.

[121] A. Khan, A. Sohail, U. Zahoora, A. S. Qureshi, A survey of the recent architectures of deep convolutional neural networks, Artificial intelligence review 53 (8) (2020) 5455–5516.

[122] X. Han, H. Gao, T. Pffaf, J.-X. Wang, L.-P. Liu, Predicting physics in mesh-reduced space with temporal attention, arXiv preprint arXiv:2201.09113.

[123] I. S. Kavvadias, G. K. Karpouzas, E. M. Papoutsis-Kiachagias, D. I. Papadimitriou, K. C. Giannakoglou, Optimal flow control and topology optimization using the continuous adjoint method in unsteady flows, in: Advances in Evolutionary and Deterministic Methods for Design, Optimization and Control in Engineering and Sciences, Springer, 2015, pp. 159–173.

[124] G. H. Yoon, Topology optimization method with finite elements based on the k-ε turbulence model, Computer Methods in Applied Mechanics and Engineering 361 (2020) 112784.

[125] Q. Zhou, R. Ooka, Neural network for indoor airflow prediction with cfd database, in: Journal of Physics: Conference Series, Vol. 2069, IOP Publishing, 2021, p. 012154.

[126] F. Jaffar, T. Farid, M. Sajid, Y. Ayaz, M. J. Khan, Prediction of drag force on vehicles in a platoon configuration using machine learning, IEEE Access 8 (2020) 201823–201834.

[127] M. Arie, A. Shooshtari, S. Dessiatoun, E. Al-Hajri, M. Ohadi, Numerical modeling and thermal optimization of a single-phase flow manifold-microchannel plate heat exchanger, International Journal of Heat and Mass Transfer 81 (2015) 478–489.

[128] S. N. Lophaven, H. B. Nielsen, J. Søndergaard, et al., DACE: a Matlab kriging toolbox, Vol. 2, Citeseer, 2002.

[129] T. Craeghs, S. Clijsters, E. Yasa, J.-P. Kruth, Online quality control of selective laser melting, in: 2011 International Solid Freeform Fabrication Symposium, University of Texas at Austin, 2011.

[130] H. Keramati, F. Hamdullahpur, M. Barzegari, Deep reinforcement learning for heat exchanger shape optimization, International Journal of Heat and Mass Transfer 194 (2022) 123112.

[131] P. K. Jayaraman, A. Sanghi, J. G. Lambourne, K. D. Willis, T. Davies, H. Shayani, N. Morris, UV-Net: Learning From Boundary Representations, in: Proceedings of

the IEEE/CVF Conference on Computer Vision and Pattern Recognition, 2021, pp. 11703–11712.

[132] W. Chen, Data-Driven Geometric Design Space Exploration and Design Synthesis, PhD Thesis, University of Maryland, College Park (2019).

[133] W. Chen, M. Fuge, J. Chazan, Design Manifolds Capture the Intrinsic Complexity and Dimension of Design Spaces, Journal of Mechanical Design 139. doi:10.1115/1.4036134.

[134] A. Logg, K.-A. Mardal, G. N. Wells, others, (Automated Solution of Differential Equations by the Finite Element Method), Springer, 2012. doi:10.1007/978-3-642-23099-8.

[135] C. Geuzaine, J.-F. Remacle, Gmsh: A 3-d finite element mesh generator with built-in pre-and post-processing facilities, International journal for numerical methods in engineering 79 (11) (2009) 1309–1331.

[136] B. E. Abali, An accurate finite element method for the numerical solution of isothermal and incompressible flow of viscous fluid, Fluids 4 (1) (2019) 5, publisher: Multidisciplinary Digital Publishing Institute.

[137] J. Viquerat, J. Rabault, A. Kuhnle, H. Ghraieb, A. Larcher, E. Hachem, Direct shape optimization through deep reinforcement learning, Journal of Computational Physics 428 (2021) 110080.

[138] T. M. Oyinloye, W. B. Yoon, Application of computational fluid dynamics (cfd) simulation for the effective design of food 3d printing (a review), Processes 9 (11) (2021) 1867.

[139] M. Kuenstle, H. Rashed-Ali, Research methods in computational fluid dynamics, Research Methods in Building Science and Technology (2021) 95–114.

[140] E. Haghighat, M. Raissi, A. Moure, H. Gomez, R. Juanes, A physics-informed deep learning framework for inversion and surrogate modeling in solid mechanics, Computer Methods in Applied Mechanics and Engineering 379 (2021) 113741.

[141] M. Lapan, Deep reinforcement learning hands-on, Packt publishing, 2020.

[142] K. Wang, W. Sun, Meta-modeling game for deriving theory-consistent, microstructure-based traction–separation laws via deep reinforcement learning, Computer Methods in Applied Mechanics and Engineering 346 (2019) 216–241.

[143] J. Schulman, F. Wolski, P. Dhariwal, A. Radford, O. Klimov, Proximal policy optimization algorithms, arXiv preprint arXiv:1707.06347.

[144] J. Schulman, S. Levine, P. Abbeel, M. Jordan, P. Moritz, Trust region policy optimization, in: International conference on machine learning, PMLR, 2015, pp. 1889–1897.

[145] R. Webb, E. Eckert, Application of rough surfaces to heat exchanger design, international journal of heat and mass transfer 15 (9) (1972) 1647–1658.

[146] C. Sammut, G. I. Webb, Encyclopedia of machine learning, Springer Science & Business Media, 2011.

[147] M. Lapan, Deep reinforcement learning hands-on, Packt publishing, 2020.

[148] F. Chollet, Xception: Deep learning with depthwise separable convolutions, in: Proceedings of the IEEE conference on computer vision and pattern recognition, 2017, pp. 1251–1258.

[149] K. He, X. Zhang, S. Ren, J. Sun, Deep residual learning for image recognition, in: Proceedings of the IEEE conference on computer vision and pattern recognition, 2016, pp. 770–778.

[150] C. Szegedy, W. Liu, Y. Jia, P. Sermanet, S. Reed, D. Anguelov, D. Erhan, V. Vanhoucke, A. Rabinovich, Going deeper with convolutions, in: Proceedings of the IEEE conference on computer vision and pattern recognition, 2015, pp. 1–9.

[151] L. Alzubaidi, J. Zhang, A. J. Humaidi, A. Al-Dujaili, Y. Duan, O. Al-Shamma, J. Santamaría, M. A. Fadhel, M. Al-Amidie, L. Farhan, Review of deep learning: Concepts, cnn architectures, challenges, applications, future directions, Journal of big Data 8 (1) (2021) 1–74.

[152] Z. Fan, H. Lin, C. Li, J. Su, S. Bruno, G. Loprencipe, Use of parallel resnet for high-performance pavement crack detection and measurement, Sustainability 14 (3) (2022) 1825.

[153] S. L. Brunton, J. N. Kutz, Data-driven science and engineering: Machine learning, dynamical systems, and control, Cambridge University Press, 2019.

[154] C. Szegedy, V. Vanhoucke, S. Ioffe, J. Shlens, Z. Wojna, Rethinking the inception architecture for computer vision, in: Proceedings of the IEEE conference on computer vision and pattern recognition, 2016, pp. 2818–2826.

[155] L. Li, K. Jamieson, A. Rostamizadeh, E. Gonina, M. Hardt, B. Recht, A. Talwalkar, Massively parallel hyperparameter tuning.

[156] L. Yang, F. Albregtsen, Fast and exact computation of cartesian geometric moments using discrete green's theorem, Pattern Recognition 29 (7) (1996) 1061–1073.

[157] C. M. Okubo Jr, L. F. Sá, C. Y. Kiyono, E. C. Silva, A discrete adjoint approach based on finite differences applied to topology optimization of flow problems, Computer Methods in Applied Mechanics and Engineering 389 (2022) 114406.

[158] W. Chen, F. Ahmed, Padgan: Learning to generate high-quality novel designs, Journal of Mechanical Design 143 (3).

[159] P. Baque, E. Remelli, F. Fleuret, P. Fua, Geodesic convolutional shape optimization, in: International Conference on Machine Learning, PMLR, 2018, pp. 472–481.

[160] M. C. Messner, Convolutional neural network surrogate models for the mechanical properties of periodic structures, Journal of Mechanical Design 142 (2) (2020) 024503.

[161] O. Vinyals, I. Babuschkin, W. M. Czarnecki, M. Mathieu, A. Dudzik, J. Chung, D. H. Choi, R. Powell, T. Ewalds, P. Georgiev, et al., Grandmaster level in starcraft ii using multi-agent reinforcement learning, Nature 575 (7782) (2019) 350–354.

[162] P. Sunehag, G. Lever, A. Gruslys, W. M. Czarnecki, V. Zambaldi, M. Jaderberg, M. Lanctot, N. Sonnerat, J. Z. Leibo, K. Tuyls, et al., Value-decomposition networks for cooperative multi-agent learning, arXiv preprint arXiv:1706.05296.

[163] C. Yu, A. Velu, E. Vinitsky, Y. Wang, A. Bayen, Y. Wu, The surprising effectiveness of ppo in cooperative, multi-agent games, arXiv preprint arXiv:2103.01955.

[164] I. Mordatch, P. Abbeel, Emergence of grounded compositional language in multi-agent populations, arXiv preprint arXiv:1703.04908.

[165] G. Chen, A new framework for multi-agent reinforcement learning–centralized training and exploration with decentralized execution via policy distillation, arXiv preprint arXiv:1910.09152.

[166] R. Lowe, Y. Wu, A. Tamar, J. Harb, P. Abbeel, I. Mordatch, Multi-agent actor-critic for mixed cooperative-competitive environments, Neural Information Processing Systems (NIPS).

[167] G. Wu, T.-Y. Bong, Overall efficiency of a straight fin with combined heat and mass transfer.

[168] W. Chen, F. Ahmed, Mo-padgan: Reparameterizing engineering designs for augmented multi-objective optimization, Applied Soft Computing 113 (2021) 107909.

[169] I. Iu, N. Weber, P. Bansal, D. Fisher, Applying the effectiveness-ntu method to elemental heat exchanger models, ASHRAE Transactions 113 (1) (2007) 504–513.

[170] E. Burman, Consistent supg-method for transient transport problems: Stability and convergence, Computer Methods in Applied Mechanics and Engineering 199 (17-20) (2010) 1114–1123.

APPENDICES

Appendix A

A.1 Weak Form of Convection-diffusion Equation

In this section, we present our numerical approach for solving Eq. 4.3 and Eq. 4.5. In order to sove the PDEs we need to discretize space and time. Here, we present the procedure for convection diffusion equation; the same approach is valid for Navies-stoks equation except for time discretization which we use BDF2 to enhance the stability and convergence during shape variation (please refer to Erik Burman for further information [170]).

To solve equations in finite element method characterized by a variational formulation, weak form of equations discretized in the domain space is required. The weak form of equations is abtained by defining a space of test functions; each term of the PDE are multiplied by any arbitrary function as a member of this space.

We multiply Eq. A.1 to an arbitrary function $v \in \mathcal{V}$, :

$$\frac{\partial T}{\partial t} = \nabla \cdot (k_f \nabla T) - \rho c_p (\boldsymbol{u} \cdot \nabla T) \tag{A.1}$$

$$\mathcal{V} = \left\{ v(\mathbf{x}) | \mathbf{x} \in \Omega, v(\mathbf{x}) \in \mathcal{H}^1(\Omega), \text{ and } v(\mathbf{x}) = 0 \text{ on } \Gamma \right\} \tag{A.2}$$

In which the $\mathcal{H}^1$ denotes the Sobolev space of the domain Ω, which is a space of functions whose derivatives are square-integrable functions in Ω. The solution of the PDE belongs to a trial function space, which is similarly defined as:

$$\mathcal{S}_t = \left\{ T(\mathbf{x}, t) | \mathbf{x} \in \Omega, t > 0, T(\mathbf{x}, t) \in \mathcal{H}^1(\Omega), \text{ and } \frac{\partial T}{\partial n} = 0 \text{ on } \Gamma \right\} \tag{A.3}$$

$$\frac{\partial T}{\partial t} v = \nabla \cdot (k_f \nabla T)\, v - \rho c_p (\boldsymbol{u} \cdot \nabla T) v \tag{A.4}$$

Integrating over the whole domain yields:

$$\int_\Omega \frac{\partial T}{\partial t} v d\omega = \int_\Omega \nabla \cdot (k_f \nabla T) v d\omega - \int_\Omega \rho c_p (\boldsymbol{u} \cdot \nabla T) v d\omega \tag{A.5}$$

The diffusion term can be split using the integration by parts technique

$$\int_\Omega \nabla \cdot (k_f \nabla T) v d\omega = \int_\Omega \nabla \cdot [v(k_f \nabla T)] d\omega - \int_\Omega (\nabla v) \cdot (k_f \nabla T) d\omega \tag{A.6}$$

Where the second term can be converted to a surface integral on the domain boundary by applying the Green's divergence theory:

$$\int_\Omega \nabla \cdot [v(k_f \nabla T)] d\omega = \int_\Gamma k_f v \frac{\partial T}{\partial n} d\gamma = 0 \tag{A.7}$$

Applying BDF1 scheme for temporal discretization:

$$\frac{\partial T}{\partial t} = \frac{T - T^n}{\Delta t} \tag{A.8}$$

Where T^n denotes the value of the temperature in the previous time step.

$$\int_\Omega \frac{T - T^n}{\Delta t} v d\omega = -\int_\Omega k_f \nabla T \cdot \nabla v d\omega - \int_\Omega \rho c_p (\boldsymbol{u} \cdot \nabla T) v d\omega \tag{A.9}$$

Re-ordering the equation A.9, we solve for equation A.10.

$$\int_\Omega T v d\omega + \int_\Omega \Delta t k_f \nabla T \cdot \nabla v d\omega + \int_\Omega \Delta t \rho c_p (\boldsymbol{u} \cdot \nabla T) v d\omega = \int_\Omega T^n v d\omega \tag{A.10}$$

A.2 Hyperparameters for Single-agent PPO

In this section, we provide parameters and hyperparameters of the deep Rl framework to facilitate the Reproducibility.

Table A.1: PPO hyperparameters used for shape optimization framework

Hyperparameter	**Value**
Learning rate	$1 - 2.5 \times 10^{-3}$
Hidden layers	3
Connection	Dense
Clipping ratio ϵ	0.2
Nodes hidden layers	256
Activation function hidden layers	ReLU
Activation function output layer	Linear
Optimizer	Adam
Adam stepsize	1×10^{-3}
Discount factor γ	0.99
GAE parameter (λ)	0.95
Batch size (N)	50

A.3 Hyperparameters for Optimized Regular CNN

In table A.2, we provide hyperparameters of the optimized regular CNN to facilitate the reproducibility.

Table A.2: Hyperparameter Values for Optimized Regular CNN

Hyperparameter	**Value**
Learning rate	1×10^{-3}
Decay	5×10^{-3}
Number of Convolution layers	11
Number of MaxPooling layers	5
Number of FC layers	2
Activation function hidden layers	ReLU
Activation function output layer	Linear
Optimizer	Adam
Batch size (N)	128

A.4 Optimized CNN Architecture

In this section, we show the architecture of the optimized CNN used for the case with a single shape. The input image size is downscaled version of the original image by a factor of two with the size of 253 × 253 pixels. Activation functions for convolutional layers and the fully connected layer are ReLU and the output neuron is using linear function.

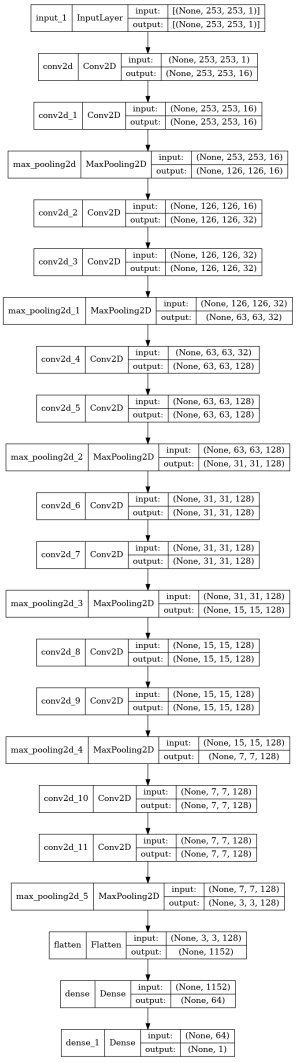

Figure A.1: Optimized CNN architecture

A.5 Hyperparameters for Xception Network used for Single Shape

In table A.3, some of the hyperparameters of the Xception model used for single fin shape are provided. Other hyperparameters are used the same as those in the original article [148].

Table A.3: Hyperparameters used for Xception network used for single shape

Hyperparameter	**Value**
Learning rate	1×10^{-3}
Optimizer	SGD
Batch size (N)	256

A.6 Hyperparameters for Xception Network used for MARL

In table A.4, some of the hyperparameters of the Xception model used for multiple fin shapes are provided. No specific changes were made to the original architecture [148].

Table A.4: Hyperparameters used for Xception network in MARL

Hyperparameter	**Value**
Learning rate	0.0001
Optimizer	Adam ($\beta_1 = 0.5, \beta_2 = .997$)
Batch size (N)	256

A.7 Hyperparameters for Multi-agent simple reference MPE

In this section, some of the hyperparameters of multi-agent RL used for simple reference particle-world environment (MPE) are provided.

Table A.5: Hyperparameters for MAPPO used for simple reference MPE

Hyperparameter	**Value**
Learning rate	7×10^{-4}
Hidden layers	3
Connection	Recurrent
Number of agents	2
Number of landmarks	3
Epoch	15
Likelihood ratio clipping ϵ	0.2
Activation function hidden layers	ReLU
Discount factor γ	0.99
GAE parameter (λ)	0.95

A.8 Hyperparameters for Multi-agent simple spread MPE

Here, some of the hyperparameters of simple spread MPE are provided.

Table A.6: Hyperparameters for simple spread MPE

Hyperparameter	**Value**
Learning rate	5×10^{-4}
Hidden layers	3
Connection	Recurrent
Number of agents	5
Number of landmarks	5
Epoch	10
Likelihood ratio clipping ϵ	0.2
Activation function hidden layers	ReLU
Discount factor γ	0.99
GAE parameter (λ)	0.95

A.9 Hyperparameters for Multi-agent Generative Design

In this section, some of the parameters and hyperparameters of the multi-agent GD framework are provided.

Table A.7: Hyperparameters for MAPPO used for optimization of multiple shapes

Hyperparameter	**Value**
Learning rate	$5 - 9 \times 10^{-4}$
Hidden layers	3
Connection	Dense
Number of agents	5
Likelihood ratio clipping ϵ	0.2
Nodes hidden layers	512
Activation function hidden layers	ReLU
Baseline optimizer	Adam
Optimizer learning rate	1×10^{-3}
Discount factor γ	0.99
Subsampling fraction	0.2
Batch size (N)	40